UNCLASSIFIED
Security Classification

AD 743560

DOCUMENT CONTROL DATA - R & D

(Security classification of title, body of abstract and indexing annotation must be entered when the overall report is classified)

1. ORIGINATING ACTIVITY (Corporate author)

Air Force Institute of Technology (AFIT-EN)
Wright-Patterson Air Force Base, Ohio, 45433

2a. REPORT SECURITY CLASSIFICATION
Unclassified

2b. GROUP

3. REPORT TITLE

ATMOSPHERIC CONTRAST TRANSMISSION: APPLICATION TO THE VISUAL DETECTION AND ELECTRO-OPTICAL LOCK-ON PROBLEM

4. DESCRIPTIVE NOTES (Type of report and inclusive dates)
AFIT Thesis

5. AUTHOR(S) (First name, middle initial, last name)

Edward A. Duff
Capt., USAF

6. REPORT DATE	7a. TOTAL NO. OF PAGES	7b. NO. OF REFS
June 1972	175	28

8a. CONTRACT OR GRANT NO.	9a. ORIGINATOR'S REPORT NUMBER(S)
b. PROJECT NO.	GEP/PH/72-4
c.	9b. OTHER REPORT NO(S) (Any other numbers that may be assigned this report)
d.	

10. DISTRIBUTION STATEMENT

Approved for public release; distribution unlimited.

11. SUPPLEMENTARY NOTES	12. SPONSORING MILITARY ACTIVITY
	Operations Evaluation Group AF/SAV Asst Chief of Staff, Studies and Analysis Hq USAF, Washington, D. C.

13. ABSTRACT

The contrast and size of the target limit detection or lock-on range. Models for the prediction of detection range are evaluated in this report. The contrast available at the eye or the electro-optical sensor is assumed to be the limiting factor. The atmosphere provides a transmission factor for the target-background contrast. A model for the prediction of contrast transmission proposed by Duntley in 1948 is examined. Duntley's work provides an analytic solution based on an equation which relates visibility to air-transmittance along an inclined path, and a table of sky-ground ratios. An improved relation for visibility is developed by the author. More realistic sky-ground ratios are obtained from calculated data and from flight tests.

The RRA Monte Carlo model and the AWS model, which predict contrast transmission, are compared for accuracy. The AWS model is also compared to recent flight data. The AWS model is shown to predict generally higher results than the RRA data, due to the approximations used. The AWS model does provide a useful, fast tool for prediction of contrast transmission.

A more recent concept developed by Duntley, the directional path reflectance R*, is used to describe the atmospheric effects. R* provides a useful single parameter for evaluating a situation to determine approach angles where the effect of haze is a minimum. The directional background reflectance $_bR_0$ must be used with R* to predict contrast transmission. Graphs illustrating the application are presented.

DD FORM 1 NOV 65 1473

UNCLASSIFIED
Security Classification

14. KEY WORDS	LINK A		LINK B		LINK C	
	ROLE	WT	ROLE	WT	ROLE	WT
Atmospheric contrast transmission						
Atmospheric haze models						
Transfer function for the atmosphere						
Sky-ground ratio						
Visibility						
Comparison of atmospheric haze models						
Directional path reflectance						
Directional background reflectance						
Visual detection range						
Electro-optical lock-on range						

ATMOSPHERIC CONTRAST TRANSMISSION: APPLICATION TO THE VISUAL DETECTION AND ELECTRO-OPTICAL LOCK-ON PROBLEM

THESIS

GEP/PH/72-4

Edward A. Duff
Captain USAF

ATMOSPHERIC CONTRAST TRANSMISSION: APPLICATION TO THE VISUAL DETECTION AND ELECTRO-OPTICAL LOCK-ON PROBLEM

THESIS

Presented to the Faculty of the School of Engineering

of the Air Force Institute of Technology

Air University

in Partial Fulfillment of the

Requirements for the Degree of

Master of Science

by

Edward A. Duff, B.S.
Captain USAF

Graduate Physics Engineering

June 1972

Preface

The research which went into this report was done at the request of the Operations Evaluation Group, Assistant Chief of Staff, Studies and Analysis, USAF. The detection of tactical military targets is approached from the aspects of contrast and contrast transmission by the atmosphere. An applied approach is taken in which the factors affecting contrast transmission are pointed out, methods of solving the problem are presented and the most promising approach chosen. The attempt has been made to utilize existing models and concepts and apply them to this problem. Experimental techniques have also been investigated which may be helpful in correlating the results of model predictions and flight test data. It has become obvious to the author that the relation of model predictions to flight test data is still very inexact due to the inaccuracy of visibility measurements and the many approximations which must be made to reasonably handle the radiative transfer problem. This indicates a continued and increased need for simple, reliable measurement techniques during flight tests to describe the physical quantities which affect the operational problem. Only through these efforts can predictive models be improved.

I would like to thank many people whose efforts made this research and its results possible. In particular, Colonel Ed Battle who sponsored the research allowed me freedom to pursue different approaches, which has been invaluable in completing the work. I thank also Mr. Tom Furness and Mr. Lee Task of the AF Aero-Medical Research Laboratories for their help on very short notice during the measurement phase of the research program. Captain Jim Mardis of AFIT and Mr. Ken Arnold of ASD Technical Photographic

Branch also were very helpful during the field measurements. Mr. Lenny Crouch and Capt. Neil McQuage of the Air Force Avionics Lab provided much information about the Air Weather Service Haze Model. We also had many interesting and informative discussions on approaches to the problem, for which I am grateful. I thank also Dr. Robert Fenn of the Air Force Cambridge Research Laboratories for the interesting discussions, guidance and valuable information he provided. Dr. Donn Shankland, my advisor at AFIT, has provided some valuable insights and ideas which have enabled me to clarify the problem. My wife Andrea has provided much assistance in preparing drafts of the report and more important, kindness and understanding during the many hours of work.

Edward A. Duff
Captain, USAF

Contents

Contents

List of Figures

List of Figures

List of Figures

List of Figures

List of Figures

List of Tables

List of Tables

List of Symbols

Albedo	defined by the ratio H(Z,u)/H(Z,d), at altitude Z
B(r)	luminance; the photometric equivalent of radiance
$C_0(Z_t,\theta,\phi)$	inherent universal contrast determined for a path of sight of zero length at altitude of the object Z_t in the direction of zenith angle θ and azimuth ϕ
$C_r(Z,\theta,\phi)$	apparent universal contrast as determined at altitude Z from the end of path of sight of length r in the direction of the zenith angle θ and azimuth ϕ
H(Z,d)	irradiance produced by downwelling flux as determined on a horizontal flat plate at altitude Z. This property may be defined by the equation $H(Z,d) \equiv \int_{2\pi} N(Z,\theta',\phi') \cos\theta' d\Omega'$
H(Z,u)	irradiance produced by upwelling flux as determined on a horizontal flat plate at altitude Z
h,h_i	altitude
H_p	scale height for aerosol particles, the height at which aerosol particle density has decreased to 1/e of the value at the surface
H_R	scale height for Rayleigh particles
$\hbar\omega$	energy of a photon of wavelength λ
K	sky-ground ratio
n(r),n(Z)	particle-number density distribution function
N	particle-number density
$N(Z,\theta,\phi)$	radiance as determined from altitude Z in the direction specified by zenith angle θ and azimuth ϕ
${}_bN_0(Z_t,\theta,\phi)$	inherent background radiance as determined at altitude of the receiver Z_t at zenith angle θ and azimuth ϕ
${}_bN_r(Z,\theta,\phi)$	apparent background radiance as determined at altitude Z from the end of a path of sight of length r at zenith angle θ and azimuth ϕ
${}_tN_0(Z_t,\theta,\phi)$	inherent radiance of an object as determined at altitude of the object Z_t at zenith angle θ and azimuth ϕ

List of Symbols

$_{t}N_{r}(Z,\theta,\phi)$	apparent radiance of an object as determined at altitude Z from the end of a path of sight of length r at zenith angle θ and azimuth ϕ
$N_{q}(Z,\theta,\phi)$	equilibrium radiance at altitude Z with the direction of the path of sight specified by zenith angle θ and azimuth ϕ
$N_{*}(Z,\theta,\phi)$	path function at altitude Z with the direction of the path of sight specified by zenith angle θ and azimuth ϕ. This property is a point function of position and direction.
$N^{*}(Z,\theta,\phi)$	path radiance as determined at altitude Z at the end of a path of sight in the direction specified by zenith angle θ and azimuth ϕ
$p(Z,\theta,\phi,\theta',\phi')$	angular scattering phase function which describes the distribution of scattered particles
Q	source function
Q'	emission radiance
$_{b}R_{0}(Z_{t},\theta,\phi)$	inherent background reflectance as determined at altitude of an object Z_{t} and viewed at zenith angle θ and azimuth ϕ
$R^{*}(Z,\theta,\phi)$	directional path reflectance as determined at altitude Z at the end of a path of sight in the direction specified by zenith angle θ and azimuth ϕ
$S(\lambda)$	relative spectral response of a system of interest
t	time
$T(Z,\theta)$	transmission of the atmosphere along a path of sight to altitude with receiver angle θ
$T(\bar{r})$	atmospheric transmittance along a path of sight of length r
v	speed of particle
V	visual range
V,V_{η}	meteorological or visual range
Z,Z_{t}	altitude, altitude of object of interest
$\alpha(r),\alpha(Z)$	absorption coefficient
$\beta(r),\beta(Z)$	scattering coefficient

List of Symbols

β	scattering angle
θ	receiver zenith angle
θ_0	solar zenith angle
$\kappa(r),\kappa(Z)$	attenuation coefficient
λ	wavelength
$\rho(\lambda)$	spectral diffuse reflectance
$\sigma_T(Z,\lambda)$	total attenuation cross section
$\sigma_R(Z,\lambda)$	scattering cross section due to Rayleigh particles
$\sigma_H(Z,\lambda)$	scattering cross section due to haze particles
τ_c	contrast transmission
$\tau_{ext}(Z)$	optical depth
ϕ	azimuth angle
ψ	angular density
Ω	solid angle

Abstract

The contrast and the size of the target limit detection or lock-on range. Models for the prediction of detection ranges are evaluated in this report. The contrast available at the eye or the electro-optical sensor is assumed to be the limiting factor. The atmosphere provides a transmission factor for the target-background contrast. A model for the prediction of contrast transmission proposed by Duntley in 1948 is examined. Duntley's work provides an analytic solution based on an equation which relates visibility to air-transmittance along an inclined path, and a table of sky-ground ratios. An improved equation for relating air-transmittance to visibility is developed by the author. More realistic values of sky-ground ratio were obtained from calculated data and from flight tests.

The RRA Monte Carlo model and the AWS Haze Model, which solve the radiative transfer problem and predict contrast transmission, are compared for accuracy. The AWS model is also compared to recent flight data which predicts contrast transmission. The AWS model is shown to predict generally higher results than the Monte Carlo data, due to the allowance for only two scattering events in the AWS approximations. The AWS model does provide a very fast and useful tool for the prediction of atmospheric effects on contrast transmission.

A more recent concept developed by Duntley, the directional path reflectance R*, is used to describe the atmospheric effects. R* is a calculated parameter based on the path radiance, downward irradiance, and air-transmittance. It may be generated from flight measurements or from model calculations. R* provides a useful single parameter for

evaluating an operational situation to determine approach angles where the effects of haze will be least on contrast transmission. The directional background reflectance ${}_bR_0$ is shown to be an important parameter in the prediction of contrast transmission. ${}_bR_0$ must be used with the R* data to predict the contrast transmission. Sources of measured ${}_bR_0$ data are referenced. Graphs illustrating the use of the R* and ${}_bR_0$ for prediction are presented.

The inherent target contrast is needed with the contrast transmission factor to predict detection or lock-on range. Measurements of inherent target contrast by photometric and photographic means are compared. A simple measurement technique for field use is recommended. Radiometric measurements are presented to illustrate some spectral effects which should be considered in comparisons between the eye and different electro-optical sensors.

ATMOSPHERIC CONTRAST TRANSMISSION: APPLICATION TO THE VISUAL DETECTION AND ELECTRO-OPTICAL LOCK-ON PROBLEM

I. Introduction

Background

All visual systems detect a target by an interaction of two phenomena: the size of the target and the contrast between the target and the background. Both of these phenomena have been studied in detail, particularly during and after World War II. The size dependence is one of resolution and thus a function of whether the eye sees the target with the fovea, or high resolution area, or with the peripheral areas with lower resolving power. The angular subtense required in each of the areas of the eye has been described analytically as a result of experiment. The contrast threshold of the eye is dependent on total illumination present, the minimum detectable contrast decreasing as the total illumination increases until a minimum threshold is reached. Both of the phenomena are also variable between individuals.

Electro-optical systems operate on similar principles and have the same dependencies. The target must be large enough to resolve and it must present sufficient contrast with the background to allow lock-on and tracking. To be specific, an observer in an aircraft detects a target on a television display. He points the electro-optical sensor to center the target in the display and places a tracking gate over the target. The electronics of the system are used to measure the received signal difference from the "target" and "background". If the contrast (electronically, the signal to noise ratio or the difference in signals divided by

the background signal, where the target is assumed to contribute only a small portion of the signal) is sufficient, the electronics will lock-on to the target and will track as the aircraft moves. The target size and angular subtense is a geometry and system resolution problem. It is very important to the detection, or lock-on problem, but not the subject of this report. In this regard, we consider the target to be large enough to resolve and we consider the contrast as the limiting factor.

The problem to be solved is the determination of the contrast available at some point in the atmosphere from readily available meteorological data such as surface visibility and cloud ceiling.

The contrast problem may be divided into three parts. First, we must consider the contrast which exists between the target and the background, in the immediate vicinity of the target, the inherent contrast. Second, we must consider how the contrast is affected by the atmosphere it passes through in getting to the sensor, the contrast transmission or atmospheric transfer function. Third, we must consider the required contrast at the sensor for detection, or lock-on or tracking, the apparent contrast threshold. The inherent contrast may be calculated from the reflectivities of the target and the background, although these are not constant with wavelength, illumination angle, and viewing angle. The apparent contrast threshold can be measured as a function of illumination level and specified for the system. The effects of the atmosphere are the most difficult to solve.

Work was done by Koschneider in 1924 to predict the attenuation of contrast along horizontal paths of sight (Ref 1:33). Duntley extended this work to downward and upward-looking paths of sight in 1948 (Ref 2:179). Under the assumptions which Duntley made, a closed-form solution was obtained

for the contrast transmission of the atmosphere. System designers and systems analysts have subsequently used this solution by Duntley to predict the effects of the atmosphere on contrast transmission. The Air Staff, in an attempt to predict the performance of electro-optical (EO) and visual systems, has used the model, originally stated by Duntley and reiterated by Middleton (Ref 3:64) and by Bailey and Mundie (Ref 4). In attempting to correlate the results of model predictions with lock-on ranges obtained in flight tests of one EO guided system they found large discrepancies between some of the results. It was unknown whether the poor correlation was due to scarce data about the test conditions or whether the model was invalid. In an attempt to answer these questions it was decided to look in more detail at the Duntley model and also the more recent models which relate the effects of the atmosphere on contrast transmission to weather information.

Purpose of the Report

The purpose of this report is to investigate contrast and contrast transmission by the atmosphere and to determine ways to handle the prediction of lock-on ranges. To do this it was necessary to investigate the Duntley model to determine the assumptions on which it is based and how to determine the parameters which are required to use the model. Also one had to investigate the other models which address the problem to see how they agree among themselves, and with flight data which reports contrast transmission. We then can recommend the best model to use, how to use it, and the limitations under which the model must be used.

Scope of Report

The report compares several models for the prediction of contrast

transmission by the atmosphere. It does not attempt to re-solve the radiative transfer problem, but only examines work which has been done, and applies it to the problem at hand. The report presents some measured data on intrinsic contrast and suggests how this may be obtained simply in future flight tests. It does not examine the details of any of the sensor systems involved or their requirements for apparent contrast for detection, lock-on or tracking. In general, it limits itself to the photopic (i.e. visual) region of the spectrum since the electro-optical system is usually controlled by a man who must see the target first. Several important consequences of the different spectral responses of the eye and TV system are pointed out.

Assumptions

With any model, assumptions must be made. These will be pointed out in the discussion of each of the individual models. Along with these assumptions, the apparent contrast threshold is assumed to be a constant for any system to be considered, although none of the data here requires that assumption. Only in the step where lock-on range is finally specified for a given combination of target, illumination, and atmospheric condition, must apparent contrast threshold be specified. Also it is assumed that contrast is the limiting phenomenon and not target size or system resolution. Again this does not limit the validity of the arguments presented; one must simply ask, when determining the range, where adequate contrast is available if the target is large enough to be resolved.

Development of the Report

In Chapter II, the basic equations of contrast and contrast transmission are presented and important concepts are discussed. Different

approaches to the solution are laid out along with some of their assumptions. Duntley's model is examined in detail. In Chapter III, an approach for the description of contrast transmission is chosen and discussed in more detail, and the importance of the directional background reflectance is discussed. Chapter IV compares two model predictions of contrast transmission, and compares one to measured flight data. Chapter V presents graphs which can be used to predict contrast transmission under a variety of cases. Some experimental measurements of intrinsic contrast are presented in Chapter VI along with important consequences of the spectral nature of contrast and contrast transmission. Chapter VII presents the Conclusions and Recommendations.

II. The Problem of Contrast Transmission and Approaches to its Solution

Radiative Transfer Equation

An understanding of the physics of the situation is helpful in understanding the effects of the atmosphere on light. From the conservation of particles in phase space, one may write the radiative transfer equation (Ref 6:27). The equation describes the gain and loss of particles from a beam in direction $\hat{\Omega}$ in a small volume of phase space resulting from scattering, absorption, and reemission.

The equation may be written

$$\frac{\partial \psi}{\partial t} = - v\hat{\Omega}\cdot\nabla\psi(\bar{r},\hat{\Omega},t) - v\kappa(\bar{r},t)\psi(\bar{r},\hat{\Omega},t) + \frac{v\beta(\bar{r},t)}{4\pi}\int_{\Omega'} p(\bar{r},\hat{\Omega},\hat{\Omega}')\psi(\bar{r},\hat{\Omega}',t)\,d\Omega' + Q(\bar{r},\hat{\Omega},v,t) \qquad (1)$$

where

$\psi(\bar{r},\hat{\Omega},t)$ is the angular particle density, i.e., the number of particles, per unit volume, per unit solid angle, at some position $\bar{r}$, with direction $\hat{\Omega}$, speed v, at time t,

$Q(\bar{r},\hat{\Omega},v,t)$ is the source term describing the number of particles per unit volume, per unit solid angle, per unit time, created in the direction $\hat{\Omega}$, with speed v.

$\frac{p(\bar{r},\hat{\Omega},\hat{\Omega}')}{4\pi}$ is the angular scattering phase function which describes the angular distribution of scattered particles at point $\bar{r}$. The function is normalized such that

$$\int_{\Omega'} \frac{p(\bar{r},\hat{\Omega},\hat{\Omega}')}{4\pi}\,d\hat{\Omega}' = \int_{\Omega} \frac{p(\bar{r},\hat{\Omega}',\hat{\Omega})}{4\pi}\,d\Omega = 1 \qquad (2)$$

$\beta(\bar{r},t)$ is the magnitude of the scattering coefficient (units, per unit path length) at position $\bar{r}$ and time t for particles with speed v,

$\kappa(\bar{r},t)$ is the magnitude of the attenuation coefficient (units, per unit path length) at point $\bar{r}$ and time t for particles with speed v.

The first term on the right of the above equation then describes the net number of particles which leave the volume at $\bar{r}$, per unit time, per unit solid angle in direction $\hat{\Omega}$, with speed v and time t which also entered in the same direction $\hat{\Omega}$.

The second term represents the particles per unit volume, per unit time, lost from the beam in all other directions, by scattering or absorption.

The third term represents the number of particles per unit volume, per unit time, scattered into the beam from all other directions Ω' at time t and position $\bar{r}$ with speed v.

The fourth term represents the total number of particles per unit volume, per unit time created in the direction $\hat{\Omega}$, with speed v, at time t and position $\bar{r}$.

If each of the particles is a photon, the $v = c$, the speed of light, and if we define

$$ch\omega\psi(\bar{r},\hat{\Omega},t) = N(\bar{r},\hat{\Omega},t) \tag{3}$$

as the spectral radiance, i.e. the energy per unit area, per unit time, per unit solid angle per unit energy interval at time t in direction $\hat{\Omega}$, at position $\bar{r}$ then we may rewrite Eq (1) as

$$\frac{\partial N}{\partial t} = - c\hat{\Omega}\cdot\nabla N - c\kappa(\bar{r},t)N(\bar{r},\hat{\Omega},t) + \frac{c\beta(\bar{r},t)}{4\pi}\int_{\Omega'} p(\bar{r},\hat{\Omega}',\hat{\Omega})N(\bar{r},\hat{\Omega}',t)d\Omega' + Q'(\bar{r},\hat{\Omega},\hbar\omega,t) \quad (4)$$

In atmospheric problems, the time rate of change of the spectral radiance is very slow compared to the diffusion time of photons through the atmosphere. Thus

$$\frac{\partial N(\bar{r},\hat{\Omega},t)}{\partial t} = 0$$

Assuming now that the atmosphere is uniform in the x,y plane and that variations occur only in the z direction, we can restrict ourselves to the case where the transfer of radiation is independent of position in the x,y plane. Then

$$\hat{\Omega}\cdot\left(\frac{\partial N}{\partial x}\hat{i} + \frac{\partial N}{\partial y}\hat{j} + \frac{\partial N}{\partial z}\hat{k}\right) = \frac{\partial N}{\partial z}|\cos\theta| \quad (5)$$

where θ is the angle between the path of sight and the vertical. Then the transfer equation becomes

$$\frac{\partial N}{\partial z}|\cos\theta| = - \kappa(Z)N(Z,\hat{\Omega}) + \frac{\beta(Z)}{4\pi}\int_{\Omega'} p(Z,\hat{\Omega},\hat{\Omega}')N(Z,\hat{\Omega}')d\Omega' + Q'(Z,\hat{\Omega},\hbar\omega) \quad (6)$$

The physical meaning of the above assumptions is that we neglect effects of scattered clouds which would make the atmosphere non-uniform in the x,y plane. Also we neglect any other haze or fog effects which may be isolated in the atmosphere. We also make a flat earth assumption.

We now note that in the first term on the right hand side of Eq (6), the spectral radiance $N(Z,\hat{\Omega})$ is made up of two portions. It contains the spectral radiance which left some reference surface and has not been

attenuated to the point r in the direction $\hat{\Omega}$, and also the spectral radiance which has been scattered or emitted into the solid angle in the direction $\hat{\Omega}$, and has not yet been attenuated. We call the spectral radiance at the reference surface $N_0(0,\Omega)$ the inherent spectral radiance. The other portion of the spectral radiance we shall call the path radiance $N^*(Z,\hat{\Omega})$ from the surface 0 to the point r.

We now consider our reference surface to be the surface of the earth, with a coordinate system centered at the location of our target of interest. Then we will be concerned with the spectral radiance $N_0(Z_+,\theta,\phi)$ which leaves the target and background in a small solid angle in the direction $\hat{\Omega}$. We will be concerned with the amount which reaches the position r, $N_r(Z,\theta,\phi)$ in that direction.

Contrast and Contrast Transmission

Spectral contrast as defined here is the ratio of the difference in spectral radiance between the target and background to the spectral radiance of the background. In this form it is also called universal contrast. Other forms of spectral contrast are also defined: contrast modulation, which is the ratio of the difference in spectral radiances of target and background to the sum of the spectral radiances; and spectral contrast ratio, the ratio of target spectral radiance to background spectral radiance. Only the universal contrast is dealt with here, although Appendix A shows relations between the different definitions of contrast. Spectral contrast transmission is the ratio of the spectral contrast at any point along a path of sight, the apparent contrast, to the spectral contrast at the source, the inherent contrast.

Non-spectral versions of the above quantities are also defined in which the wavelength dependence has been integrated out. The derivations

which follow are rigorously true only for monochromatic light. The areas where an assumption is made to apply the results to regions of the spectrum will be pointed out.

The inherent contrast depends on the source and position of illumination and viewing as does the contrast transmission. The contrast transmission also depends on the general terrain albedo over which the target is viewed. Albedo is defined here as the ratio of the spectral reflected irradiance to spectral incident irradiance. In addition contrast transmission is a function of the aerosol content of the atmosphere. Any other absorbing or scattering substances in the atmosphere will affect it. The problem may be laid out mathematically as follows: At any point along a path of sight the spectral radiance from a target is made up of the image forming light reflected from the target and transmitted to that point, $N_0(Z_t,\theta,\phi)T(\bar{r})$, and the path radiance $N^*(Z,\theta,\phi)$, the spectral radiance scattered into the path by aerosol and molecular components, and which may be called non-image forming light. Thus,

$$N_r(Z,\theta,\phi) = N_0(Z_t,\theta,\phi)T(\bar{r}) + N^*(Z,\theta,\phi) \qquad (7)$$

where $N_r(Z,\theta,\phi)$ is the spectral radiance at altitude Z, receiver zenith angle θ, and azimuth from the sun ϕ. $N_0(Z_t,\theta,\phi)$ is the spectral radiance at the source $\bar{r} = 0$ into a small solid angle about θ,ϕ and $T(\bar{r})$ is the spectral air-transmittance to altitude Z along a slant path r of receiver zenith angle θ. The geometry is illustrated in Fig. 1.

The equation holds for radiation from the target or the background. The quantities involved are spectral in nature so that a dependence on wavelength is implied. Denoting the spectral radiance from the target by ${}_tN$ and from the background by ${}_bN$ we can compute the spectral contrast at the sensor $C_r(Z,\theta,\phi)$:

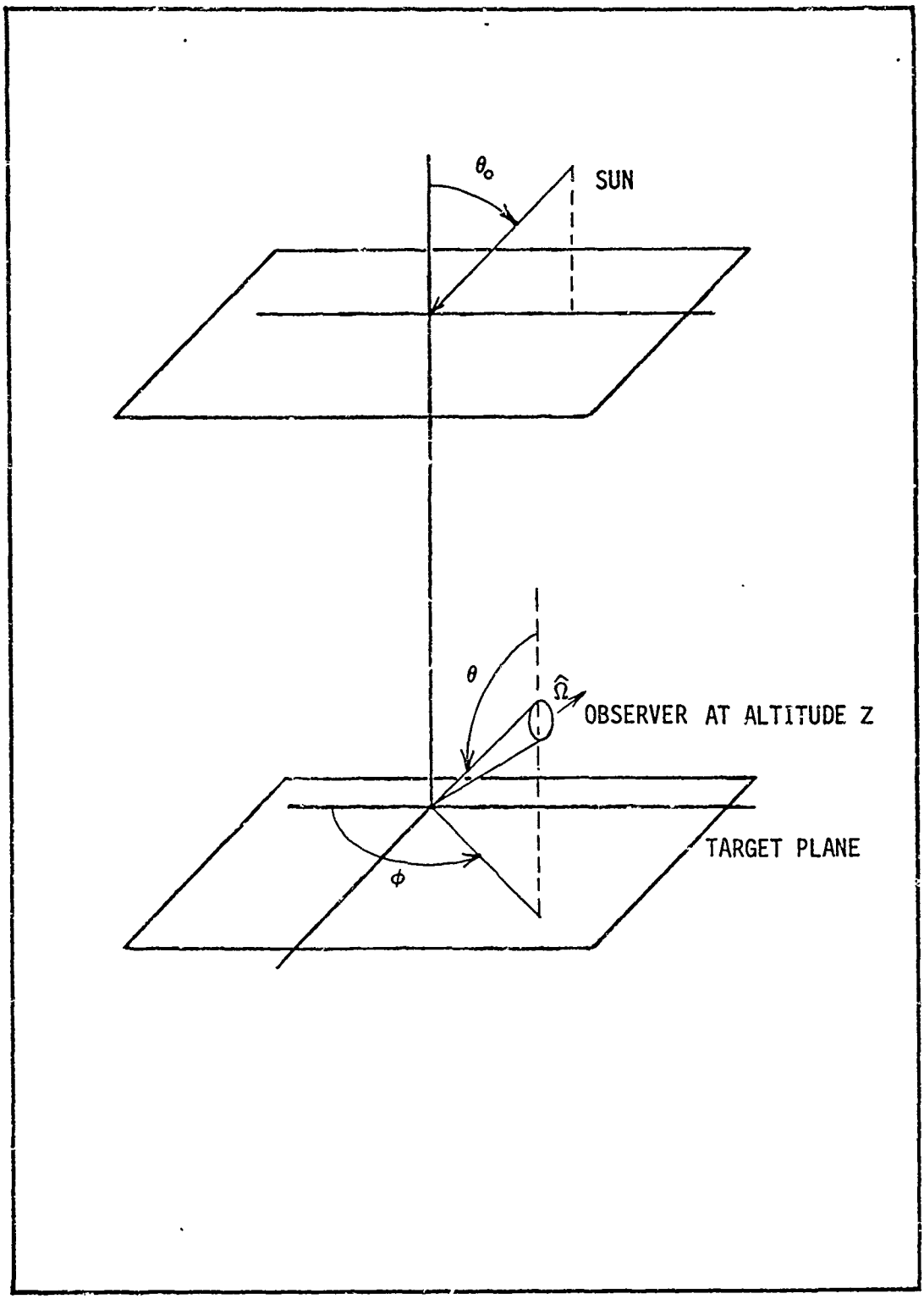

Fig. 1. Schematic Showing the Relationship of the Solar Zenith Angle θ_o, Receiver Zenith Angle θ, and the Receiver Azimuth Angle ϕ.

$$C_r(Z,\theta,\phi) = \frac{{}_tN_r(Z,\theta,\phi) - {}_bN_r(Z,\theta,\phi)}{{}_bN_r(Z,\theta,\phi)} \tag{8}$$

The spectral contrast at the source C_0 is

$$C_0(Z_t,\theta,\phi) = \frac{{}_tN_0(Z_t,\theta,\phi) - {}_bN_0(Z_t,\theta,\phi)}{{}_bN_0(Z_t,\theta,\phi)} \tag{9}$$

The spectral contrast transmission τ_C is the ratio of the apparent spectral contrast to the inherent spectral contrast. It is given by

$$\tau_C(Z,\theta,\phi) = \frac{C_r(Z,\theta,\phi)}{C_0(Z_t,\theta,\phi)} \tag{10}$$

Using Eqs (8) and (9) and dropping the (Z,θ,ϕ) for brevity,

$$\tau_C = \frac{{}_tN_r - {}_bN_r}{{}_bN_r} \cdot \frac{{}_bN_0}{{}_tN_0 - {}_bN_0}$$

Substituting from Eq (7) for the elements of the first term,

$$\tau_C = \frac{{}_tN_0T - {}_bN_0T}{{}_bN_0T + N^*} \cdot \frac{{}_bN_0}{{}_tN_0 - {}_bN_0}$$

Dividing

$$\tau_C = \frac{{}_bN_0T}{{}_bN_0T + N^*} \tag{11}$$

then dividing by the numerator, we get

$$\tau_C = \frac{1}{1 + \frac{N^*}{{}_bN_0T}} \tag{12}$$

This is the basic equation for computing spectral contrast transmission through the atmosphere. Rewriting to show the full dependence,

$$\tau_c(Z,\theta,\phi) = \frac{1}{1 + \frac{N^*(Z,\theta,\phi)}{b^{N_0}(Z_+,\theta,\phi)T(Z,\theta)}} \tag{13}$$

Here we notice that the spectral contrast transmission is a function of altitude, receiver zenith angle, and azimuth of the path of sight with respect to the sun, and we see the complex way in which this comes about. The transmission dependence is easily understood: as the range increases, the transmission decreases due to scattering and absorption. The range along a slant path is described by

$$R = Z\,|\sec\theta| \tag{14}$$

where θ is the receiver zenith angle (see Fig. 1). This statement makes the flat earth assumption and must be corrected for long slant paths (Ref 5:35). The spectral attenuation coefficient $\kappa(Z)$ describes the distance in which a beam of unit irradiance is reduced to 1/e of its initial value by scattering or absorption or both. The attenuation coefficient $\kappa(Z) = \alpha(Z) + \beta(Z)$ where $\alpha(Z)$ is the absorption coefficient and $\beta(Z)$ is the scattering coefficient. For a horizontal path $\kappa(Z) = \kappa_0$ and the spectral transmission is just

$$T(R) = \exp(-\kappa_0 R) \tag{15}$$

Since the attentuation coefficient is not constant with altitude, the concept of optical depth was evolved. This is defined by

$$\tau_{ext}(Z) = \int_0^Z \kappa(Z)\,dZ \tag{16}$$

The spectral air-transmittance for any slant path through the atmosphere is then given by

$$T(\bar{r}) = T(Z,\theta) = \exp(-\tau_{ext}|\sec\theta|) \tag{17}$$

The spectral radiance from the background is seen to be a function of target height, and the angle of the path of sight relative to the sun or other source of illumination. This target height dependence enters since the amount of spectral irradiance reaching the target from the sun or the sky is a function of altitude. The θ,ϕ dependence is due to the directional reflectance properties of all real materials. It is only for the ideal, Lambertian, or diffuse surface, that the spectral radiance would be constant in all directions, independent of the relation of the source of illumination and the viewing angle.

The dependence on altitude of the path radiance N* enters through the dependence of the number and type of scatterers, absorbers or emitters on altitude. No single function can describe this dependence although it is usually assumed that there is an exponential decrease in scatterers with altitude up to some altitude. The dependence of N* on θ and ϕ is due to the angular distribution of scattering $p(Z,\hat{\Omega},\hat{\Omega}')$ with respect to the source of illumination. Figure 2 shows a Rayleigh scattering function and a representative aerosol scattering function (Ref 6:21). The dependence

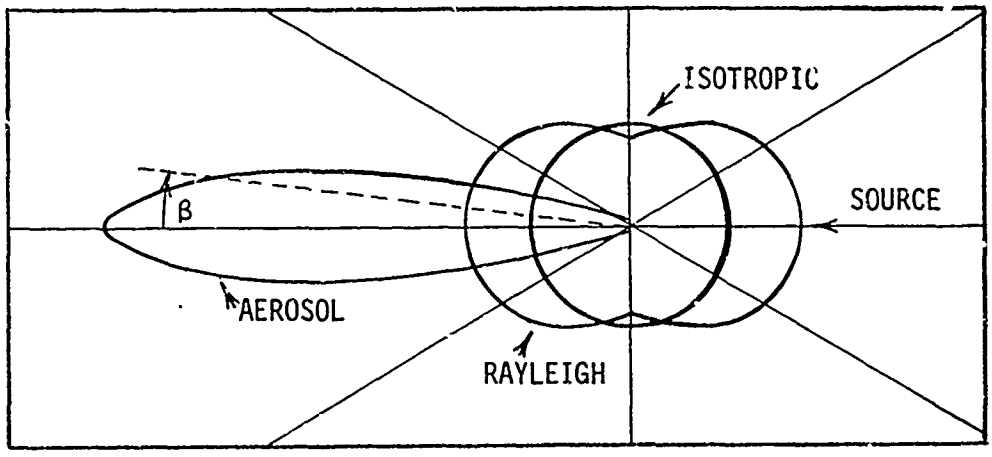

Fig. 2. Representative Scattering Patterns for Isotropic, Rayleigh, and Aerosol Particles

on wavelength enters due to the changing, with wavelength, of the scattering magnitude (and shape for the aerosol). For the different molecular (Rayleigh) components which cause scattering, this scattered intensity can be written as

$$I_{scattered} \propto \lambda^{-4}(1 + \cos^2\beta) \tag{18}$$

where λ is the wavelength and β is the scattering angle measured from the axis pointed in the direction away from the source of illumination. For aerosol scattering the dependence is not available in closed form without assumptions about the size and makeup of the particles. Since aerosols can be smoke particles, dust, water vapor haze, ice or snow, the specification of size and number density is very difficult. It is the task of measurement to model these parameters accurately so that calculations can be made to determine the scattering phase functions. These dependencies listed above indicate the complex nature of the path radiance.

Following the development by Duntley (Ref 7:2-5, Appendix A), the last two terms in Eq (6) may be called the path function $N_*(Z,\theta,\phi)$. Then

$$\frac{\partial N}{\partial z|\sec\theta|} = -\kappa(Z)N(Z,\theta,\phi) + N_*(Z,\theta,\phi) \tag{19}$$

where

$$N_*(Z,\theta,\phi) = \frac{\beta(Z)}{4\pi}\int_{\Omega'} p(Z,\hat{\Omega},\hat{\Omega}')N(Z,\hat{\Omega}')\, d\Omega' + Q'(Z,\Omega',\hbar\omega) \tag{20}$$

Duntley then points out that there exists for each point in the atmosphere a unique spectral radiance, the equilibrium radiance $N_q(Z,\theta,\phi)$, which is transmitted unchanged through the small volume $dz\, d\Omega$. From Eq (19), by setting $\partial N/(\partial z|\sec\theta|) = 0$,

$$N_q(Z,\theta,\phi) = \frac{N_*(Z,\theta,\phi)}{\kappa(Z)} \tag{21}$$

This shows that at each point along the path, the spatial rate of change of the spectral radiance is proportional to the difference between the spectral radiance $N(Z,\theta,\phi)$ and the equilibrium radiance $N_q(Z,\theta,\phi)$. That is,

$$\frac{\partial N(Z,\theta,\phi)}{\partial z|\sec\theta|} = -\kappa(Z)[N(Z,\theta,\phi) - N_q(Z,\theta,\phi)] \tag{22}$$

A dark object will tend to increase in spectral radiance and a light object will tend to decrease, toward the equilibrium radiance.

Analytic Approaches

We now consider some of the approaches to solving the problem, both analytic and by measurement. We will also consider the assumptions made in each.

Analytic Approach I: Sky-Ground Ratio (Duntley K Factor). Duntley originated the following approach in 1948 (Ref 2:179). It has been reiterated and used, though often incorrectly, many times since its origination (Ref 3:64 and Ref 4). Duntley develops the problem as follows (also see Middleton, Ref 3:64):

The geometry is shown in Fig. 3a. In this derivation all quantities are integrated over wavelength over the photopic or visual region. To avoid confusion we use the symbol $B(Z,\theta,\phi)$ to represent the brightness, the photometric equivalent of radiance. An equation for the change in radiance through the lamina dr is

$$\frac{dB(r)}{dr} = -[\alpha(r) + \beta(r)]B(r) + B^*(r) \tag{23}$$

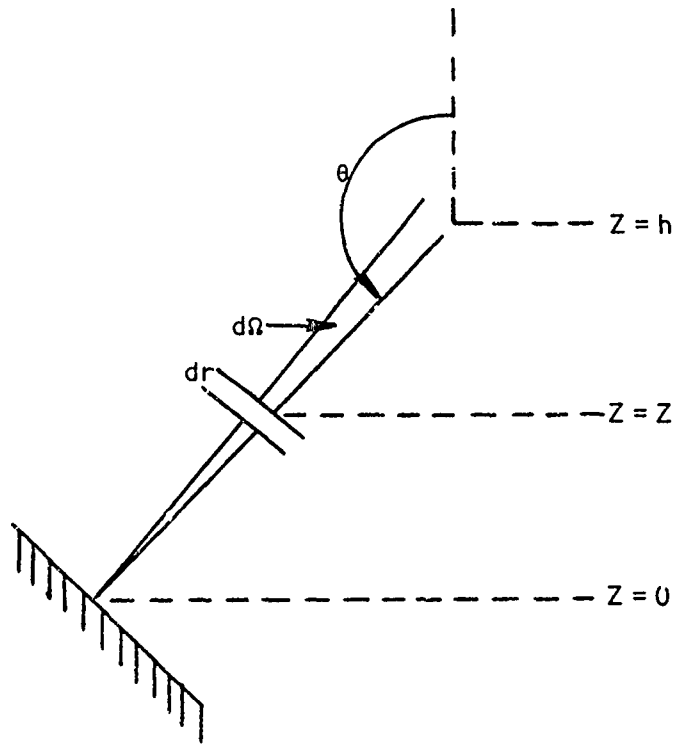

Fig. 3a. Inclined Path From Observer To Target-Background Scene

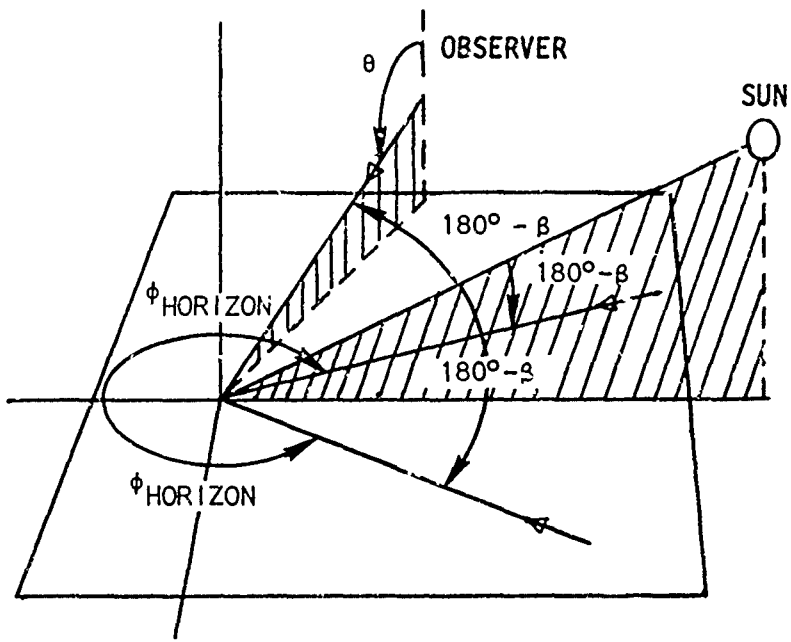

Fig. 3b. Horizontal Paths of Sight With Equal Scattering to That Along the Inclined Path to the Observer

Fig. 3. Geometry for Development of Duntley's Equation for the Reduction of Contrast by the Atmosphere

where

$B(r)$ is the radiance at the lower surface,

$\alpha(r)$ is the absorption coefficient (units 1/length),

$\beta(r)$ is the scattering coefficient (units 1/length)

$B^*(r)$ is the path radiance in the direction of the observer per unit length (power/area-ster-path length),

and

$$B^*(r) = \frac{\beta(r)}{4\pi} \int_{\Omega'} B(r,\theta',\phi') p(r,\hat{\Omega},\hat{\Omega}') \, d\Omega' \tag{24}$$

This expression for path radiance ignores any emission by the atmosphere, the Q' term from Eq (20) above. This assumption is very good in the visible region of the spectrum.

If B^* is everywhere proportional to β, the scattering coefficient, then Eqs (23) and (24) hold.

With the above assumptions one may proceed to assume that

$$\sigma(r) = \alpha(r) + \beta(r) = \sigma_0 f(r) \tag{25}$$

and

$$B^*(r) = B^*(0) f(r) \tag{26}$$

where σ_0 is the attenuation coefficient at the surface. This assumption, as Middleton points out, restricts one to the case where absorption is negligible compared to scattering. This is probably a good assumption if large amounts of pollutants are not present and also at relatively high sun angles. We then may write Eq (23) as

$$dB(r) = [-\sigma_0 B(r) + B^*(0)] f(r) dr \tag{27}$$

Integrating between B_0 and B_R and 0 and R,

$$\int_{B_0}^{B_R} \frac{dB(r)}{\sigma_0 B(r) - B^*(0)} = -\int_0^R f(r)dr \tag{28}$$

where R is the length of the slant path, B_0 is the radiance in the direction of interest at the source and B_R is the radiance at the receiver.

Solving, we have

$$\ln[\sigma_0 B_R - B^*(0)] - \ln[\sigma_0 B_0 - B^*(0)] = -\sigma_0 \bar{R} \tag{29}$$

where

$$\bar{R} = \int_0^R f(r)dr$$

which Duntley calls the "optical slant range." Then

$$\sigma_0 B_R - B^*(0) = [\sigma_0 B_0 - B^*(0)]e^{-\sigma_0 \bar{R}} \tag{30}$$

$$B_R = \frac{B^*(0)}{\sigma_0} + \frac{\sigma_0 B_0 - B^*(0)}{\sigma_0} e^{-\sigma_0 \bar{R}} \tag{31}$$

$$B_R = \frac{B^*(0)}{\sigma_0} (1 - e^{-\sigma_0 \bar{R}}) + B_0 e^{-\sigma_0 \bar{R}} \tag{32}$$

This is seen to be in the same form as Eq (7) with

$$\frac{B^*(0)}{\sigma_0} (1 - e^{-\sigma_0 \bar{R}})$$

equal to the path radiance and $e^{-\sigma_0 \bar{R}}$ equal to the transmittance. Proceeding with the same type of development for contrast transmission we obtain

$$\tau_C = \frac{C_R}{C_0} = \frac{1}{1 + \frac{B^*(0)}{\sigma_0 B_0} (e^{\sigma_0 \bar{R}} - 1)} \tag{33}$$

Next Duntley goes back to his differential Eq (23) as we did in Eq (21) and sets it equal to zero to get the equilibrium radiance:

$$B_q(r) = \frac{B^*(r)}{\sigma(r)} \tag{34}$$

Hence if the radiance is just equal to $B^*(r)/\sigma(r)$ it will not be altered with range. This is the concept of "optical equilibrium" (Ref 2:179). By the assumptions made above in Eqs (25) and (26),

$$\frac{B^*(r)}{\sigma(r)} = \frac{B^*(0)}{\sigma(0)} = B_{horizon} \tag{35}$$

since along any horizontal path of sight $B_q(r)$ is the radiance of the horizon sky in a particular direction provided that the sky is clear.

What is the direction along the horizon? Consider the downward looking path of sight as shown in Fig. 1. The sun is being scattered into the small solid angle $d\Omega$ in the direction $\hat{\Omega}$. From Fig. 2, the angle is described as β. One must look along the horizon in the direction such that the scattering angle is the same. The sun must make the same angle with the horizon path as it does with the inclined path. The reason for requiring clear skies is now additionally clear. This development will be valid only if single scattering of the sun is the prime cause of the path radiance $\frac{B^*(r)}{\sigma(r)}$. Then Eq (33) reduces to

$$\tau_c = \frac{1}{1 + \frac{B(\phi_{horizon} = \beta)}{{}_bB_0}(e^{\sigma_0 \bar{R}} - 1)} \tag{36}$$

$B(\phi_{horizon} = \beta)/{}_bB_0$ is the "sky-ground ratio." $B_{horizon}$ must be measured in a particular direction which may be specified as follows: If the spherical coordinate system shown in Fig. 1 is set up, then the cosine of the scattering angle for a path of sight in direction θ,ϕ is given by

$$\cos \beta = \cos \theta_0 |\cos \theta| + \sin \theta_0 \sin \theta \cos \phi \tag{37}$$

(see Appendix B for derivation), where

θ_0 is the zenith angle of the source,

θ is the receiver zenith angle,

ϕ is the azimuth from the sun ($\phi = 0$ when looking toward the sun),

and in the direction along the horizon for equal scattering $\phi_{horizon} = \beta$, $\theta = 90°$; thus

$$\cos \phi_{horizon} = \frac{\cos \beta}{\sin \theta_0} \tag{38}$$

where β is 0° when looking in the same direction as the ongoing sun rays. Clearly then, directions may exist such that $\cos \beta > \sin \theta_0$ in which case $\cos \phi_{horizon} > 1$ and $\phi_{horizon}$ is imaginary. Then $B(\phi_{horizon} = \beta)$ cannot be measured. Figure 3b shows a case where the directions exist.

If the direction exists, and we make all of the above assumptions, then $B(\phi_{horizon} = \beta)$ can be measured along with ${}_bB_0(\theta,\phi)$ and the sky-ground ratio determined. This $B(\phi_{horizon} = \beta)$ is then the non-spectral counterpart of the previously mentioned N_q of Eq (21), the equilibrium radiance for a path of sight.

Duntley gives a table of possible values of sky-ground ratio under some sky and background conditions. The variation of sky-ground ratio with sun angle and path of sight is not shown. As a matter of fact, calling the sky-ground ratio K, as do Bailey and Maudie (Ref 4) and others, is highly misleading since it implies that sky-ground ratio is invariant with source and receiver position. Actually, sky-ground ratio is a function of θ and ϕ, the path of sight, θ_0, the sun zenith; and the inherent background reflectance as Duntley points out (Ref 2:179).

This still leaves the determination of $\bar{R}$. Duntley does this by assuming an "optical standard atmosphere" in which the scattering and absorbing particle density decreases exponentially with altitude. The form which Duntley uses for particle density is (Ref 2:187):

$$N/N_0 = \exp (- Z/21,700) \tag{39}$$

where Z is the height above sea level in feet. Middleton uses (Ref 3:74):

$$N/N_0 = \exp(-Z/30,000) \tag{40}$$

as do Bailey and Mundie (Ref 4). See Fig. 1 for geometry. Since $Z = R|\cos\theta|$ and assuming that the f(r) in Eq (28) is N/N_0, then

$$\bar{R} = 21,700\,|\sec\theta|\left(e^{-R_1|\cos\theta|/21,700} - e^{-R_2|\cos\theta|/21,700}\right) \tag{41}$$

and for the observer looking at a target at sea level, the expression reduces to

$$\bar{R} = 21,700\,|\sec\theta|\left(1 - e^{-R|\sec\theta|/21,700}\right) \tag{42}$$

Physically $\bar{R}$ represents the slant path length which has the same number of particles as a path along the surface of length R.

The relation is then made by Duntley, using the earlier work of Koschneider (Ref 1), between the extinction coefficient and the "meteorological range." If the "meteorological range", V, is defined as the range at which a large black object is just visible against the horizon sky, and the threshold of apparent contrast for the eye is accepted as .02, then $\sigma_0 = 3.912/V$. Frequent use is made of the relation $\sigma_0 = 3/V$ in which the eye is assumed to have a .05 threshold of contrast. Then the contrast transmission can be expressed in the analytic form

$$\tau_c = \frac{1}{1 + K(e^{+\sigma_0\bar{R}} - 1)} \tag{43}$$

where $\bar{R}$ is given in Eq (42) above, and

$$K = \frac{B(\phi_{horizon} = \beta)}{{}_bB_0(\beta,\phi)}$$

Bailey and Mundie (Ref 4) give a nice treatment showing some of the effects of different sky-ground ratios, and meteorological range on contrast transmission. The dependence of contrast transmission on air-transmission $T = e^{-\sigma_0\bar{R}}$ for various values of sky-ground ratio can be seen from Fig. 4.

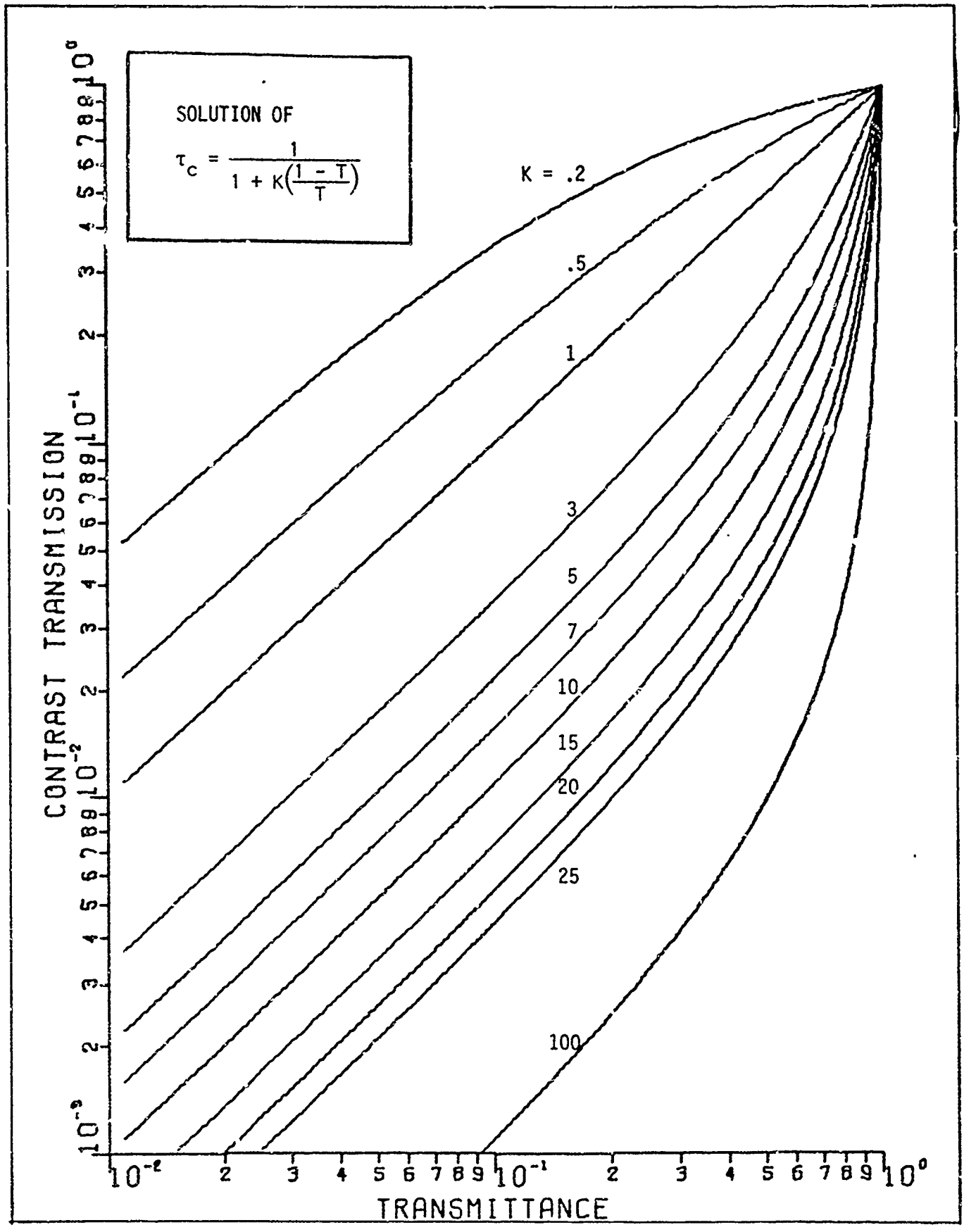

Fig. 4. Dependence of Contrast Transmission Upon Air-Transmittance For Differing Values of Sky-Ground Ratio, K

Note the very strong dependence on sky-ground ratio for a constant value of air-transmittance. One key problem then is to choose the sky-ground ratio. Duntley gives the data shown as Table I (Ref 2:184). Middleton

TABLE I
Sky-Ground Ratios Suggested by Duntley in 1948

Sky Condition	Ground Condition	Sky-Ground Ratio
Overcast	Fresh snow	1
Overcast	Desert	7
Overcast	Forest	25
Clear	Fresh snow	.2
Clear	Desert	1.4
Clear	Forest	5

observes that from Duntley's table it appears that the sky-ground ratio is approximately the reciprocal of the surface albedo under an overcast sky and 1/5 of the reciprocal of the albedo under clear skies. Duntley gives no justification for the numbers he presents. The use of this table and Middleton's observations on it are a major cause of error in predictions using this theory.

Calculations have been made from the RRA Monte Carlo data to yield contrast transmission (Ref 8). By using the computed contrast transmission and known air-transmittance for that model atmosphere, the sky-ground ratio may be computed from Eq (43) for different sun positions, receiver positions and surface albedos. The results are presented graphically in Figs. 5 and 6. In Fig. 5 the computed average value over altitude of sky-ground ratio is plotted as a function of albedo for three receiver

zenith angles and two visibilities. An isotropic source at the top of the atmosphere is assumed. The dependence which Duntley shows with albedo is clear but the computed valuesfor the low albedo case of the forest (albedo = .05) or intermediate albedo of sand are considerably lower than Duntley predicts. Note also the variation of sky-ground ratio with the amount of haze present. As visibility decreases,the value of sky-ground ratio increases for a constant albedo. For a plane parallel source (i.e. the sun) there is also a marked variation with solar zenith angle as shown in Fig. 6. Here the computed average (over altitude and azimuth) sky-ground ratio is plotted against solar zenith angle for three receiver zenith angles. Visibilities of 3 and 25 KM are used and albedos of .1 and .9 are shown. Note for the low albedo the more pronounced effect of solar zenith. As the sun approaches the horizon, the sky-ground ratio increases sharply. A similar effect as in the isotropic case of increased sky-ground ratio with decreasing visibility is also noted. In general the sky-ground ratios are less spread than Duntley would indicate in Table I. The high albedos produce slightly larger sky-ground ratios than predicted and the lower albedos produce lower sky-ground ratios. The variation of sky-ground ratio with respect to azimuth from the sun can also be shown but the Monte Carlo data does not lend itself to this type of presentation, as will be discussed later.

Several other factors should be pointed out about sky-ground ratio. In general, the sky-ground ratio is not a constant with altitude, although it may be over a limited altitude regime. This can be seen from the RRA data, but the altitudes presented in the original report are .5, 2, 4, 6, 10 and 50 KM. These are rather widely spaced for use at low dive angles and low altitudes. Values of computed sky-ground ratio from several flights

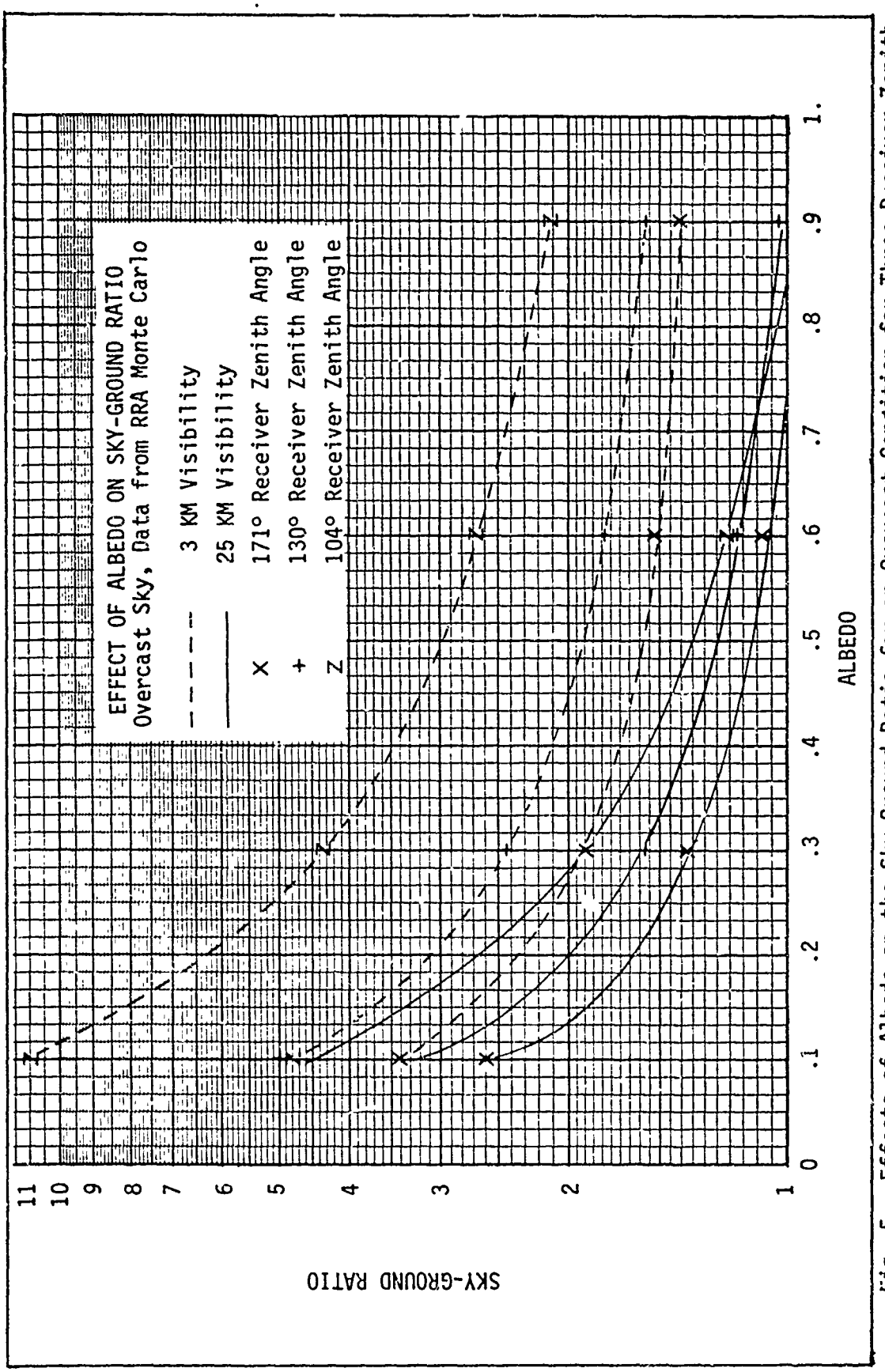

Fig. 5. Effects of Albedo on the Sky-Ground Ratio for an Overcast Condition for Three Receiver Zenith Angles. Data from RRA Monte Carlo Calculations.

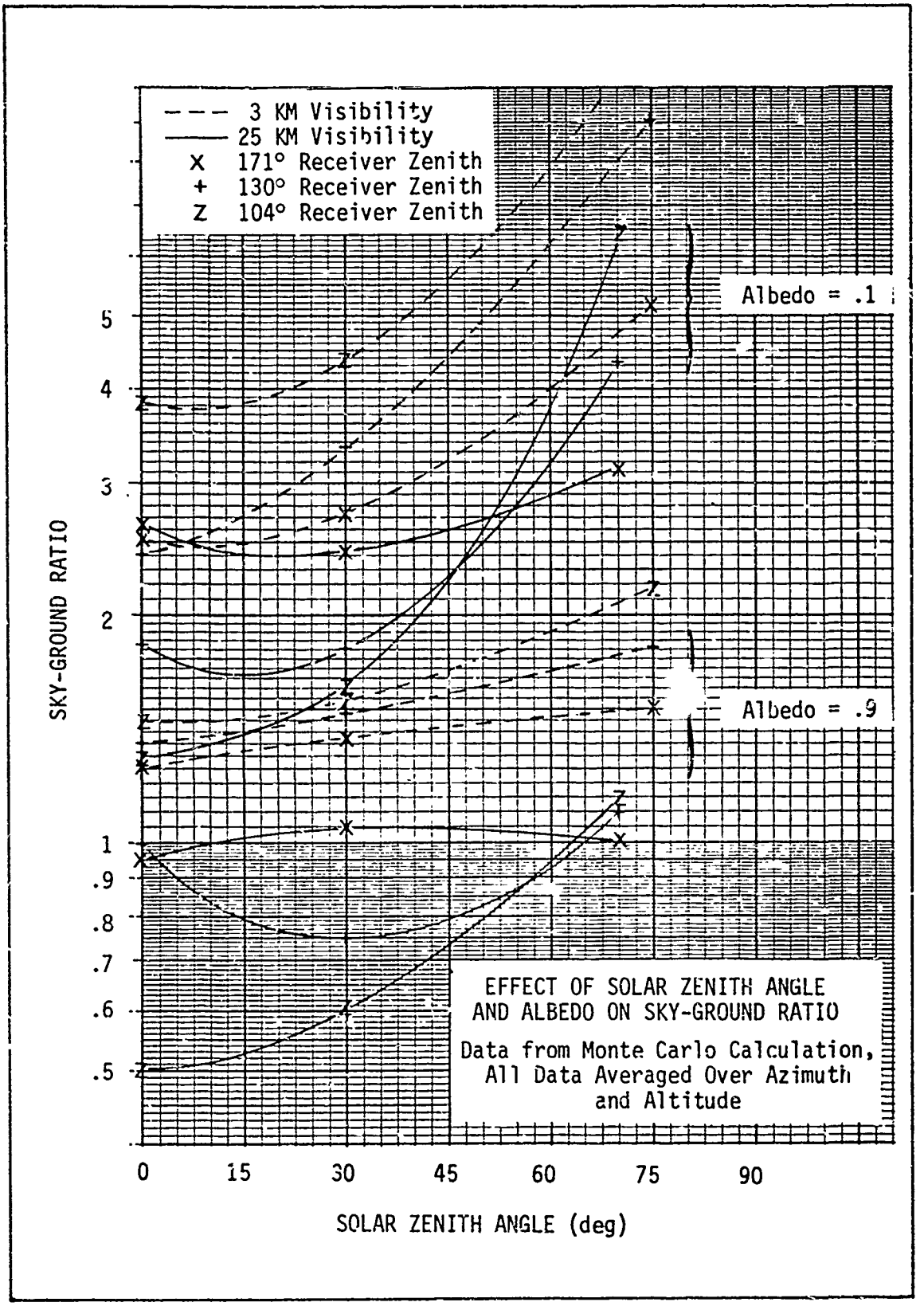

Fig. 6. Effects of Solar Zenith Angle and Albedo on the Sky-Ground Ratio for Two Visibilities. Three Receiver Zenith Angles Are Shown. Data is from Monte Carlo Calculation.

conducted in Germany in May and June of 1971 are shown in Figs. 7 through 10. The data for these calculations were received from Dr. Robert Fenn of the Air Force Cambridge Research Laboratories (Ref 9). The weather and sun conditions under which the flights were conducted are shown in Table II.

TABLE II
Geophysical and Weather Conditions for Haven View Flights

Flight	Date	Solar Zenith (Avg)	Altitudes Covered	Sky Condition	Albedo	Visibility (Reported)
c-134	05/25/71	55°	.3-2.4 KM	Broken	.07	33-24 KM
c-137	05/28/71	50°	.3-3 KM	Broken	.04	15-20 KM
c-138	05/29/71	36°	.3-5.1 KM	Scattered	.03	13-30 KM
c-139	06/03/71	38°	.3-5.1 KM	Scattered	.04	30-20 KM
c-142	06/06/71	36°	.3-5.1 KM	Scattered	.05	7-10 KM

The method of data collection is described in Ref 7 and will be discussed briefly later in this chapter and in Chapter III. Given the data necessary to compute contrast transmission, and the air-transmittance from in-flight measurements, the sky-ground ratio may be computed. The values averaged over the altitude regime are displayed in Figs. 7 through 10. Figures 7 and 8 show the values of sky-ground ratio in the plane of the sun plotted against receiver zenith angle. Flights with similar solar zenith angles have been grouped. Figures 9 and 10 show the plane perpendicular to the sun. There is some agreement in shape between the grouped data, but the varying cloud conditions could cause some of the notable differences. Note however the range of values of the sky-ground ratio, again supporting the use of lower values than shown in Table I. Note also

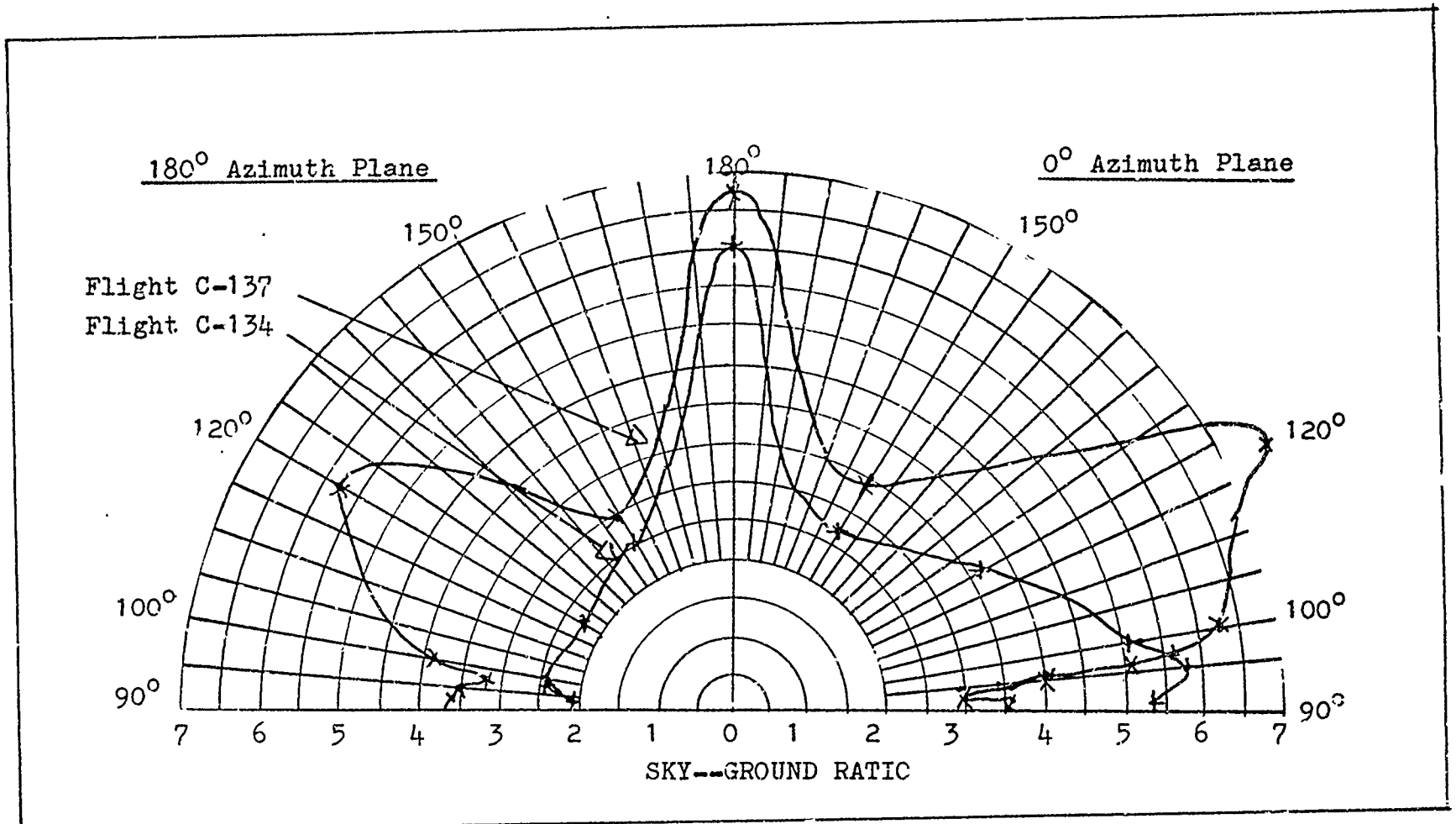

Figure 7. Sky-ground ratio versus receiver zenith angle in the solar plane. Data taken during Project Haven View.

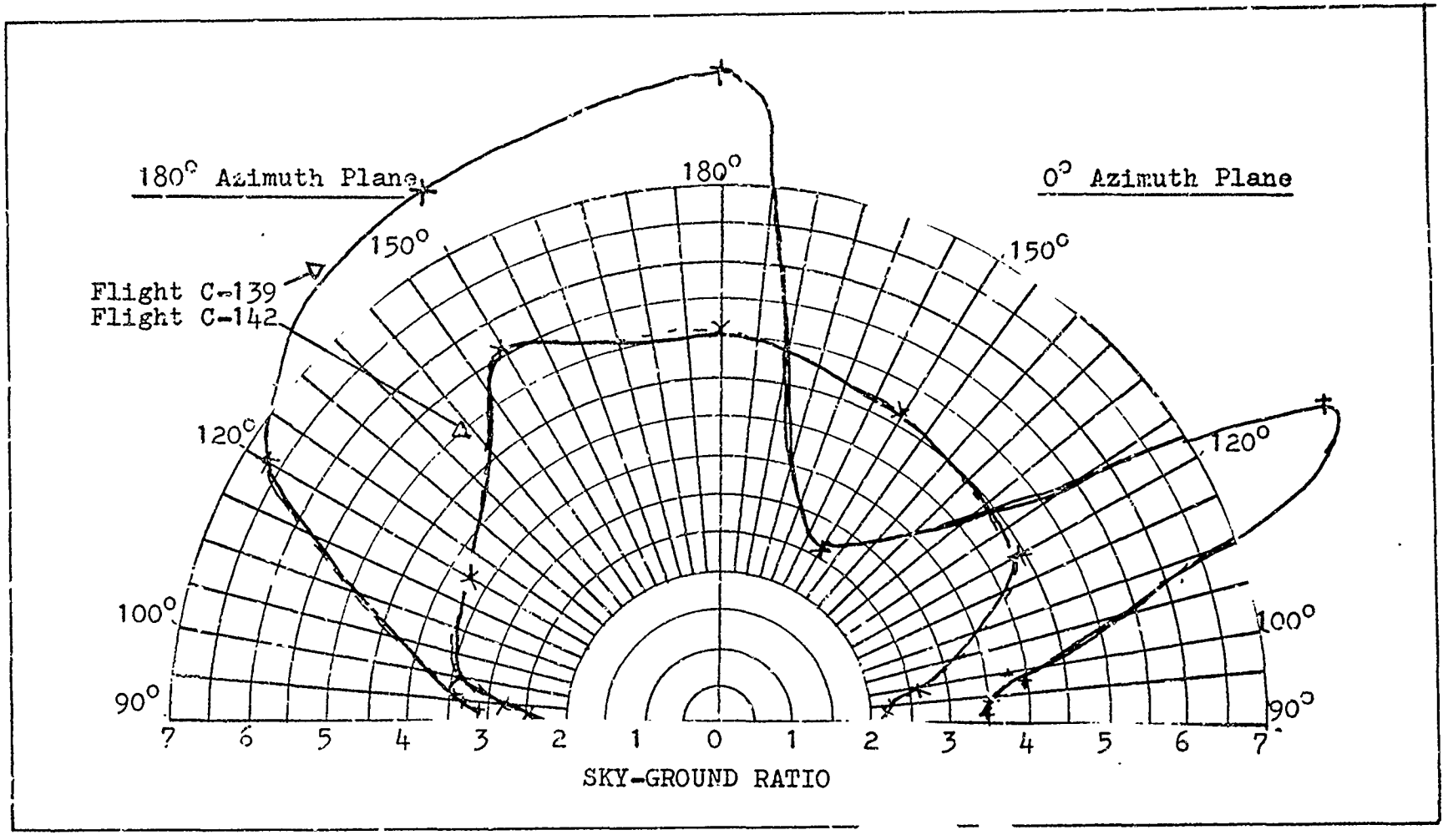

Figure 8. Sky-ground ratio versus receiver zeni the solar plane. Data taken during Project Haven View.

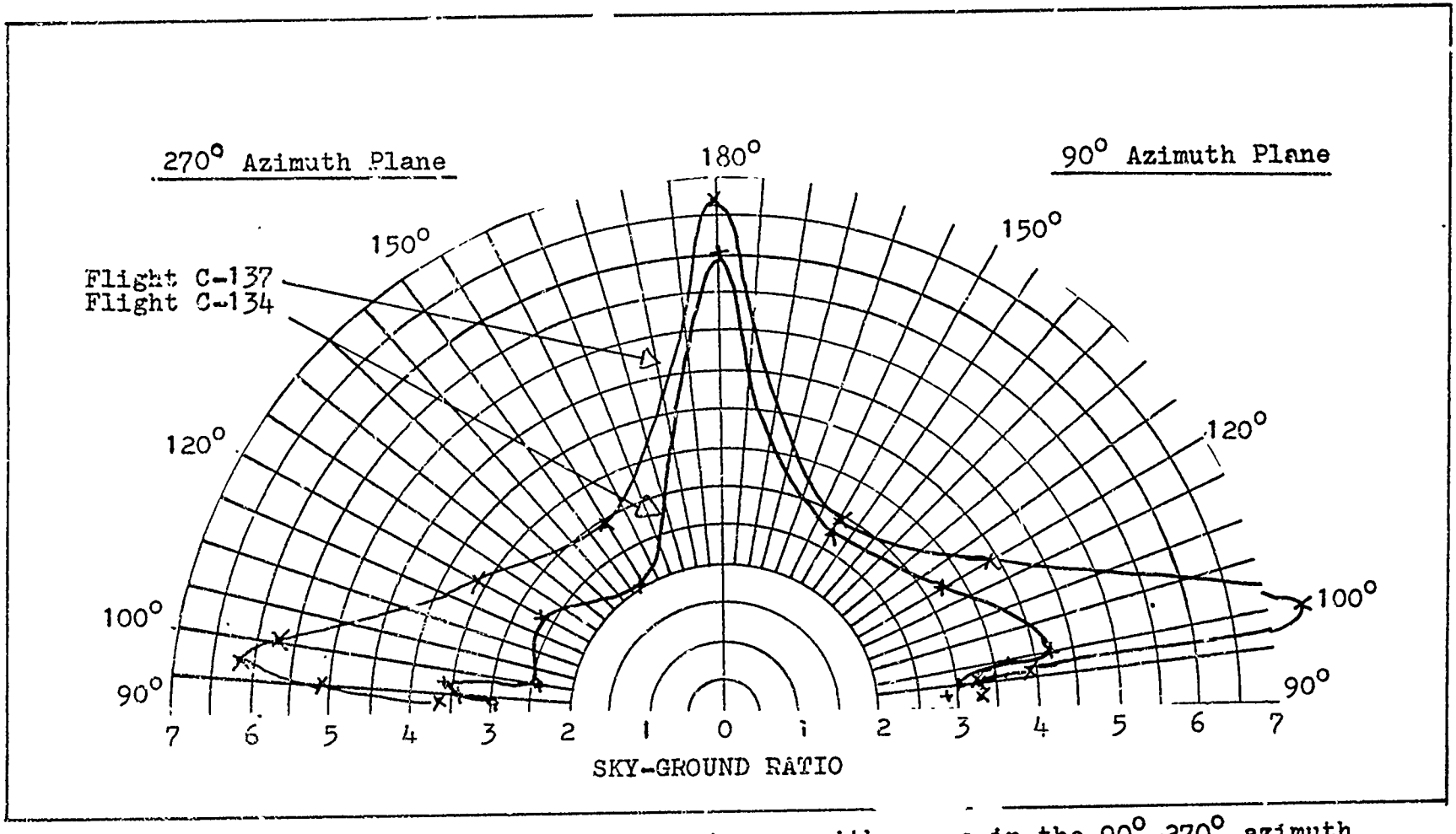

Figure 9. Sky-ground ratio versus receiver zenith ..le in the 90°-270° azimuth plane. Data taken during Project Haven View.

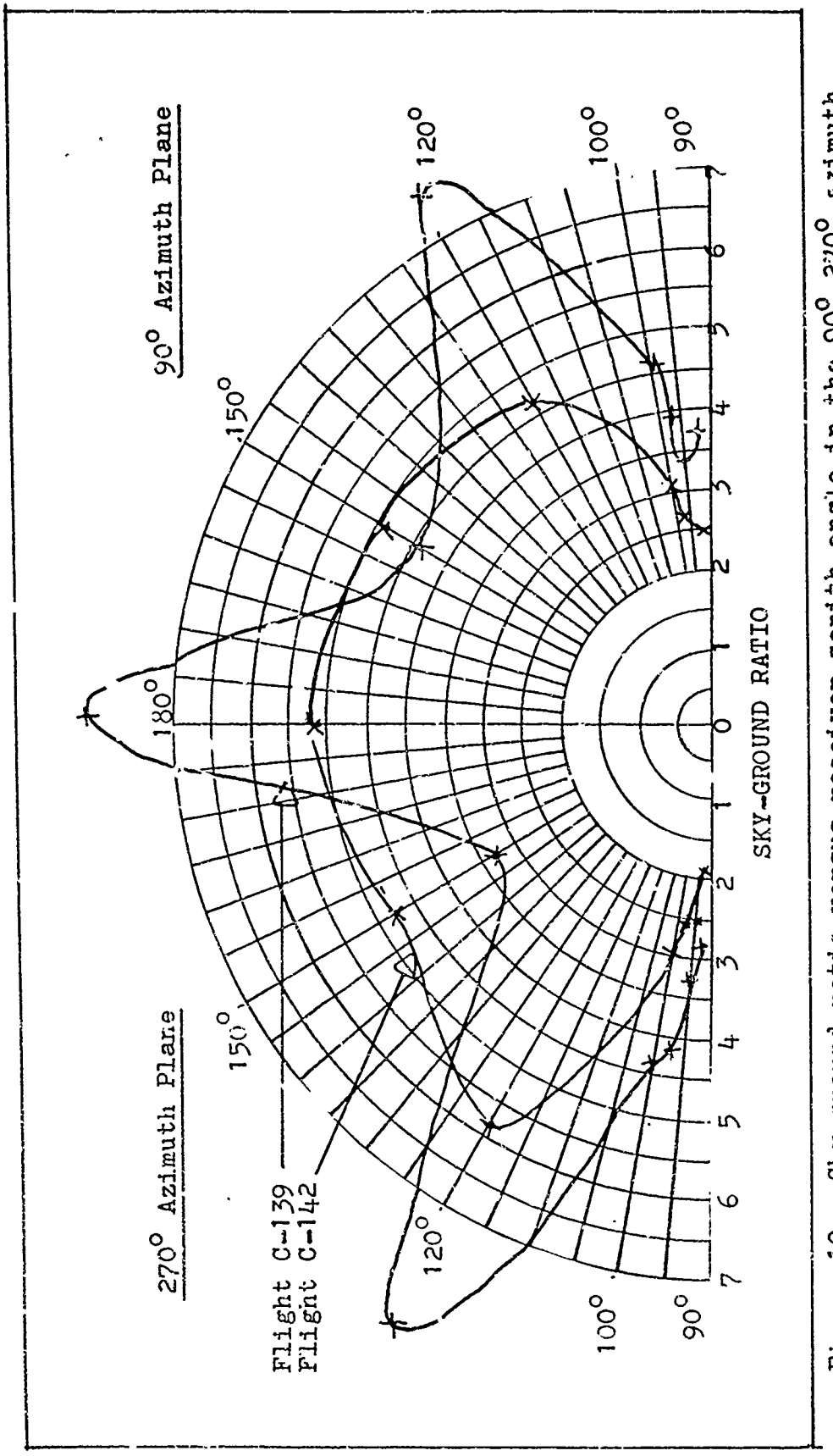

Figure 10. Sky-ground ratio versus receiver zenith angle in the 90°-270° azimuth plane. Data taken during Project Haven View.

that in most of the cases the sky-ground ratios tend to approach a lower value toward the horizon. In the limit where Dunley's theory reduces to Koschneider's, the sky-ground ratio would be 1.

Despite the many limitations of the sky-ground ratio and the fact that it usually cannot be measured, as will be shown in Chapter VI, it can be computed in the way mentioned above from the more complete models. Tables of values generated from the Monte Carlo data for various solar zeniths, visibilities, receiver positions, and albedos, and wavelengths are shown in Appendix C. Sky-ground ratio values computed from the RRA model are presented in Table III for the following conditions.

TABLE III

Parameters for Sky-Ground Ratio Computation from Monte Carlo Data

Sky Condition	Visibility	Albedo	Solar Zenith	θ	ϕ
Clear	.55 μm 3 KM	.1,.9	0°,30°,75°	12 values	22.5°,67.5° 112.5°,157.5°
	" 25 KM	"	0°,30°,70°	"	"
Overcast	.55 μm .65 μm 3 KM	.1,.3,.6,.9	Isotropic	"	-
	" 25 KM	"	"	"	-

Before accepting the Duntley model, with the new sky-ground ratios, some comments must be made about relating the visibility to the transmittance through the "optical standard atmosphere." The equation which Duntley gives (Eq 42) and Middleton and Bailey and Mundie repeat, but change 21,700 to 30,000 feet, appears to be highly pessimistic in predicting transmission of the atmosphere. Work reported by Elterman (Ref 10:7-1) uses an aerosol particle density function of $N/N_0 = \exp(Z/1.2\ KM)$ up to 10 KM. This shows

that the aerosol particle density drops much more sharply than the values predicted by Duntley in Eq (42). This can have a large effect on the prediction of contrast transmission at the lower altitudes. Elterman gives an excellent treatment of the problem of transmittance prediction as a function of surface meteorological range in Ref 11. It appears that Duntley has lumped molecular (Rayleigh) scattering with aerosol scattering in coming up with his optical slant range. Middleton and Bailey and Mundie continue the error, although they point out that all atmospheres may not look like the standard atmosphere. Using the development of Elterman (Ref 11) and the concept of optical thickness mentioned earlier, the spectral air-transmittance may be developed in analytic form as follows:

The transmission over a slant path from Eq (17) is

$$T_{h_1-h_2}(\Delta h,\lambda,V_\eta) = \exp\left\{-\left[\tau_{ext}(h_2,\lambda,V_\eta) - \tau_{ext}(h_1,\lambda,V_\eta)\right]|\sec\theta|\right\} \qquad (44)$$

where (h,λ,V_η) refers to an altitude, wavelength, and visibility condition. τ_{ext} is the optical thickness of the atmosphere from the surface to altitude h. But

$$\tau_{ext}(h,\lambda,V_\eta) = \tau_{ext_R} + \tau_{ext_p} + \tau_{ext_{abs}} \qquad (45)$$

where R, p, and abs refer to extinction due to Rayleigh scattering, aerosol scattering and absorption respectively. By definition

$$\tau_{ext}(h,\lambda,V_\eta) = \int_0^h \beta(h,\lambda,V_\eta)dh \qquad (46)$$

for Rayleigh particles

$$\beta_R(h,\lambda,V_\eta) = \beta_R(h,\lambda) = \sigma_R(\lambda,h)n_R(h)$$

since the molecular particle density does not depend on visibility. $\sigma_R(\lambda,h)$ is the scattering cross section for molecules. Also assuming uniform mixing,

$$\sigma_R(\lambda,h) = \sigma_R(\lambda,h=0)$$

So

$$\tau_{ext_R}(h,\lambda,V_\eta) = \sigma_R(\lambda)\int_0^h n_R(h)dh \tag{47}$$

We may now use the U.S. Standard Atmosphere, 1962 for an expression for number density of molecules in the standard atmosphere: $N/N_0=\exp(-Z/9.2\ KM)$. Then

$$\tau_{ext_R}(h,\lambda) = H_R\beta_R(\lambda,h=0)[1 - \exp(-Z/H_R)] \tag{48}$$

where H_R = 9.2 KM is the scale height. Note that this is not a function of visibility. Elterman gives $\beta_R(.55\ \mu m)$ = .0116 1/KM. Curves from Ref 12 show the Rayleigh aerosol and ozone attenuation coefficient as a function of wavelength. The data is presented in Fig. 11. For aerosols, a model presented by Elterman (Ref 10:7-3) shows a number density for aerosols

$$N/N_0 = e^{-Z/1.2\ KM} \tag{49}$$

up to 10 KM altitude. The density above that is not easily approximated.

The models presented by Elterman for low visual ranges in Ref 11 modify this slightly, attributing the above to clear conditions and add haze below 5 KM. Here

$$N/N_0 = e^{-Z/H_p(V_\eta)} \tag{50}$$

where H_p is a scale height for the particular visibility V_η, then

$$\beta(h,\lambda,V_\eta) = \beta_p(h_0,\lambda,V_\eta)e^{-h/H_p(V_\eta)} \tag{51}$$

and

$$\tau_{ext_p}(h,\lambda,V_\eta) = H_p(V_\eta)\beta_p(h_0,\lambda,V_\eta)(1 - e^{-h/H_p(V_\eta)}) \tag{52}$$

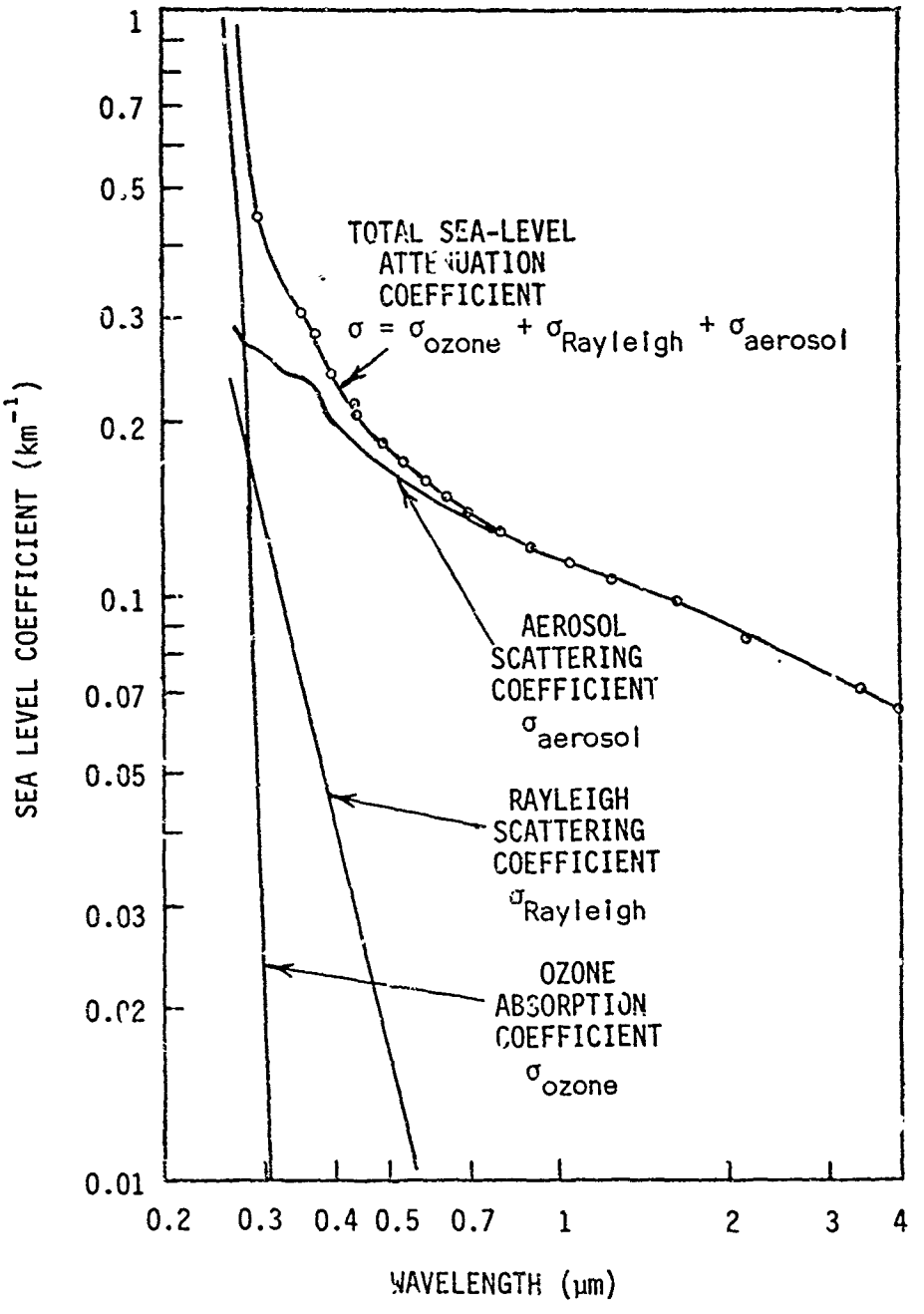

Fig. 11. Calculated Atmospheric Attenuation Coefficients for Horizontal Transmission at Sea Level in a Model Clear Standard Atmosphere. Absorption at the Longer Wavelengths Due to H_2O and CO_2 is not shown.

Neglecting absorption and in the photopic region, we may assume that the air-transmittance at $\lambda = .55$ μm is representative of the photopic region. Then

$$K_0(.55\ \mu m) = \beta_p + \beta_R = \sigma_0 = \frac{3.912}{V}$$

So

$$\tau_{ext_p}(h,\lambda,V_\eta) = H_p\left(\frac{3.912}{V} - \beta_R\right)\left(1 - e^{-h/H_p(V_\eta)}\right) \qquad (53)$$

For specific wavelengths the curve in Fig. 11 may be used to find $\beta_p(\lambda)$ and $\beta_R(\lambda)$ or consult Ref 10. Elterman gives the scale heights for the visibilities which he models as follows:

V_η (KM)	H_p (KM)
2	.84
3	.90
4	.95
5	.99
6	1.03
8	1.10
10	1.15
13	1.23

It appears appropriate to use 1.? KM as the scale height for visibilities between 13 and 25 KM and also above that. Note that the scale heights for the lower visibilities are valid only up to 5 KM altitude (Ref 11). Above 5 KM the decrease is no longer exponential (see Ref 13).

Up to 5 KM in altitude, the transmittance in the optical standard atmosphere may be written as

$$T_{h_1-h_2}(\Delta h,\lambda,V_\eta) = \exp\left\{-\left[H_R\beta_R(\lambda)\left(1 - e^{-h_2/H_R}\right) + H_p\left(\frac{3.912}{V} - \beta_R(\lambda)\right)\right.\right.$$
$$\times\left(1 - e^{-h_2/H_p(V_\eta)}\right) - \beta_R(\lambda)H_R\left(1 - e^{-h_1/H_R}\right)$$
$$\left.\left. - H_p\left(\frac{3.912}{V} - \beta_R(\lambda)\right)\left(1 - e^{-h_1/H_p(V_\eta)}\right)\right]|\sec\theta|\right\} \quad (54)$$

Combining,

$$T_{h_1-h_2}(\Delta h,\lambda,V_\eta) = \exp\left\{-\left[\beta_R(\lambda)H_R\left(e^{-h_1/H_R} - e^{-h_2/H_R}\right) + H_p\left(\frac{3.912}{V} - \beta_R(\lambda)\right)\right.\right.$$
$$\left.\left.\times\left(e^{-h_1/H_p(V_\eta)} - e^{-h_2/H_p(V_\eta)}\right)\right]|\sec\theta|\right\} \quad (55)$$

where $h_1 < h_2$.

Assuming that $h_1 = 0$, then

$$T_{0-h}(\Delta h,\lambda,V_\eta) = \exp\left\{-\left[\beta_R(\lambda)H_R\left(1 - e^{-h/H_R}\right) + H_p\left(\frac{3.912}{V} - \beta_R(\lambda)\right)\right.\right.$$
$$\left.\left.\times\left(1 - e^{-h/H_p(V_\eta)}\right)\right]|\sec\theta|\right\} \quad (56)$$

This expression may be compared with Eq (42) noting that the Rayleigh optical thickness is the same, but the sizable correction of using a scale height of approximately 1.2 in place of 6.41 or 9.2 as used by Middleton to describe aerosol extinction.

Comparison w. data presented by Elterman in Ref 10 for a 23 KM atmosphere and in Ref 11 for a 3 KM atmosphere shows good agreement between the formula given above and the predictions based on the data presented at incremental altitudes. At or below 5 KM and at slant ranges less than 20 KM, the percentage of error between the two methods is less than 14% even at the

shallow dive angle of 2.8°. The agreement is generally much better typically less than 5% for both atmospheres. Thus using the "modified optical standard atmosphere" above one can directly relate visibility to transmittance and use the Duntley sky-ground ratio concept.

Analytic Approach II: Directional Path Reflectance R*. A very interesting and promising approach to the problem has been pointed out by Duntley (Ref 7:Appendix D) and also independently by others. Starting with the same basic equation for contrast transmission, Eq (13), Duntley suggests that one divide the numerator and denominator of the second term in the denominator by $\frac{H}{\pi}(Z_t,d)T(Z,\theta)$, where $H(Z_t,d)$ is the spectral irradiance on an upward facing, horizontal plate at the target altitude, d indicating downwelling; and $T_r(Z,\theta)$ is the transmittance over the slant path of interest. The equation now has the form

$$\tau_c(Z,\theta,\phi) = \left[1 + \frac{\pi N_r^*(Z,\theta,\phi)/H(Z,d)T_r(Z,\theta)}{\pi_b N_0(Z,\theta,\phi)/H(Z,d)}\right]^{-1} \qquad (57)$$

where all terms are spectral. The denominator of the second term, as Duntley points out is the "inherent directional spectral reflectance" of the background (Ref 7:Appendix D). He designates this by ${}_bR_0(Z_t,\theta,\phi,\theta',\phi')$ where θ',ϕ' refer to the zenith angle and outward normal to the reflecting surface. Note that this value would be the same as the albedo for a diffusely reflecting or Lambertian surface. Duntley calls the numerator of the second term the "directional path reflectance." Thus the equation now reduces to the much simpler appearing expression,

$$\tau_c(Z,\theta,\phi) = \{1 + [R_r^*(Z,\theta,\phi)/{}_bR_0(Z_t,\theta,\phi)]\}^{-1} \qquad (58)$$

where

$$R_r^*(Z,\theta,\phi) = \frac{\pi N^*(Z,\theta,\phi)}{H(Z_t,d)T_r(Z,\theta)} \tag{59}$$

Thus if one knows the directional reflectivity of the background, or a range of values for it, then the contrast transmission is uniquely specified by the directional path reflectance. The dependence may be illustrated by the graph in Fig. 12 adapted from Duntley (Ref 7:Appendix D). Here, contrast transmission has been plotted as a function of directional path reflectance for several values of background reflectance. Note that for a given background directional reflectance, the contrast transmission decreases rapidly with directional path reflectance although it is log-linear over a reasonable range. But note also the relation of contrast transmission to background reflectance for a fixed directional path reflectance.

If one can determine the directional path reflectance, the problem of contrast transmission may be more simply treated.

As an added point here it should be pointed out that the directional background reflectance is not in most cases a constant as for a diffuse surface, nor is it purely specular like a mirror. It lies somewhere in between. Data will be referenced that shows rather large variations in directional reflectance of background or target materials, thus showing a strong variation of contrast transmission unless the directional path reflectance varies at the same rate. This really asks whether the path radiance $N^*(Z,\theta,\phi)$ varies proportionately to the directional background reflectance. Duntley makes the statement that the path radiance depends primarily upon the atmosphere and the position of the sun and only secondarily on the ground and thus the directional path reflectance is only mildly affected by the background (Ref 7:Appendix D). This appears reasonable, since the solar radiance is always much higher than reflected

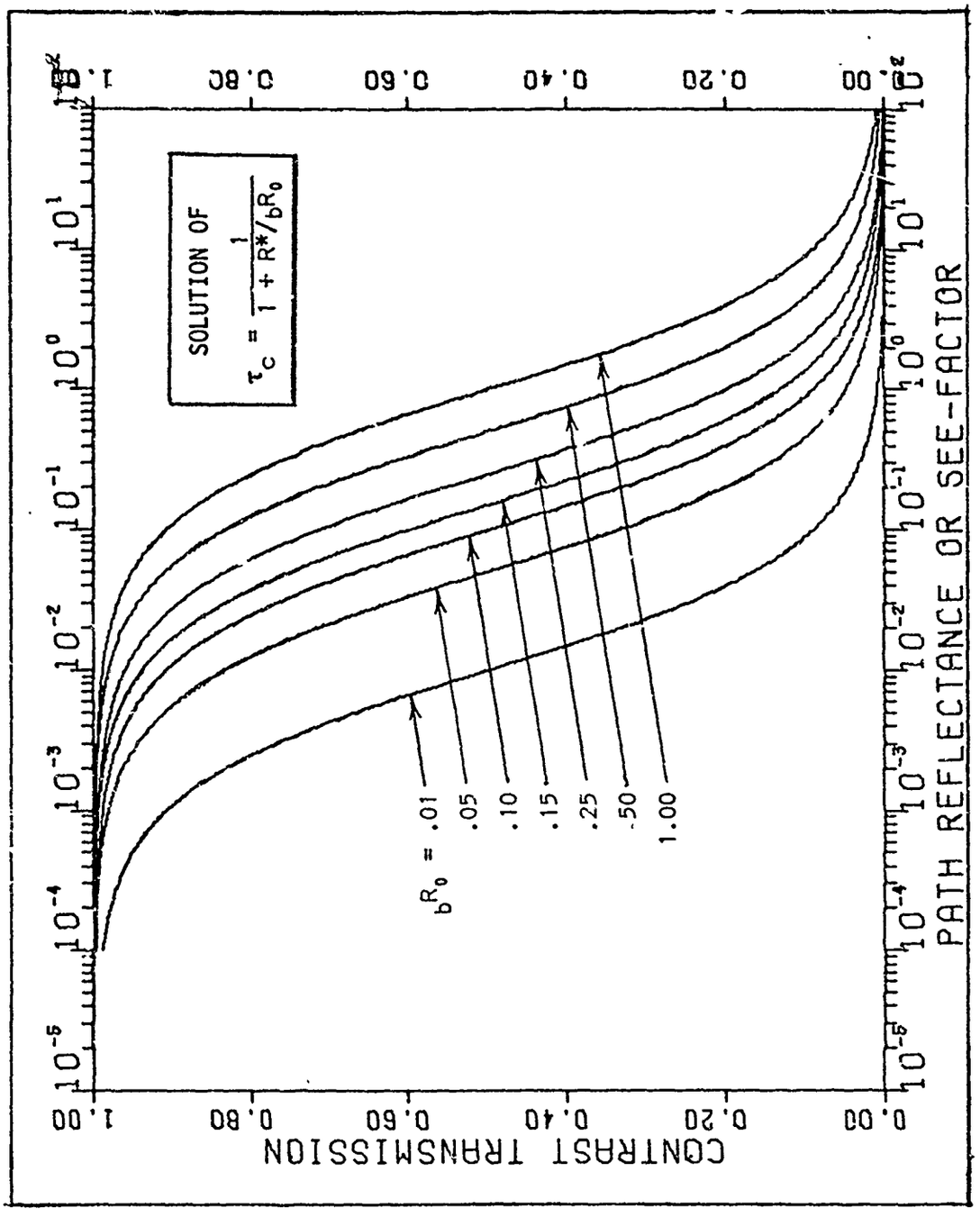

Fig. 12. Dependence of Contrast Transmission Upon Directional Path Reflectance, R*, for Differing Values of Inherent Directional Background Reflectance

radiance from terrain, unless an extremely specular surface is encountered. Thus it seems reasonable that the directional path reflectance is controlled with regard to the ground's effect by the overall scene albedo and not the directional background reflectance. Thus the strong effect of directional background reflectance on contrast transmission can be seen from Eq (58). This approach will be discussed in detail in Chapter III.

Numerical Calculation Methods

The solution of Eq (13), the basic equation for contrast transmission through the atmosphere, requires the knowledge of three basic parameters: the path radiance $N^*(Z,\theta,\phi)$, the transmission $T(Z,\theta)$, and the radiance from the background ${}_bN_0(Z,\theta,\phi)$. Duntley introduced the idea of the equilibrium radiance and optical standard atmosphere to bypass the difficulty of measuring these values at each point in space. When the horizon direction did not exist or the skies were not clear, there was no choice but to measure or do elaborate mathematical calculations. The purpose of this section will be to briefly describe some of the methods of calculation which are used to calculate path radiance, transmission, and radiance from the background.

With the advent of the digital computer, it has become possible to do the complex calculations indicated by Eq (6) or integral forms of that equation. There are several models which exist. They have been designed for differing purposes and contain differing amounts of additional capabilities above the calculations of path radiance, atmospheric transmission, and radiance from the target or background. Information and in many cases the programs themselves for several of the models can be obtained from the developing company, the Air Force Avionics Laboratory, Wright-Patterson AFB,

Ohio, or from the Air Force Cambridge Research Laboratory, Hanscom AFB, Massachusetts.

The names of some of the existing programs are listed below; two of the models and the method in which they were used will be discussed in brief detail.

1. Photographic Reconnaissance Systems Analysis (PRESAC): Data Corporation.
2. Evaluation of Optical Haze on Atmospheric Contrast: Vidya Corporation (Ref 14).
3. Contrast Transmission Data for Clear and Hazy Model Atmospheres: Radiation Research Associates (Ref 8).
4. MARSAM Model: Honeywell Aeronautical Division.
5. Aerial Photographic Energy Model: Philco Ford Corporation (Ref 15).
6. University of Michigan Atmospheric Model (Ref 5).
7. Penetration Survivability Assessment Model (PENSAM): Honeywell Aeronautical Corporation.
8. Atmospheric Transmission Model: Air Weather Service (Ref 16).

Only the third and eighth models listed will be discussed, but information on all the above may be found in the references.

Contrast Transmission for Clear and Hazy Model Atmospheres: Radiation Research Associates. This model was used to calculate the optical parameters required by Monte Carlo methods. The work was done for the Optical Physics Laboratory, Air Force Cambridge Research Laboratory.

Calculations of contrast transmission are reported for two model atmospheres, one with a surface meteorological range of 25 KM (clear), and one with a surface meteorological range of 3 KM (hazy) (Ref 8) A diffuse reflecting surface is assumed with albedos of .1, .3, .6, and .9. Wavelengths between .35 μm, and .95 μm are used. Altitudes of .5 KM, 2 KM, 4 KM, 6 KM, 10 KM and 50 KM are reported. Twelve downlooking receiver angles

and 7 solar altitudes are used. Azimuths averaged over 45° centered at 22.5°, 67.5°, 112.5°, and 157.5° are reported.

In addition, a plane isotropic sour[illegible]he top of the atmosphere simulating an overcast is assumed and v[illegible]es of contrast transmission are reported for the same geometrical parameters as listed above.

Table IV briefly describes the models used for the atmospheres, for comparison with the AWS model discussed later. The data has been taken from Ref 8.

Atmospheric Contrast Transmission Calculations:

The same formulation as given above in Eqs (8), (9), and (13) is used to define contrast and contrast transmission. Path radiance $N^*(Z,\theta,\phi)$ and background radiance ${}_bN_0(Z,\theta,\phi)T(Z,\theta)$, (called "ground reflectance" in Ref 8) are calculated from the light scattered intensities, $N(\theta_0,\lambda,\text{albedo},Z,\theta,\phi)$, where the scattered radiance is the total amount of spectral radiance arriving at Z in direction θ,ϕ. $N(\theta_0,\lambda,\text{albedo},Z,\theta,\phi)$ are calculated from the Monte Carlo programs described in Ref 17. N^* and ${}_bN_0T$ are calculated from N as follows:

The scattered spectral irradiance H_s incident on the background surface is

$$H_s(\theta_0,\lambda,\text{albedo},Z_+) = \int_0^{2\pi}\int_0^{\pi/2} N(\theta_0,\lambda,\text{albedo},Z_+,\theta,\phi)\cos\theta\sin\theta\, d\theta d\phi \qquad (60)$$

The background reflected spectral radiance in the direction $\hat{\Omega}$ that reaches the receiver at altitude Z is given by

$${}_bN_0(\theta_0,\lambda,\text{albedo},\theta)T(Z,\theta) = \left\{H_s(\theta_0,\lambda,\text{albedo},Z_+) + \exp\left[-\tau_{ext}(Z=50\text{ KM})\sec\theta_0\right]\right\} \times \left(\frac{\text{albedo}}{\pi}\right)\exp\left[-\tau_{ext}(Z)\,|\sec\theta|\right] \qquad (61)$$

TABLE IV

Atmospheric Parameters for Radiation Research Associates Monte Carlo Calculations

Parameter	3 KM Atmosphere	25 KM Atmosphere
Layers	Up to 50 plane parallel	Up to 50 plane parallel
Rayleigh attenuation coefficient	From Elterman (Ref 10) for clear standard atmosphere	From Elterman (Ref 10) for clear standard atmosphere
Ozone absorption coefficient	Same as above	Same as above
All other absorption	Neglect	Neglect
Aerosol particles	Spherical water	Spherical water
Phase functions	- - - - - - - - - From Mie calculations - - - - - - - - -	
Size range	.03 - 10 μm	.03 - 10 μm
Size distribution function	h < 3 KM, proportional to $r^{-2.5}$ h > 3 KM, proportional to $r^{-3.5}$	Proportional to $r^{-3.5}$
Density distribution function	See Ref 8, Fig. 2	See Ref 8, Fig. 1
	h < 3 KM, same as clear standard atmosphere (Ref 10), but normalized to produce 3 KM surface visibility	h < 4 KM, same as clear standard atmosphere (Ref 10)
	h > 3 KM, according to Elterman (Ref 13)	h > 4 KM, according to Elterman (Ref 13)

where $\tau_{ext}(Z = 50\ KM)$ is the optical depth of the total atmosphere, (albedo/π) is the background reflectance per unit solid angle and $\exp(-\tau_{ext}(Z)|\sec\theta|)$ is the transmittance from the surface to altitude Z. Then

$$N^*(\theta_0,\lambda,albedo,Z,\theta,\phi) = N(\theta_0,\lambda,albedo,Z,\theta,\phi) - {}_bN_0(\theta_0,\lambda,albedo,\theta)T(Z,\theta) \quad (62)$$

For a plane isotropic source emitting 1 photon/m^2 at an altitude of 50 KM, the scattered intensities and ${}_bN_0T$ were computed from the Monte Carlo data for plane parallel source as follows:

$$N_{ISO}(\lambda,albedo,Z,\theta) = \frac{1}{2}\int_{\theta_0=0}^{\pi/2} N(\theta_0,\lambda,albedo,Z,\theta,\phi)\sin\theta_0\, d\theta_0 \quad (63)$$

$${}_bN_0(\lambda,albedo,Z,\theta)T(Z,\theta)\Big]_{ISO} = \frac{1}{2}\int_{\theta_0=0}^{\pi/2} {}_bN_0(\lambda,albedo,Z,\theta)T(Z,\theta)\sin\theta_0\, d\theta_0 \quad (64)$$

then

$$N^*_{ISO}(\lambda,albedo,Z,\theta) = N_{ISO}(\lambda,albedo,Z,\theta) - {}_bN_0(\lambda,albedo,Z,\theta)T(Z,\theta)\Big]_{ISO} \quad (65)$$

Contrast transmission may be calculated from Eq (13). Tables of contrast transmission are listed in Ref 8, Vols I, II, and III.

A more recent model has also been developed by RRA for AFCRL using a spherical shell atmosphere and a "backward" Monte Carlo technique. The authors indicate that the improved model is required for twilight scattering studi sun is very low. The model is described in Refs 18 and 19.

AWS Atmospheric Model. The data summarized here for the Air Weather Service model is taken from "Computer Simulation of Optical Contrast Reduction Caused by Atmospheric Haze" (Ref 16), or from the modified computer program dated October 1971, obtained from the Air Force Avionics Laboratory.

Assumptions:

a. Horizontally stratified atmosphere (25 layers) and composed of atmospheric gases and haze particles

b. Number density of molecules is given by $N/N_0 = \exp(-Z/8.430\ KM)$

c. Top of atmosphere is 84.3 KM

d. Ozone absorption occurs above the top of the atmosphere

e. Absorption of visible light by other atmospheric molecules and haze particles is neglected

By neglecting absorption in the atmosphere the extinction coefficient at any altitude is

$$\beta_T(Z) = \beta_R(Z) + \beta_H(Z) \tag{66}$$

where T, R, and H refer to total, Rayleigh and haze scattering respectively, and the scattering coefficient is

$$\sigma_T(\beta,\lambda,Z) = \sigma_R(\beta,\lambda,Z) + \sigma_H(\beta,\lambda,Z) \tag{67}$$

where β is the scattering angle as discussed previously. For Rayleigh scattering

$$\sigma_R(\beta,\lambda,Z) = \frac{f(\beta)}{\lambda^4} e^{-Z/H_R} \tag{68}$$

where $f(\beta)$ is independent of wavelength and is proportional to $(1 + \cos^2 \beta)$, σ_R is scaled such that in the limit of a Rayleigh atmosphere the surface visibility is 336 KM. For haze

$$\sigma_H = \frac{[\beta_\lambda(Z)]_H p_\lambda(\beta)}{4\pi} \tag{69}$$

where $p_\lambda(\beta)$ is the scattering phase function such that

$$\int_{4\pi} \frac{p_\lambda(\beta)}{4\pi} d\Omega = 1$$

the same as the angular scattering phase function was discussed above in Chapter II, in Eqs (1) through (6).

Four atmospheres are specified although they may be changed as required in the program. The data for these atmospheres is presented in Table V.

The equations used in the development of the AWS model are given in Ref 16. The problem which is solved is the transfer equation stated earlier in Eq (6). We will describe here only the basis of the solution.

As noted in the list of assumptions, we have a one dimensional problem with the assumption of horizontally stratified atmosphere. Then Eq (6) applies. Also $\kappa(Z)$ reduces to $\beta(Z)$ with the assumption of no absorption in the atmosphere. We also have boundaries at the surface of the earth and at the top of the atmosphere at which we may apply boundary conditions to solve our problem. The spectral irradiance at the "top" of the atmosphere is well defined and may be used as an input. The absorption due to ozone is also obtainable, so this may be taken into account above the atmosphere. The spectral irradiance reaching the surface of the earth is composed of two portions: the direct solar spectral irradiance which has reached the earth without scattering and the diffuse spectral irradiance from the sky.

The diffuse irradiance may be thought of as coming from single scattering events (where the solar spectral radiance is scattered once before reaching the earth), and from multiple scattering events (which are made up of diffuse radiance which has been scattered).

The same ideas apply for any plane in the atmosphere but with spectral irradiances arriving from both above and below.

The problem is then solved in pieces. The direct solar irradiance reaching the earth is the solar irradiance after ozone absorption multiplied by the transmission from the top of the atmosphere to the altitude

TABLE V

Atmospheric Parameters for Air Weather Service Haze Model

Parameter	3 KM "Dirty"	10 KM "Typical"	15 KM "Suburban"	23 KM "Clear"
Layers	25	25	25	25
Rayleigh extinction coefficient	$\beta_R(Z,.45\ \mu m) = 2.64\times10^{-7}\ cm^{-1}\ \exp(-Z/8.430\ KM)$			
Ozone absorption coefficient	Source unspecified; uses integrated absorption coefficient as a function of λ above atmosphere			
All other absorption	Neglect			
Aerosol particles	Spherical water			
Size range and size distribution and phase functions	See D. Deirmendjian (Ref 20) for description of Haze models listed below			
	0 - 3 KM, Haze M 3 - 12 KM, Haze L	0 - 12 KM, Haze L	0 - 12 KM, Haze L	0 - 12 KM, Haze L
	12 KM - up, Haze H			
Aerosol density distribution	h > 4 KM, from Elterman (Ref 13)			
	0 - 1 KM, see Ref 16, Fig. 2 1 - 4 KM, same as "Typical"	0 - 4 KM, see Ref 16, Fig. 2	0 - 4 KM, see Ref 16, Fig. 2	0 - 4 KM $N/N_0=\exp(-Z/1.2\ KM)$

of interest and the cos θ_0. A diffuse surface is assumed at the earth so that the reflected radiance of $\frac{\rho(\lambda)}{\pi}$ times the irradiance reaching the earth from direct and diffuse irradiance is reflected into a small solid angle. This spectral radiance times the transmittance from the surface to the receiver is called the reflectance $N_0(Z,\theta,\phi)T(Z,\theta)$ and reaches the receiver at altitude Z. Also reaching the receiver are singly and multiply scattered radiances from the path from surface to the receiver, $N^*(Z,\theta,\phi)$.

The path radiance seen by the observer is made up of singly and multiply scattered radiances. The singly scattered radiances may be easily handled using Eq (6) since we know the spectral irradiance from the direct solar irradiance at any altitude along the path from the surface to the observer.

The singly scattered radiance reaching the earth which contributes to the image forming light may also be handled from Eq (6).

To determine the multiply scattered portions of the radiation reaching the surface of the earth and reaching the observer, one uses Eq (6) for an upward and downward stream of diffuse spectral irradiance. Thus two differential equations may be set up and solved simultaneously using the boundary conditions to yield the diffuse spectral irradiances moving upward and downward at any altitude. The procedure related above for determining the singly scattered components is then repeated for the multiply scattered components, using the diffuse irradiances.

The program computes three basic parameters: the path radiance $N^*(Z,\theta,\phi)$; the air-transmittance $T(Z,\theta)$ from the surface of the earth to the observer; and the inherent spectral radiance $N_0(Z_+,\theta,\phi)$ from a surface of unit reflectivity in the direction of the observer. These three parameters

may be used in Eq (13) by modifying the third to coincide with the true directional reflectance of the background. They may also be used to calculate the directional path reflectance $R^*(Z,\theta,\phi)$, since the downwelling irradiance is just equal to the spectral radiance from a unity reflectivity surface times π.

Measurements: Ground and Flight

Two methods exist to estimate by measurement the effects of atmospheres on contrast. The first and direct way is to measure the inherent contrast either spectral or non-spectral in a given direction and then the apparent contrast as a function of range along that path of sight. The ratio of apparent to inherent contrast gives the atmospheric contrast transmission. The second, an indirect way, is to measure the parameters to solve the derived Eqs (13) or (58). Both methods are feasible but involve different problems. For example, in the direct method, one must be able to measure the apparent contrast between reasonable distances and also be able to describe the weather and measure the visibility conditions so that these measurements may be related to other similar weather and terrain conditions. The problem with the measurement then is to maintain accuracy in the contrast measurement over a wide range, implying some type of zoom optical system to maintain the same field of view. Assuming that this could be done, an extremely large number of measurements would be required to describe all the possible approach angles and sun angles and sky conditions.

Contrast data measured photographically at 200 feet and 3000 feet is presented in Chapter VI of this report. A flight test program to measure apparent contrast as a function of range from the target under several weather conditions is reported in Ref 21. Two vidicons were used: the

current Maverick vidicon with peak response in the visible at .55 μm and a silicon vidicon with peak response in the near IR at .75 μm. Data was reduced from the video recordings of the individual TV lines. Data is presented as apparent contrast versus range and an exponential curve is fitted to the data. The inherent contrast and the extinction coefficient are the free parameters for the fitting process. The report should provide a useful reference in future attempts to reduce contrast from the video recordings.

The indirect approach is the one presently being followed by the Visibility Laboratory, Scripps Institute of Oceanography in their work for Air Force Cambridge Research Laboratories.

With the concept of the path function from Eq (20) and the path radiance from Eq (7), Duntley points out that one might experimentally determine the path radiance $N^*(Z,\theta,\phi)$ by summing up the products of the path function over an incremental path Δr along the path and the transmittance of the path from that incremental path to the sensor (Ref 7: Appendix A).

Then,

$$N_r^*(Z,\theta,\phi) = \sum_{i=1}^{m} N_*(Z_i,\theta,\phi)T_{r_i}(Z,\theta)\Delta r \tag{70}$$

where $N_*(Z,\theta,\phi)$ is the path function and $T_{r_i}(Z,\theta)$ is the beam transmittance along path r_i, the distance from incremental path Δr to the sensor at Z. $N_*(Z,\theta,\phi)$ is given by

$$N_*(Z,\theta,\phi) = N_q(Z_i,\theta,\phi)\beta(Z_i) \tag{71}$$

where $N_q(Z_i,\theta,\phi)$ is the equilibrium radiance for altitude Z_i and $\beta(Z_i)$ is the total scattering coefficient.

N_q is given by

$$N_q(Z,\theta,\phi) = \frac{1}{4\pi}\int_{\Omega'} N(Z_1,\theta',\phi')p(Z,\hat{\Omega}',\hat{\Omega})d\Omega' \qquad (72)$$

where $N(Z,\theta',\phi')$ is the apparent radiance of the sky or ground for direction θ',ϕ' and $p(Z,\hat{\Omega},\hat{\Omega}')$ is the angular scattering phase function for direction $\hat{\Omega}$ for radiation entering in direction $\hat{\Omega}'$ at altitude Z_1.

All the quantities here are spectrally dependent. To determine the path radiance then for a path of sight, one must know, either experimentally or analytically, the radiance of the sky and ground in all directions from each incremental path along the path of sight. One must also know or measure the proportional directional scattering coefficient, and the transmission for each incremental path along the path of sight.

The measurement techniques used to determine the parameters to solve Eqs (70), (71) and (72) are described in Ref 7. The measurement aircraft flies straight and level profiles at several altitudes and then makes vertical ascents and descents. During this time, radiometers with several filters are scanning the sky and ground to measure the apparent radiance $N(Z,\theta',\phi')$ of Eq (72).

Simultaneously, a nephelometer, mounted on the end of the wing, is measuring beam transmittance over an incremental path for Eq (70). If feasible a ground station is positioned along the track of flight to measure the same parameters on the ground. The data is then interpolated or extrapolated to produce data at required intermediate intervals. The scattering functions used in the cases reported here for Eq (72) are measured data from Barteneva (Ref 7:Appendix E). The path radiance may then be calculated from Eqs (70), (71) and (72). The spectral irradiance at the surface may be calculated from

$$H(Z_t,d) = \int_{2\pi} N(0,\theta',\phi')\cos\theta' \, d\Omega' \tag{73}$$

The inherent directional background reflectance may then be determined from

$${}_bR_0(Z_t,\theta,\phi) = \frac{{}_bN_0(Z_t,\theta,\phi)}{H(Z_t,d)/\pi} \tag{74}$$

Air-transmittance is obtained by summing over the incremental paths. Then contrast transmission may be determined from either Eq (13) or (58).

We note the significant advantage that the indirect method is independent of any particular target.

III. Approach Chosen

Several approaches were discussed in the previous chapter. An approach is now chosen for solving the problem. It is clear that the measurement approach is highly desirable but very time and resource consuming and application to other conditions very difficult. Thus the model approach is chosen here. The model chosen is that in which the directional path reflectance R* is the key parameter rather than the sky-ground ratio. The latter still provides a useful analytic tool provided the more realistic optical standard atmosphere and sky-ground ratios presented in Chapter II are used. The advantage of the directional path reflectance concept is that it allows decoupling of the atmosphere from the directional background reflectance. The sky-ground ratio explicitly does not. The directional path reflectance R* provides a single parameter to describe the effect of the atmosphere, sun, scene albedo combination. The sky-ground ratio concept could be adjusted to consider the individual parts, the equilibrium radiance and the background reflected radiance, in which the same decoupling occurs, but then the formulation is more complex since the transmittance must still be considered.

So with the calculation of the directional path reflectance either from airborne measured data as described by Duntley et al. (Ref 7) or from a numerical model like the RRA Monte Carlo or AWS models, one can use this single parameter to investigate the ease or difficulty of contrast transmission for any azimuth or dive angle. One can construct surfaces of constant directional path reflectance in space and from their shape determine the best and worst directions for contrast transmission

for that atmosphere, solar zenith, and surface albedo. It must be stressed that the contrast transmission is still not uniquely determined since the directional background reflectance must be used. The decoupling mentioned above aids greatly in simplifying the problem of determining the atmospheric effects. Some of these effects can be seen from Figs. 13 through 18. Figure 13 plots the directional path reflectance versus azimuth from the sun for a clear atmosphere (23 KM) but with two solar zenith angles. A wavelength of .55 μm and an albedo of .06 have been used. Note the stronger effect of azimuth from the sun as the solar zenith angle increases. The data has been calculated from the AWS program. Note also the increase in directional path reflectance as the zenith angle of the sun increases, implying better seeing conditions in general for the higher sun. In addition, the effect of azimuth appears strong for only a limited azimuth range, while there is a rather broad area in which the effect is not too great. Now going to Fig. 14, the contours of constant directional path reflectance have been plotted versus altitude and horizontal range for a sun angle of 42° and an albedo of .06. Figure 15 shows the same type of plot except the solar zenith has been increased to 78°. Both plots are presented for an azimuth of 90° from the sun. Note in general the increased slant range as the dive angle increases. This improvement is due to an increase in transmission with dive angle and a decrease in path radiance. Again the data has been generated from the AWS program. The contours differ as the azimuth is changed as noted from Fig. 13.

Importance of Directional Background Reflectance

Once the directional path reflectance is known, one must have the angular dependence of the directional background reflectance to determine the contrast transmission. Many times, since this is not known, a diffuse

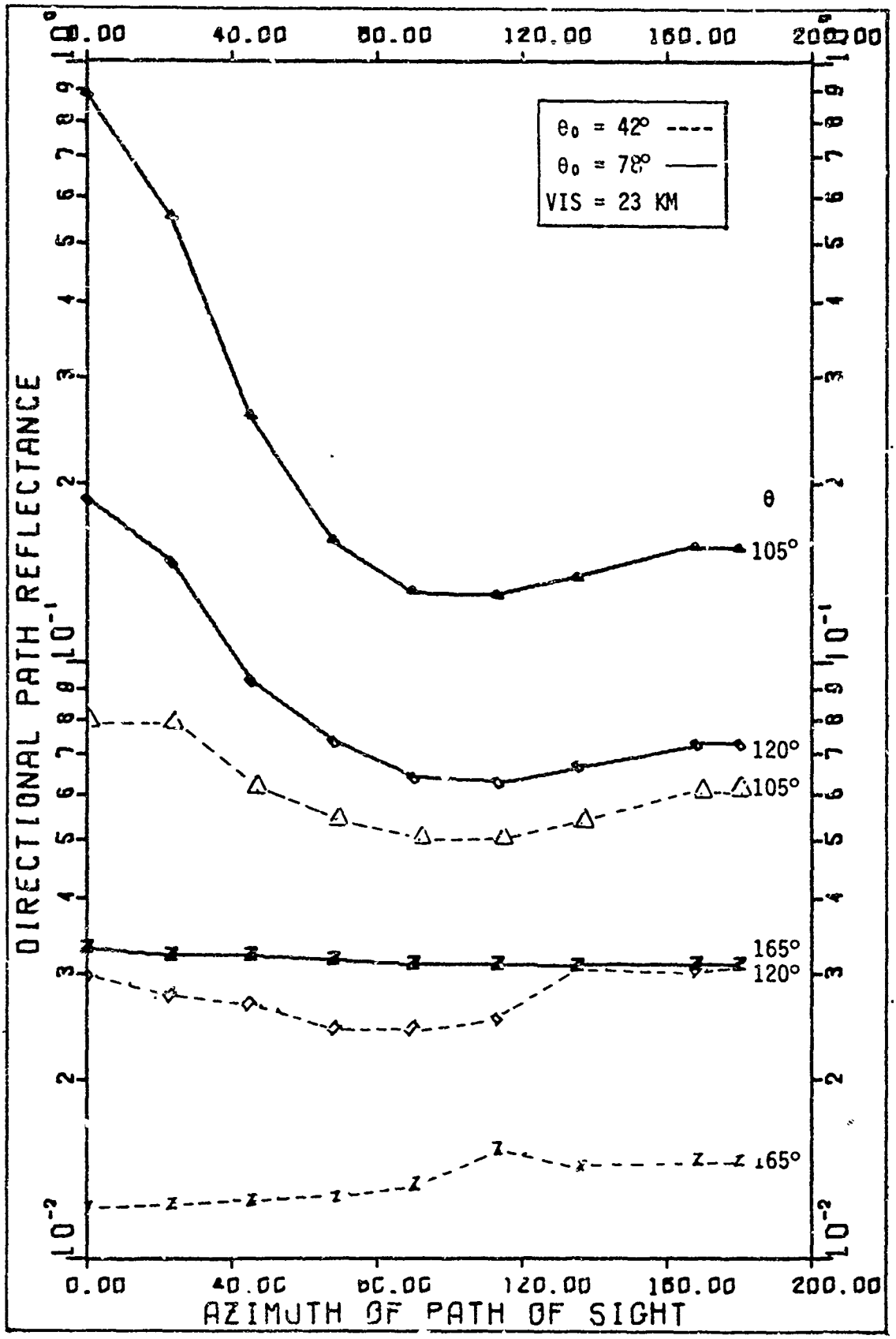

Fig. 13. Directional Path Reflectance Versus Azimuth for Two Solar Zenith Angles. Albedo is .06, λ = .55 μm, Altitude is 2 KM. Data from AWS Model.

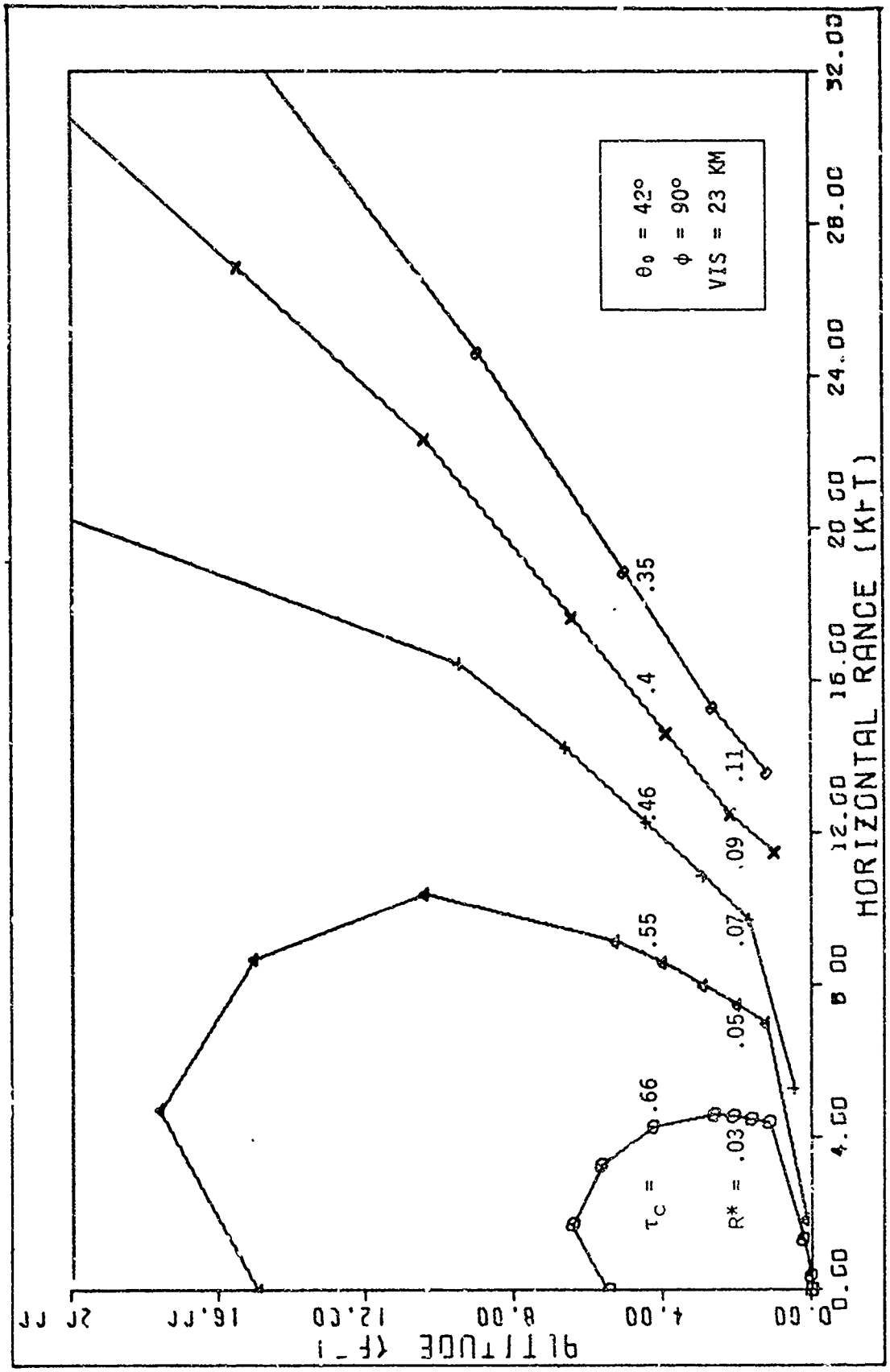

Fig. 14. Contours of Constant Directional Path Reflectance R* for a Solar Zenith Angle of 42°, and an Azimuth of 90°. Albedo is .06 and λ = .55 μm. Values of Contrast Transmission are Shown Assuming $_bR_0$ = Albedo. Data from AWS Model.

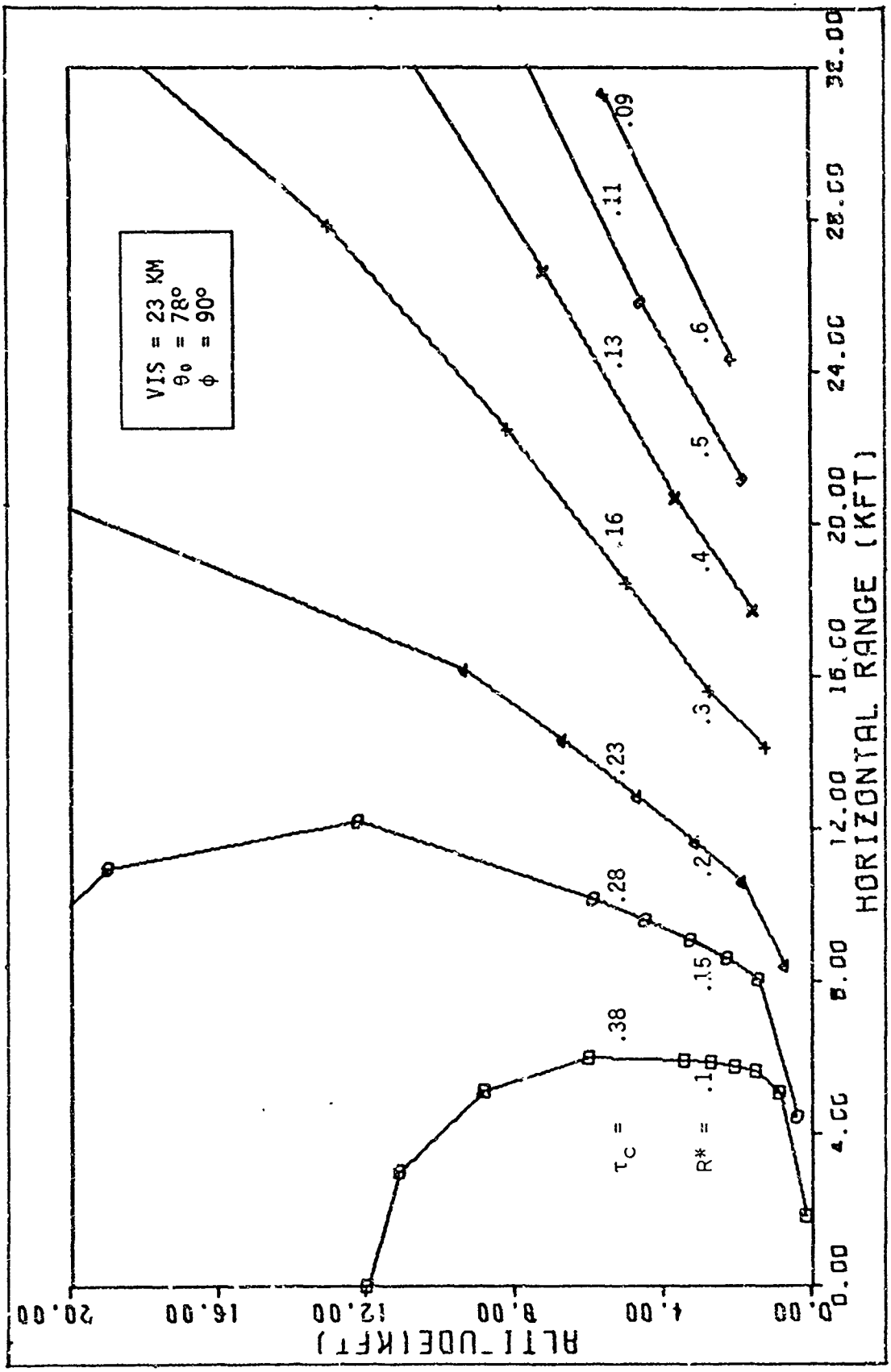

Fig. 15. Contours of Constant Directional Path Reflectance R* for a Solar Zenith Angle of 78° and an Azimuth of 90°. Albedo is .06 and λ is .55 μm. Values of Contrast Transmission are Shown Assuming $_bR_0$ = Albedo. Data from AWS Model.

surface will be assumed, in which case the directional background reflectance is just the scene albedo used to calculate the directional path reflectance. In the latter case, the three figures (13, 14, and 15) describe exactly the shapes of the contours of constant ntrast transmission. In that case Eq (58) or Fig. 12 may be used to convert the contours of constant directional path reflectance to ones of constant contrast transmission. Similarly, the igures may be rescaled in terms of contrast transmission. This is shown in Figs. 14 and 15. But if the directional background reflectance is not a constant, then the shapes of the curves above are changed. From the discussion in Chapter II, we saw the strong effect of directional background reflectance. Here we reference data collected by Duntley and others for AFCRL during flight tests which shows the directional background reflectance variation with look angle and azimuth from the sun for a particular type of terrain (Ref 22:795). The data was taken using a photopic filter so that it is an integrated reflectance. It must be first noted that this data is based on an average reflected energy from a large area of not necessarily uniform terrain and that the value which should be used in Eq (58) is the directional reflectance of the background in the immediate vicinity of the target. But the variation shown should be representative of terrain of that type. The data is presented in Figs. 16 and 17. It was taken with solar zenith angle of 42° and the albedo was .06. If this data is then used instead of assuming a constant value of directic background reflectance, it can be applied through Eq (58) or Fig. 12 to generate the contours of constant contrast transmission shown in Fig. 18. Here we assume that the R* data is representative of the photopic or visible region. Note the pronounced change in shape between Fig. 14

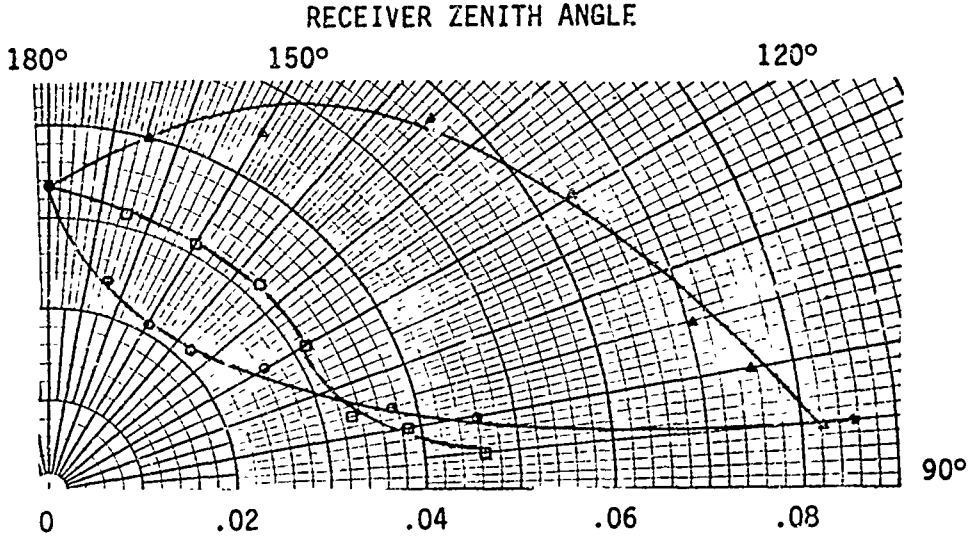

Fig. 16. Measured $_bR_0$ Data as a Function of Receiver Zenith Angle for Three Azimuths. Data Taken Over Small Pine Trees, Uniformly Spaced. (Ref 22:795). Albedo = .06.

ϕ = 0° ○

ϕ = 90° □

ϕ = 180° △

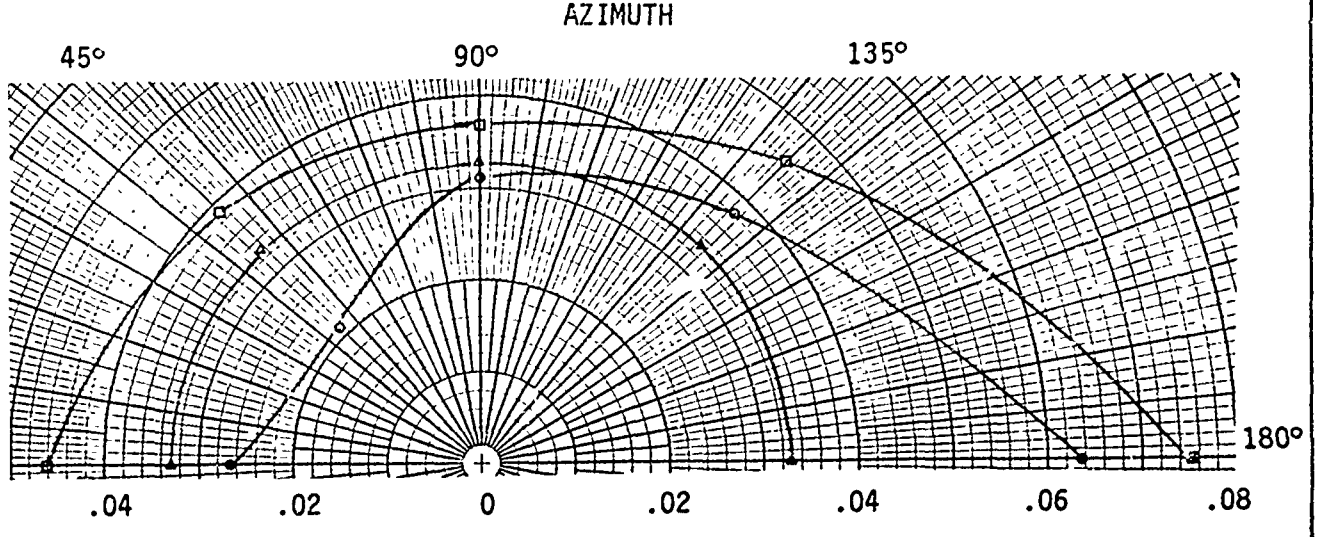

Fig. 17. Measured $_bR_0$ Data as a Function of Azimuth for Three Receiver Zenith Angles. Source Same as Fig. 16.

θ = 100° □

θ = 120° ●

θ = 180° △

and Fig. 18. Other data measured by Duntley indicates the same type of strong dependence with look angle and azimuth (see Table VI). The importance of knowing the directional background reflectance is clearly illustrated, particularly for low dive angles. Several sources of this data are available. The sources listed here are primarily those done by Duntley and others for AFCRL. The University of Michigan, Target Signature Analysis Center has compiled a data bank for NASA which contains directional background reflectance data for many background materials. In Table VI the target or background material, the sun angles and the sky conditions are listed along with the reference where the data appears.

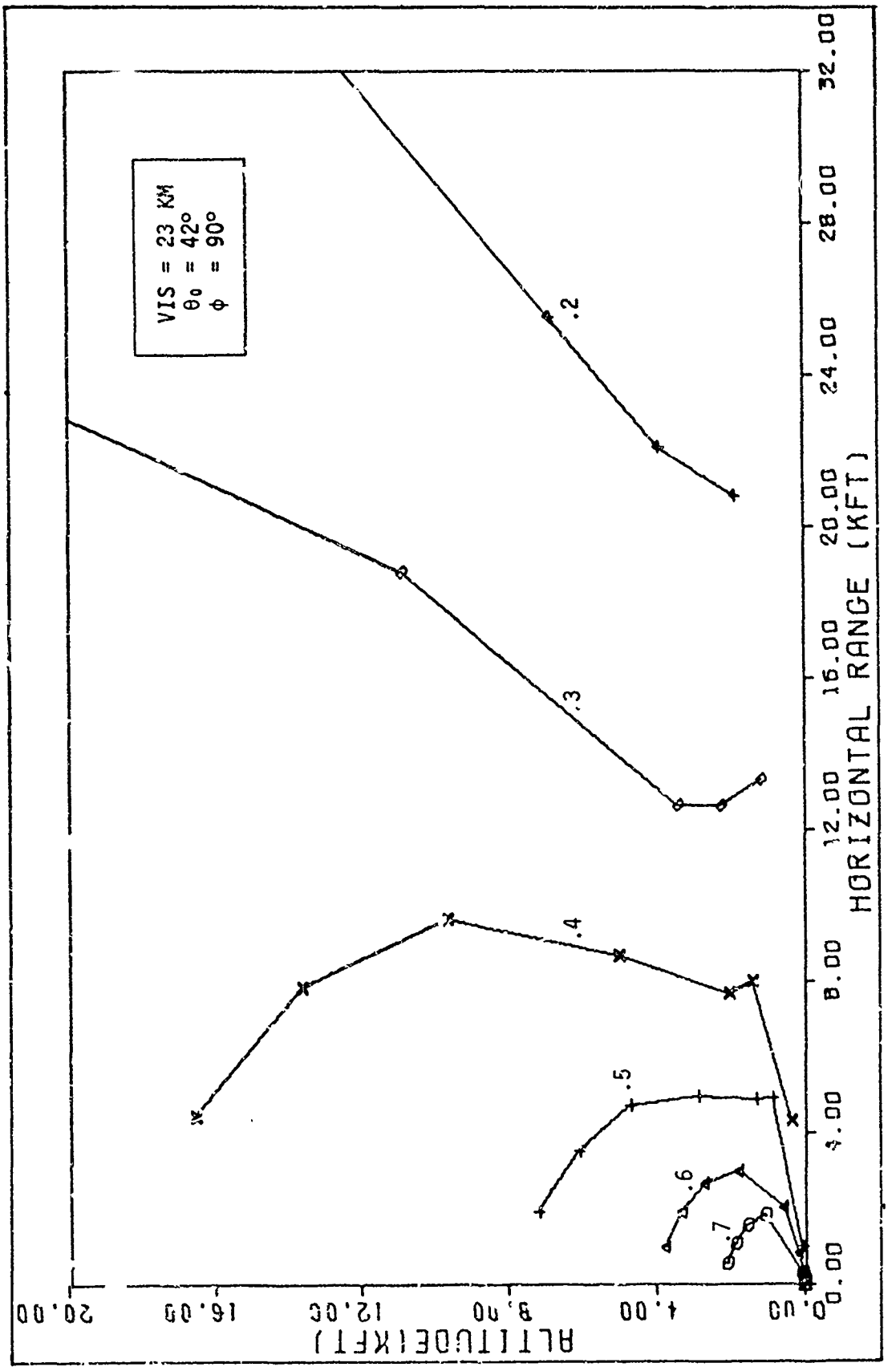

Fig. 18. Contours of Constant Contrast Transmission for a Solar Zenith Angle of 42° and an Azimuth of 90°. Albedo is .06, and λ is .55 μm. R^* Data is from AWS Model, $_bR_o$ Data is Measured Background Reflectance from Fig. 16.

TABLE VI

Some References for Directional Reflectances of Backgrounds and Target Materials

Target or Background	Solar Zeniths	Spectral Region	Sky Condition	Reference
Pine trees, grass, soil, concrete, etc.	40° - 50°	Photopic	Clear	(Ref 22:559)
Aluminum, aluminum paint, glossy white paint	50° - 60°	Photopic	Clear	(Ref 22:561)
Snow, crops, soil, water	51° - 52°	Photopic	Overcast	(Ref 24:920,21)
Black and g ip paints	51° - 52°	Photopic	Overcast	(Ref 24:922)
Snows, water, dirt road	74° - 78°	Photopic	Clear	(Ref 23:804)
Black and gray ship paints	71° - 76°	Photopic	Clear	(Ref 23:808)
Farmland and trees (Germany)	35° - 55°	Blue, red, photopic, and S-20	Varied--clear to overcast	Project Haven View (Ref 9)
Spain, Morocco, Mediterranean	Unknown	Blue, red, photopic, and S-20	Unknown	Project Haven View (Ref 9)
Crops, etc.	Varied	Varied	Varied	NASA Data Bank (Ref 25)

IV. Comparison of Calculations Between Models and Comparison to Flight Data

In this chapter, a comparison will be made between the Air Weather Service Model and the Monte Carlo model of Radiation Research Associates. Also after it has been shown that the AWS model predicts results with reasonable agreement to the Monte Carlo model, comparison will be made to flight data collected during Project Haven View.

The more direct calculational approaches like the AWS model and the University of Michigan model possess superiority over the Monte Carlo method in making rapid calculations on the computer. A rough estimate has indicated that the AWS program runs 360 cases in the time the Monte Carlo calculations program runs 1 case. Here a case is defined as a particular visibility, solar zenith, albedo, wavelength, altitude, azimuth and receiver zenith angle position. This can be very important if one is attempting to describe a complex situation and trying to optimize a situation for best seeing conditions. One could easily include the last program as a subroutine in an overall program, while the Monte Carlo calculation method would almost be out of the question.

The question then arises as to how the results of the faster AWS program can compare to the results predicted by the more exact, and by its nature more time consuming, Monte Carlo method. The RRA Monte Carlo data for the calculations are from Contrast Transmission Data for a Clear and Hazy Model Atmosphere (Ref 8), already described. The AWS data has been run from the computer program as described in "Computer Simulation of Optical Contrast Reduction Caused by Atmospheric Aerosol," (Ref 16) previously cited. Since the computer program was not available for the Monte Carlo

calculations, and the AWS program was, the AWS data was generated to match as closely as possible the conditions already generated by the Monte Carlo method and then the comparison was made. The comparison could not be exact without some extensive although not difficult modifications to the AWS program. These were not done. Table VII indicates the value of each parameter used in the Monte Carlo calculations and the comparable parameter used in the AWS program.

As noted from Table VII the major differences occur in the altitudes and azimuths used for the calculations although some other differences exist in the scattering phase functions as may be detected from the discussion in Chapter II. The Monte Carlo method because of its statistical nature requires intervals over which the photons are collected, while the AWS method allows for calculations at discrete points. Also, the AWS model requires inputs in whole KFT so the altitude match was not exact. The largest error in altitude match is for the low altitude case in which the AWS data point is 20% higher in altitude. Averaging over azimuth can also have a strong effect. As can be seen from Fig. 13, already discussed, the directional path reflectance and thus the contrast transmission can vary sharply in the region between an azimuth of 0° and about 45° and also near 180° depending on solar altitude. Thus averaging over the interval 0°- 45° and 135° - 180° and calling these the mid-value of angle for comparison may lead to error.

In comparing the two models, the following formula was used to determine percentage difference:

$$\% \text{ difference} = \frac{\text{Monte Carlo value} - \text{AWS value}}{\text{Monte Carlo value}} \times 100\% \qquad (75)$$

This holds for comparison of air-transmittance, contrast transmission or

TABLE VII

Parameters Used for Monte Carlo - AWS Comparison

Parameter	Monte Carlo	Air Weather Service
Visibility	3 KM 25 KM	3 KM 25 KM Aerosol extinction modified to be similar to Monte Carlo from Ref 8 for both visibilities
Wavelength	.55 μm	.55 μm
Albedo	.1 .9	.1 .9
Solar zenith	0° 30° 70°(25 KM Vis) 75°(3 KM Vis)	0° 30° 70°(25 KM Vis) 75°(3 KM Vis)
Azimuth	22.5°(0-45°) 67.5°(45-90°) 112.5°(90-135°) 157.5°(135-180°)	23° 68° 113° 158°
Altitude	.5 KM 2.0 KM 4.0 KM 6.0 KM 10.0 KM	2 KFT(.61 KM) 7 KFT(2.13 KM) 13 KFT(3.96 KM) 20 KFT(6.10 KM) 33 KFT(10.06 KM)
Receiver angles	170.933° 164.267° 157.667° 148.217° 138.583° 130.550° 123.667° 116.750° 110.383° 104.483° All receiver angles are actually the center of a small interval in the Monte Carlo calculation; see Ref 8 for exact interval	171° 164° 158° 148° 138° 130° 123° 116° 110° 104°

computed sky-ground ratios. Thus a negative percentage implies that the AWS model calculates too high, and a positive percentage implies that the AWS calculates too low (here we make the assumption that the Monte Carlo method is more accurate).

25 KM Case

Let us first compare the air-transmittance calculation. Here the aerosol profiles used are very similar as seen from the previous discussions. Both are drawn from the same source, Elterman (Refs 10 and 13). The AWS data was adjusted to produce a surface visibility of 25 KM used on the RRA model.

Comparison of the contrast transmission data is illustrated in Figs. 19 through 28. Figure 19 shows the sun at 0° solar zenith (directly overhead). Contrast transmissions are plotted for both models as a function of altitude for three receiver zenith angles. The RRA data averaged over azimuth is plotted since there is large statistical variation with azimuth which should not be present. The results for the two steeper angles show that the AWS model is more optimistic than the RRA model and the percentage difference increases with altitude. At the shallow look angle, the agreement is good although the AWS data tends to be more optimistic. For an albedo of .9, all other conditions being the same, the data is plotted in Fig. 20. For all receiver angles, the AWS model is more optimistic; again the difference increasing with altitude. For a relatively high sun, solar zenith angle of 30° and an albedo of .1, contrast transmission for the two models is plotted for an azimuth of 113° in Fig. 21. Here the agreement is much better for the two shallow look angles but poor for the steep angle. This large difference appears to be due to the statistical variation in the Monte Carlo method rather than physical reasons since comparison

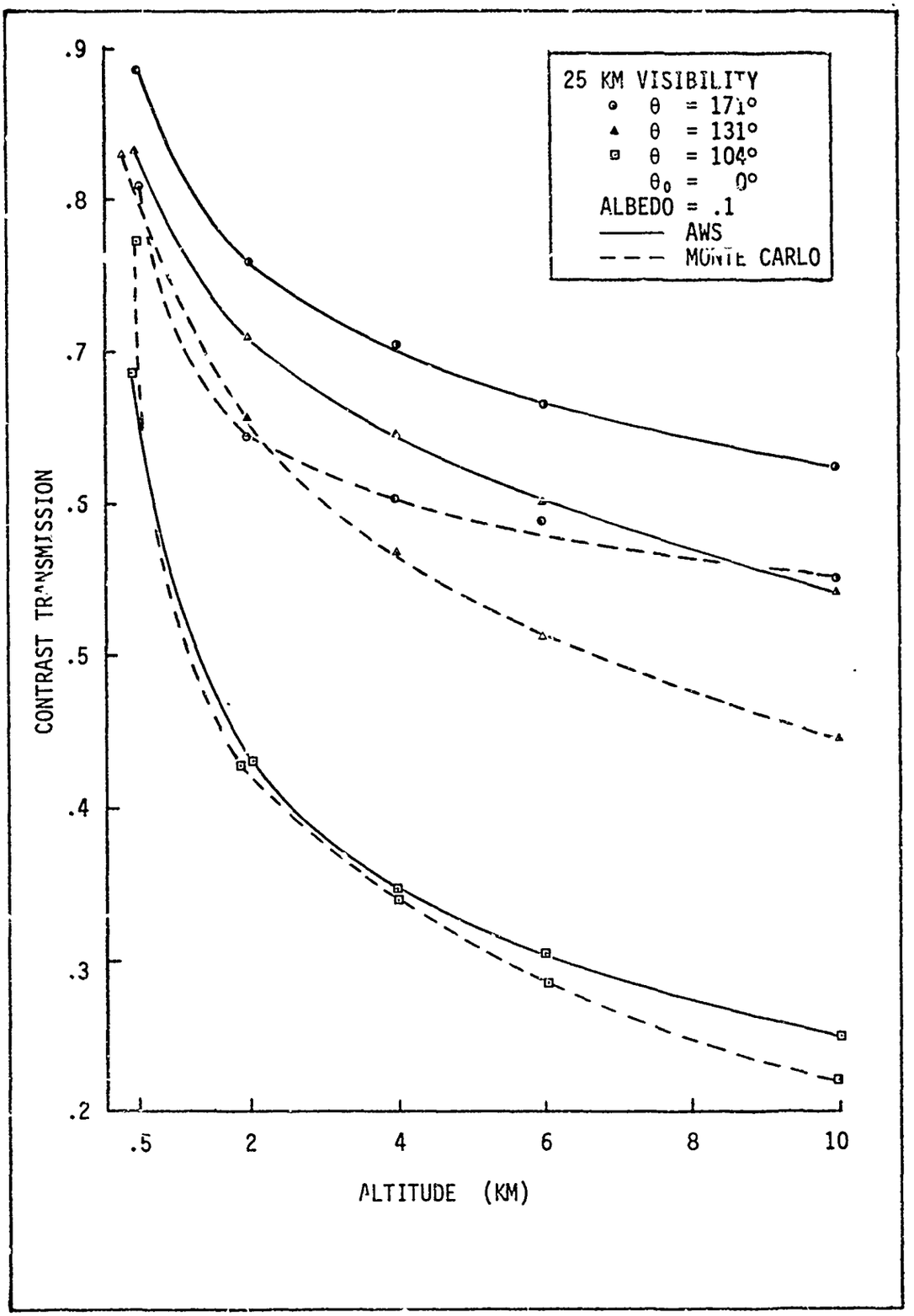

Fig. 19. Comparison of Calculation of Contrast Transmission by the AWS and RRA Monte Carlo Methods. The Wavelength is .55 μm, Solar Zenith Angle is 0°, Albedo is .1. The Surface Visibility is 25 KM.

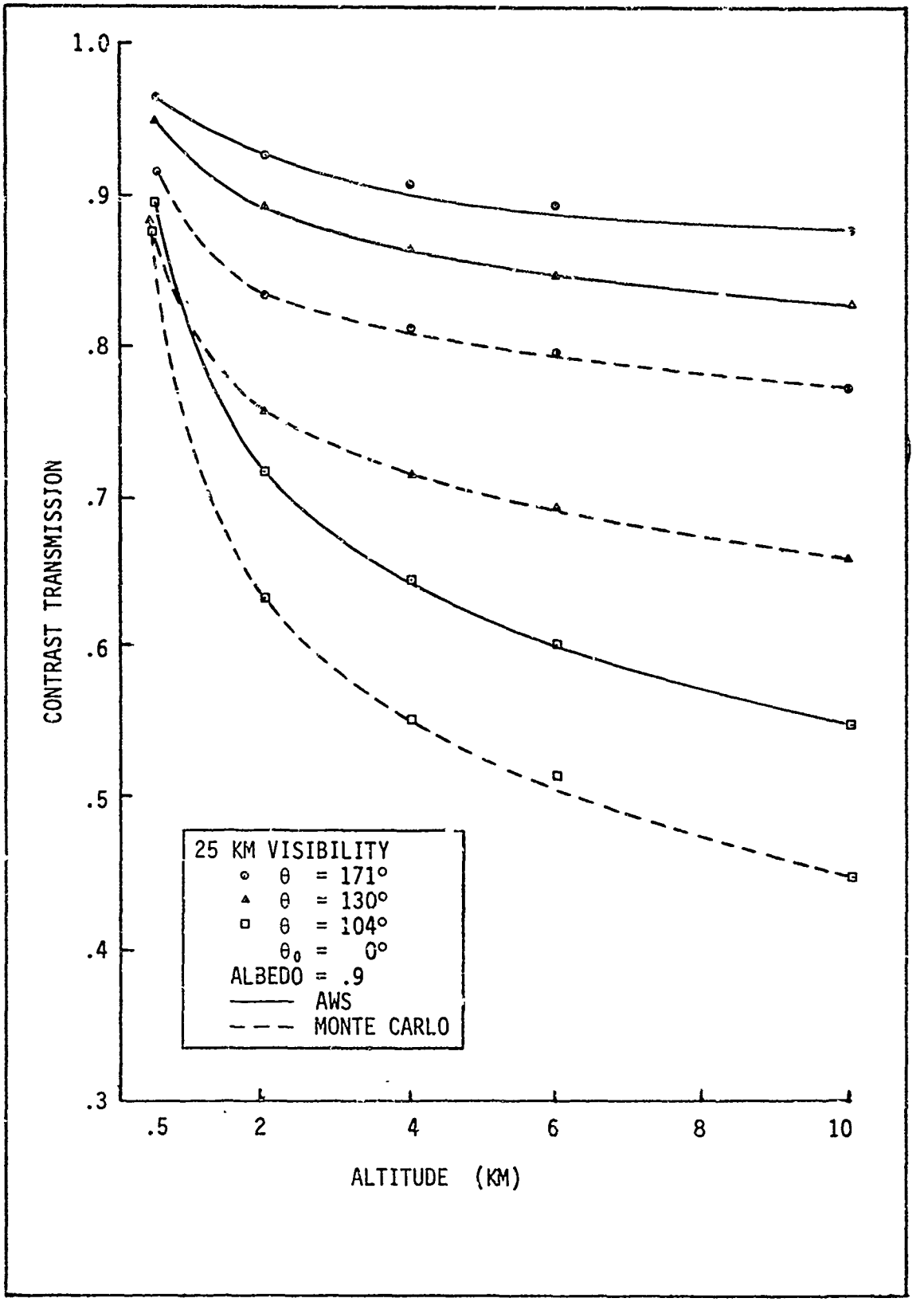

Fig. 20. Comparison of Calculation of Contrast Transmission by the AWS and RRA Monte Carlo Methods. The Wavelength is .55 μm, Solar Zenith Angle is 0°, Albedo is .9. The Surface Visibility is 25 KM.

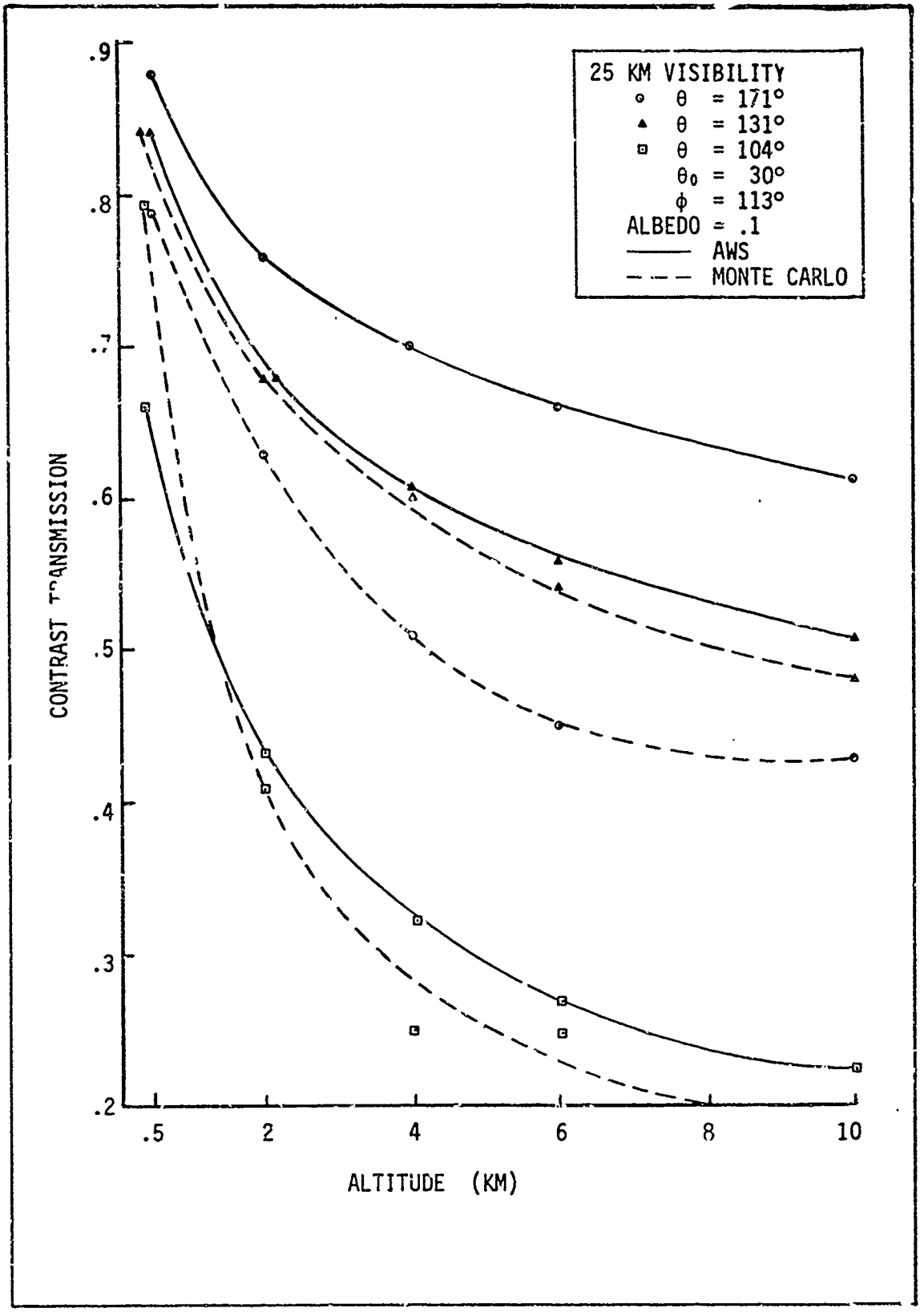

Fig. 21. Comparison of Calculation of Contrast Transmission by the AWS and RRA Monte Carlo Methods. The Wavelength is .55 μm, Solar Zenith Angle is 30°, Albedo is .1. The Surface Visibility is 25 KM.

for look angles of 164° and 158° shows a maximum of 11% error under these same conditions. The general trend continues to show an increase in difference with altitude with AWS predicting slightly higher values. In Fig. 22 the effect of azimuth is examined. Here for an altitude of 2 KM and for two look angles, contrast transmission is plotted against azimuth for a solar zenith of 30° and an albedo of .1. The Monte Carlo data is presented in bar graph fashion due to the averaging over a 45° azimuth in their presentation. The agreement in shape is reasonable. The 12% difference for the look angle of 131° and azimuth of 23° appears to be accounted for by the statistical nature of the Monte Carlo program, since this configuration is near the minimum of the scattering lobe for primary scattering, and path radiance should be a minimum assuming single scattering. Figure 23 presents the same conditions as in Fig. 21 but for an albedo of .9. Here the AWS model is again optimistic, and in comparison to the .1 albedo the difference between the two models is greater for the higher albedo. This is probably due to the increased upwelling radiation making multiple scattering more likely. The Monte Carlo method should handle multiple scattering more accurately than the AWS model. The Monte Carlo data for the look angle of 171° seems unrealistically low, particularly since it is well below the 131° data. Data at 164° and 158° show a maximum of 10% difference from the AWS data. Figure 24 presents similar conditions to Fig. 22 but with an albedo of .9. The AWS data is still optimistic, more so than for the albedo of .1 and probably due to increased multiple scattering mentioned above. The insensitivity of the AWS data to azimuth compared to the Monte Carlo data may be also due to the Monte Carlo superiority in accounting for multiple scattering events. Figure 25 shows the case of solar zenith angle 70° and albe .1. The agreement for all angles is reasonably good with

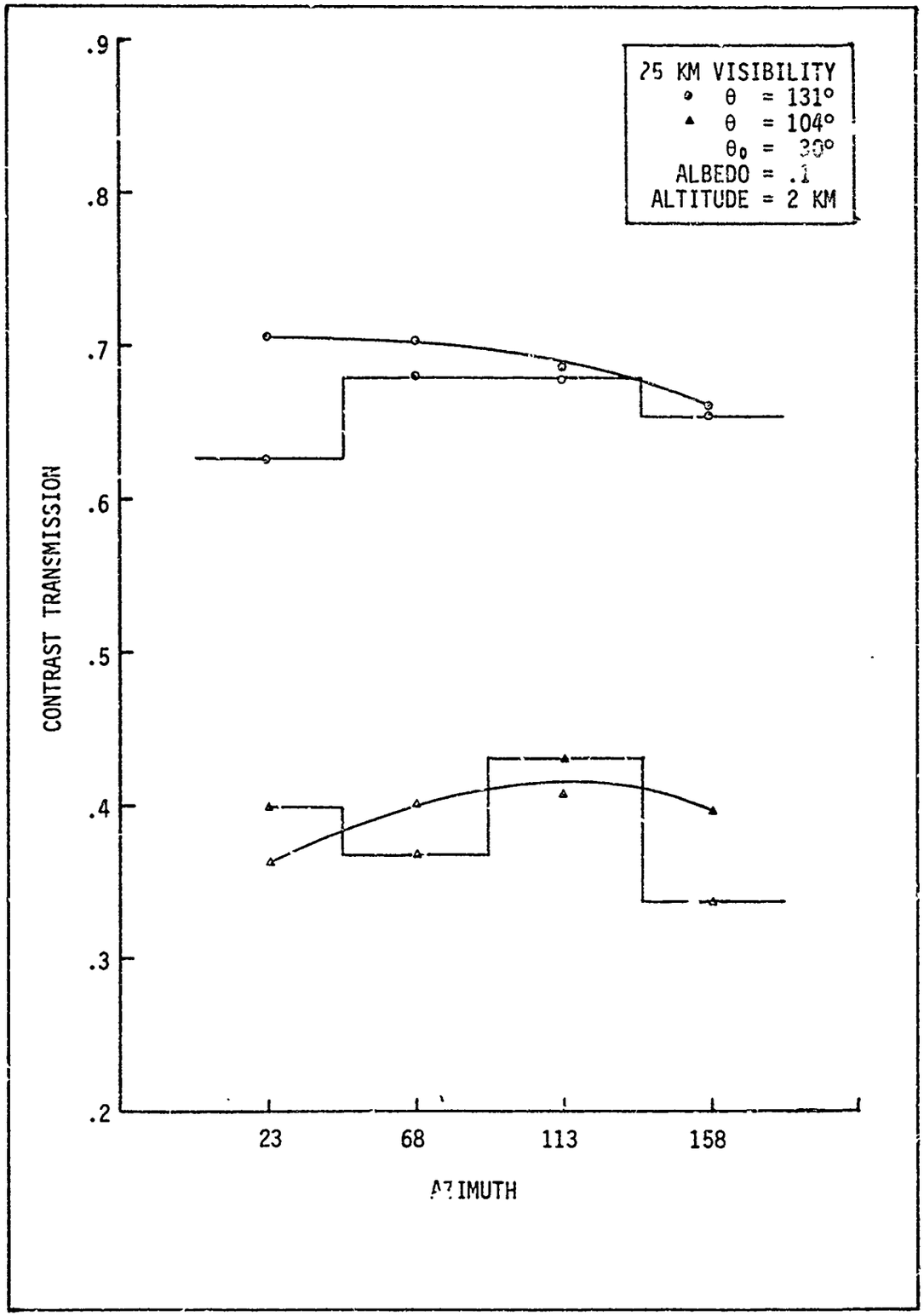

Fig. 22. Comparison of Calculation of Contrast Transmission by the AWS and RRA Monte Carlo Methods. The Wavelength is .55 μm, Solar Zenith Angle is 30°, Albedo is .1. The Surface Visibility is 25 KM.

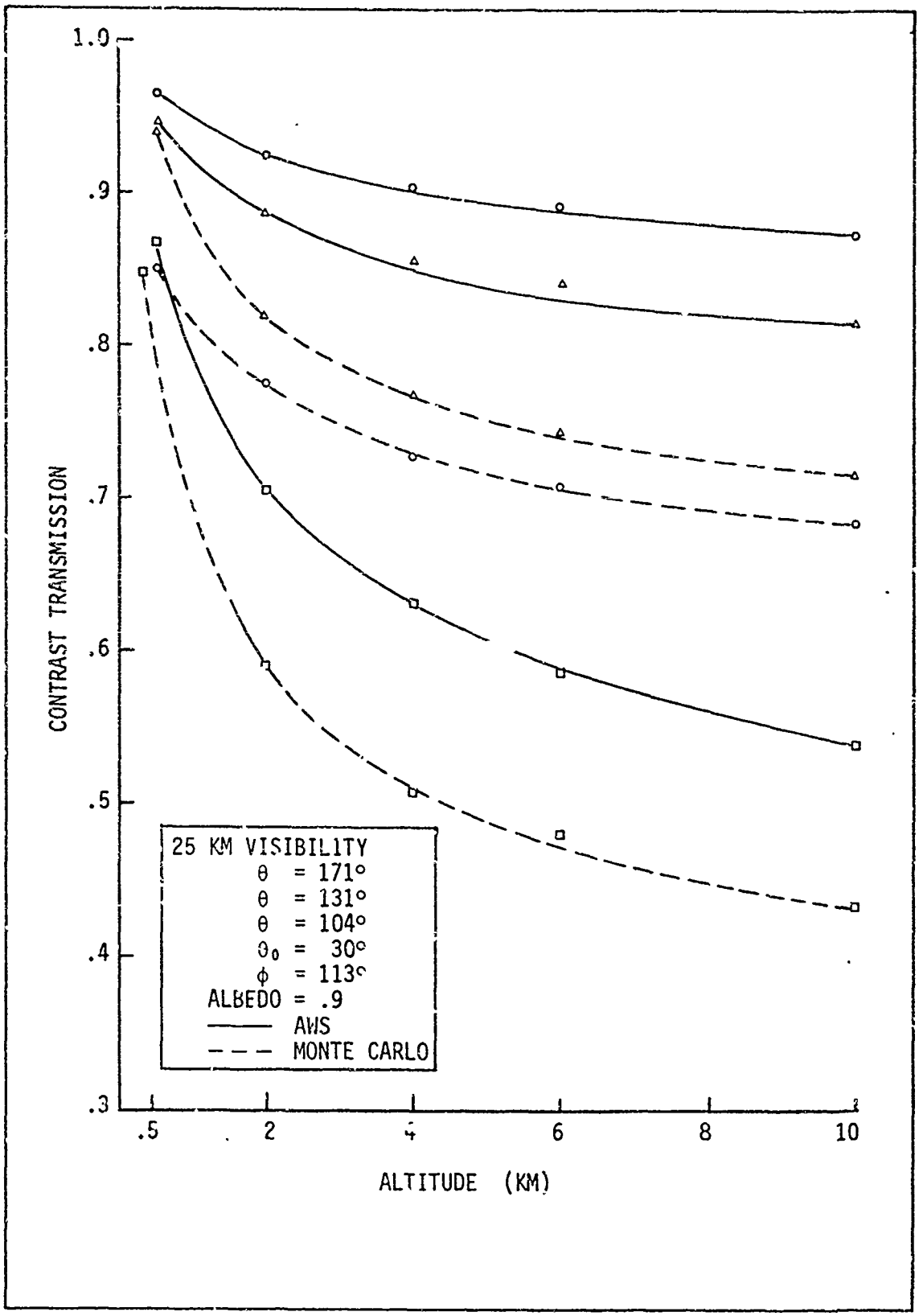

Fig. 23. Comparison of Calculation of Contrast Transmission by the AWS and RRA Monte Carlo Methods. The Wavelength is .55 μm, Solar Zenith Angle is 30°, Albedo is .9. The Surface Visibility is 25 KM.

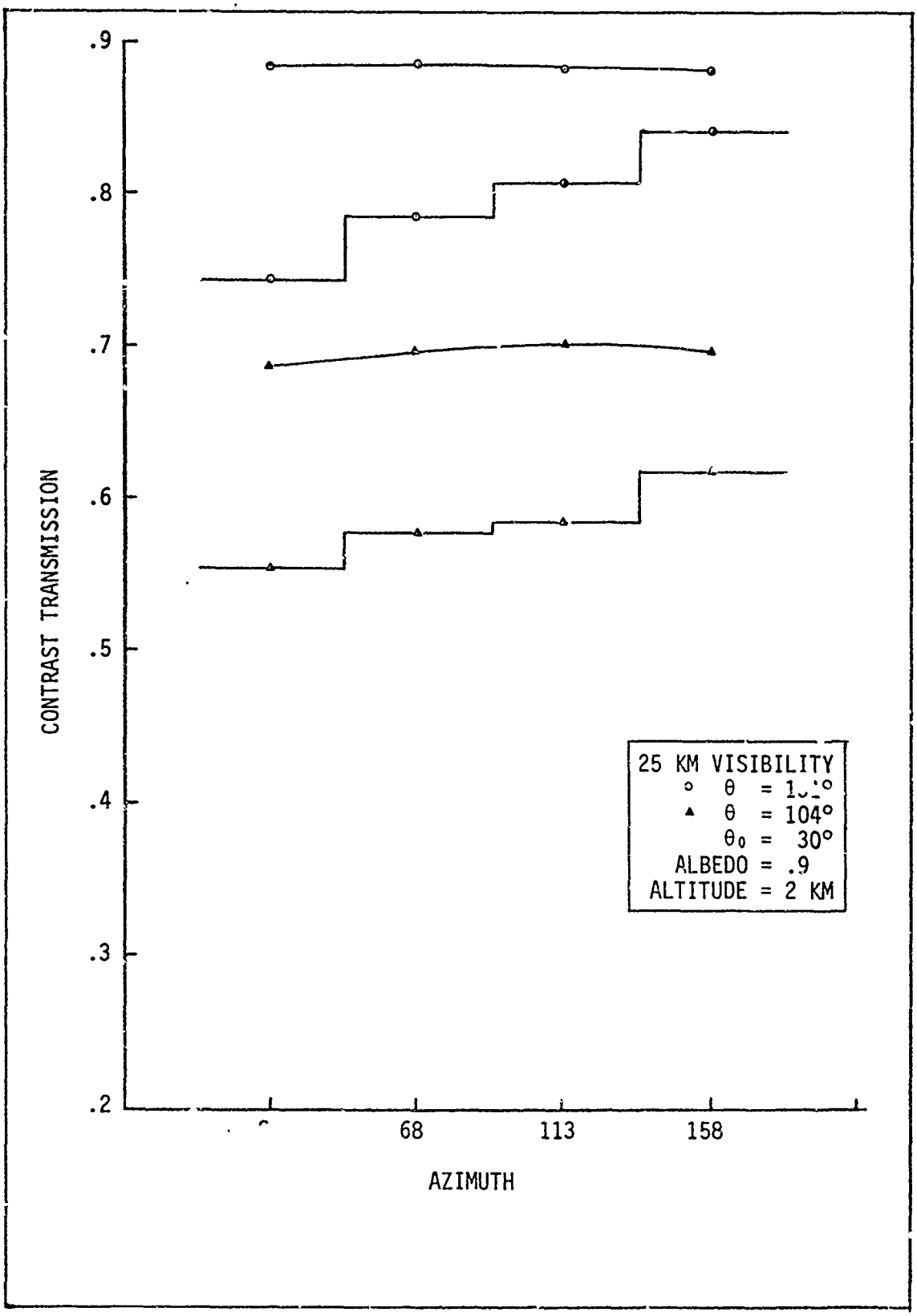

Fig. 24. Comparison of Calculation of Contrast Transmission by the AWS and RRA Monte Carlo Methods. The Wavelength is .55 μm, Solar Zenith Angle is 30°, Albedo is .9. The Surface Visibility is 25 KM.

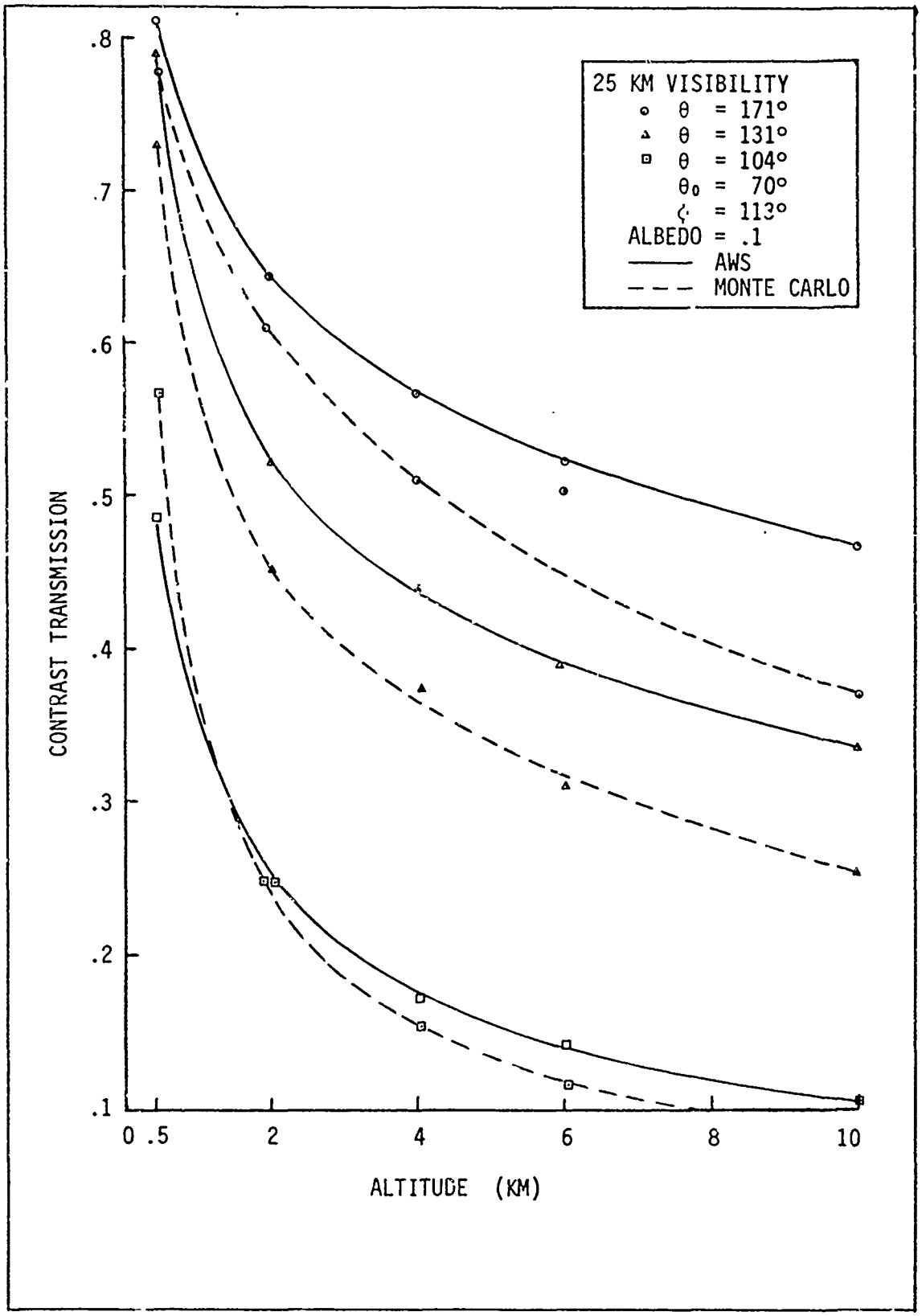

Fig. 25. Comparison of Calculation of Contrast Transmission by the AWS and RRA Monte Carlo Methods. The Wavelength is .55 μm, Solar Zenith Angle is 70°,Albedo is .1. The Surface Visibility is 25 KM.

the AWS model again predicting more optimistically as the altitude increases. Figure 26 shows the variation with azimuth. The agreement here is also quite good, although the Monte Carlo point for look angle of 131° is probably too high. Figures 27 and 28 present the same information for an albedo of .9. Previous trends are repeated with AWS more optimistic and increasing slightly with altitude. The significant increase in percentage difference is not as notable here as it was in the comparison of albedo for the solar zenith of 30°.

One can then conclude that the predictions of contrast transmission by the AWS model are comparable to those of the more time consuming and statistically variable Monte Carlo method for the clear visibility case compared here. This includes angles down to solar zeniths of 70° and look angles down to 104°. The AWS model tends to be more optimistic than the Monte Carlo method and the percentage difference increases with altitude. An increase in percentage difference with albedo was also noted for the high sun angles, but not for the low angles.

3 KM case

Due to the difference in aerosol profiles used by the RRA Monte Carlo method and the AWS model, the AWS model aerosol extinction profile was changed so that it reflected exactly the values used in the RRA model, up to and including 3 KM altitude. As noted previously, both models use the same data above that altitude.

Similar sun geometries and albedos are compared for the 3 KM case. The results are shown in Figs. 29 through 36.

Figures 29 and 30 show the case for solar zenith angle of 0° and albedos of .1 and .9 respectively for three receiver look angles. Note the good agreement for the low albedo but the large difference for the high

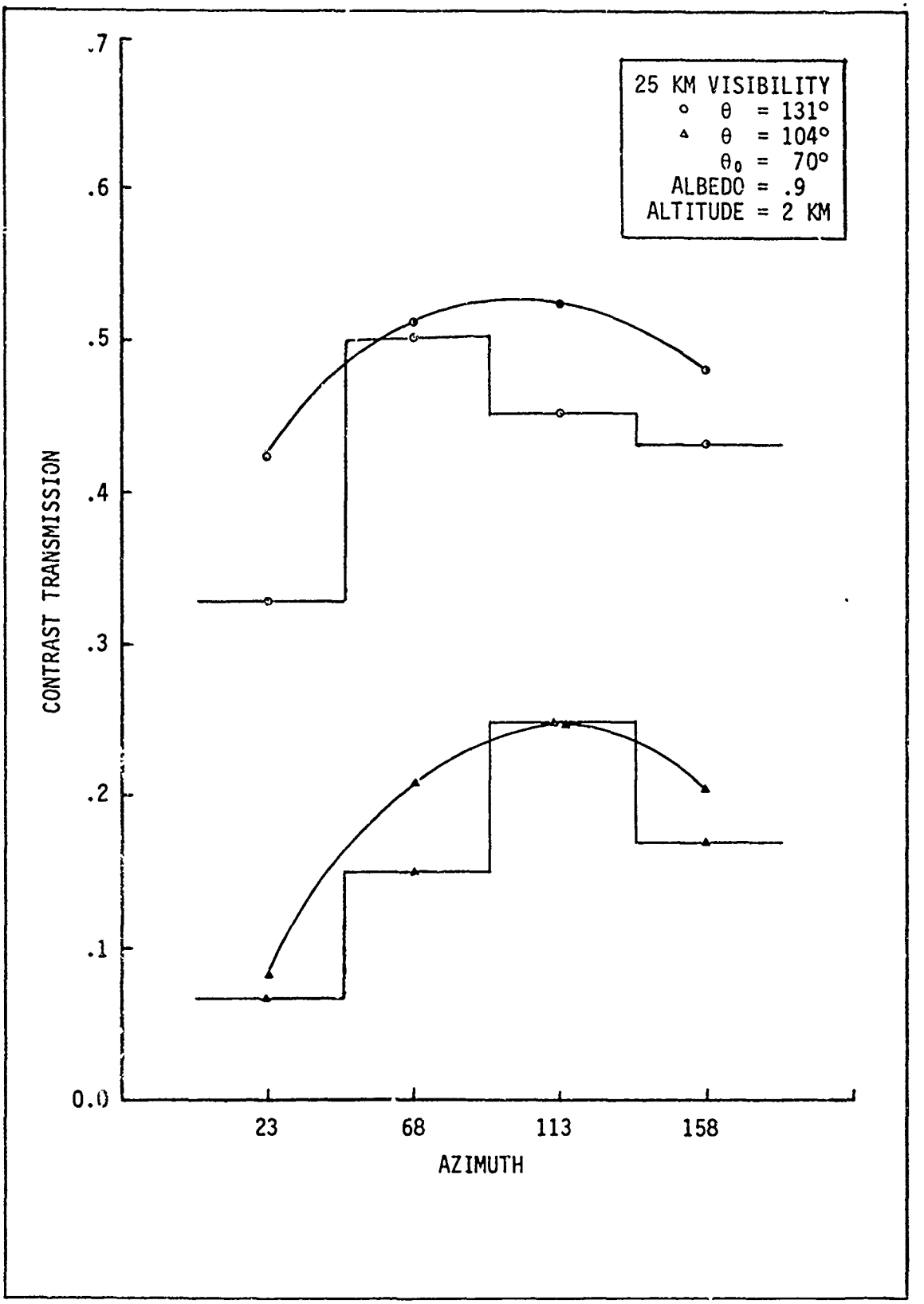

Fig. 26. Comparison of Calculation of Contrast Transmission by the AWS and RRA Monte Carlo Methods. The Wavelength is .55 μm, Solar Zenith Angle is 70°, Albedo is .1. The Surface Visibility is 25 KM.

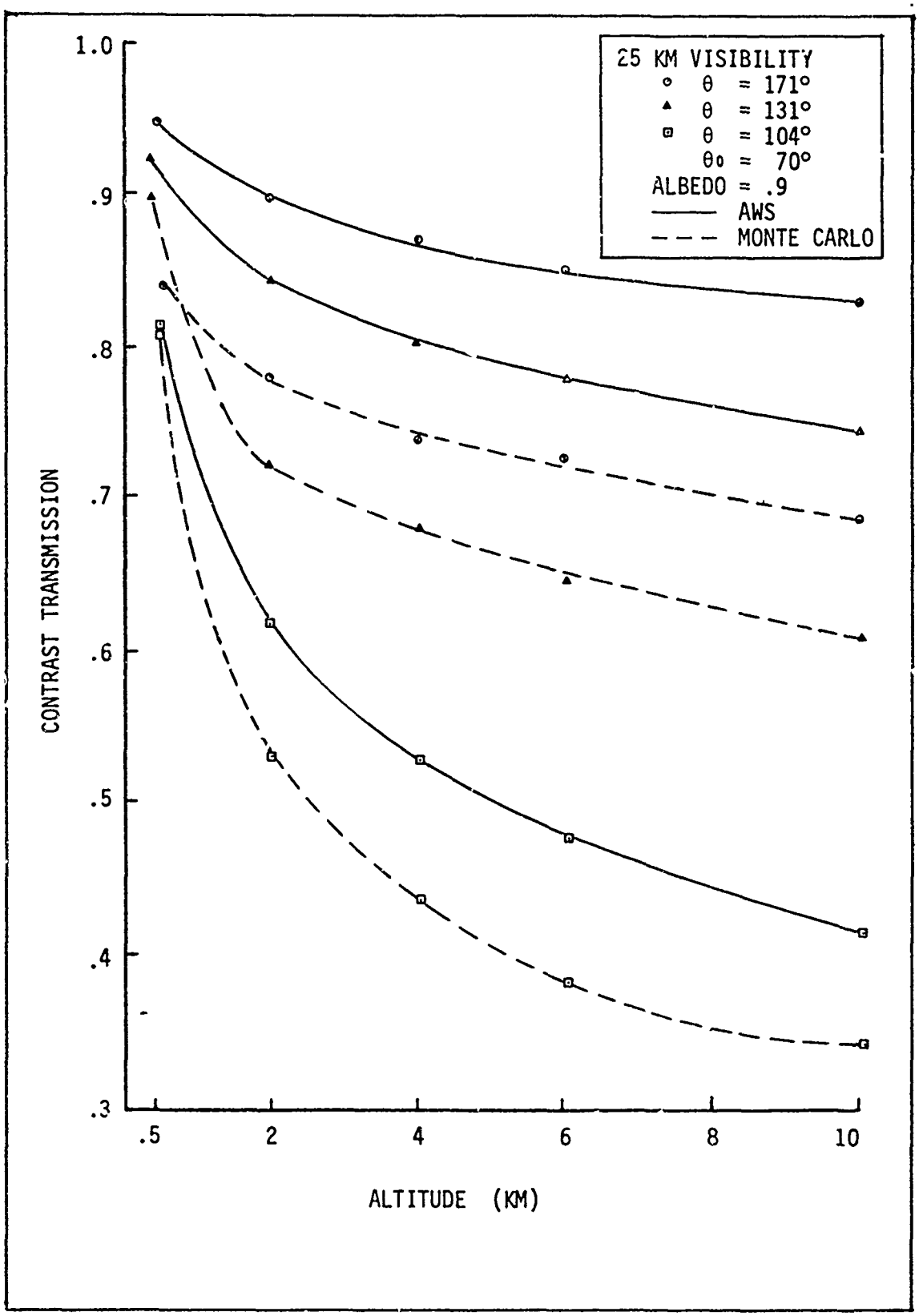

Fig. 27. Comparison of Calculation of Contrast Transmission by the AWS and RRA Monte Carlo Methods. The Wavelength is .55 μm, Solar Zenith Angle is 70°,Albedo is .9. The Surface Visibility is 25 KM.

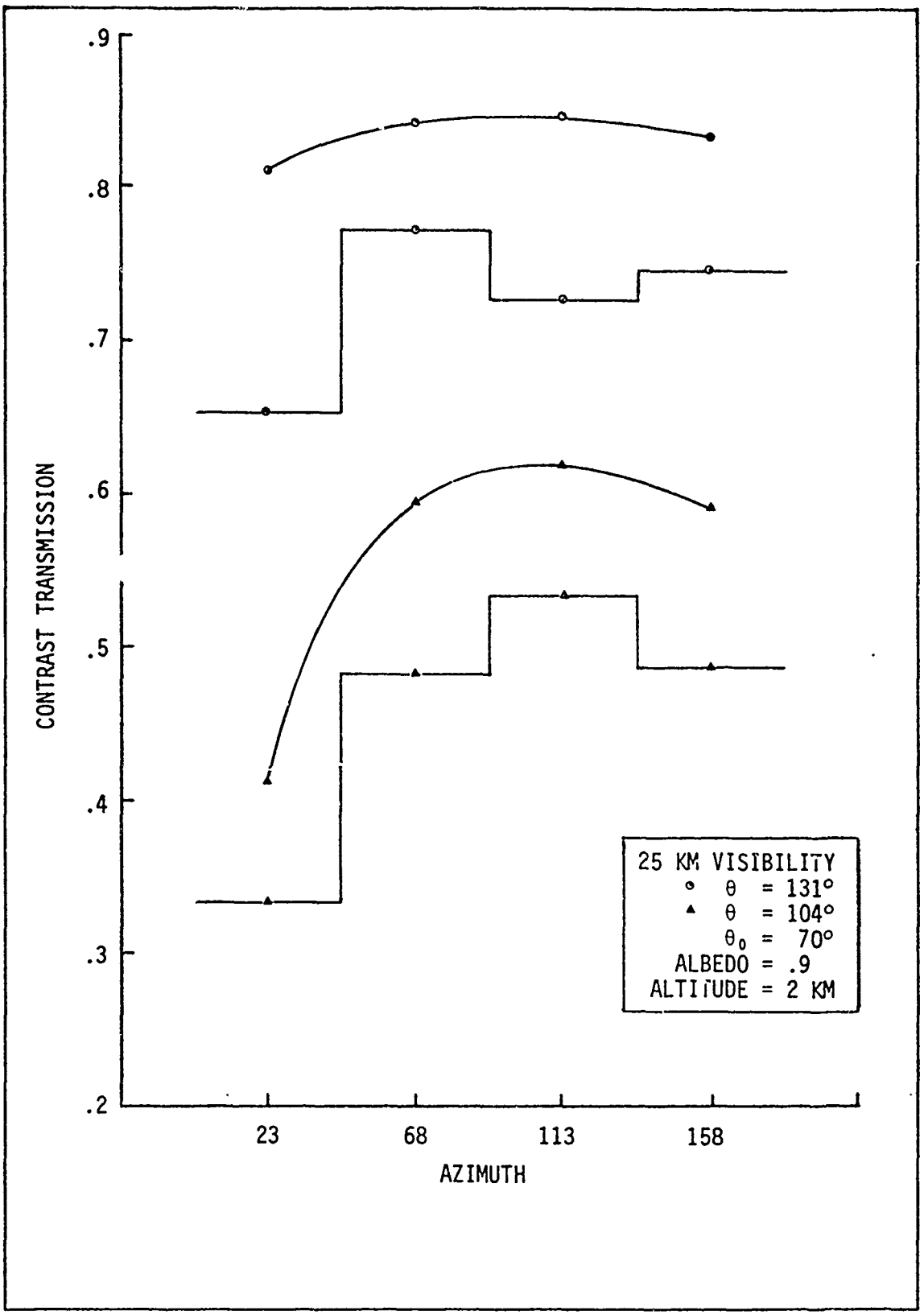

Fig. 28. Comparison of Calculation of Contrast Transmission by the AWS and RRA Monte Carlo Methods. The Wavelength is .55 μm, Solar Zenith Angle is 70°,Albedo is .9. The Surface Visibility is 25 KM.

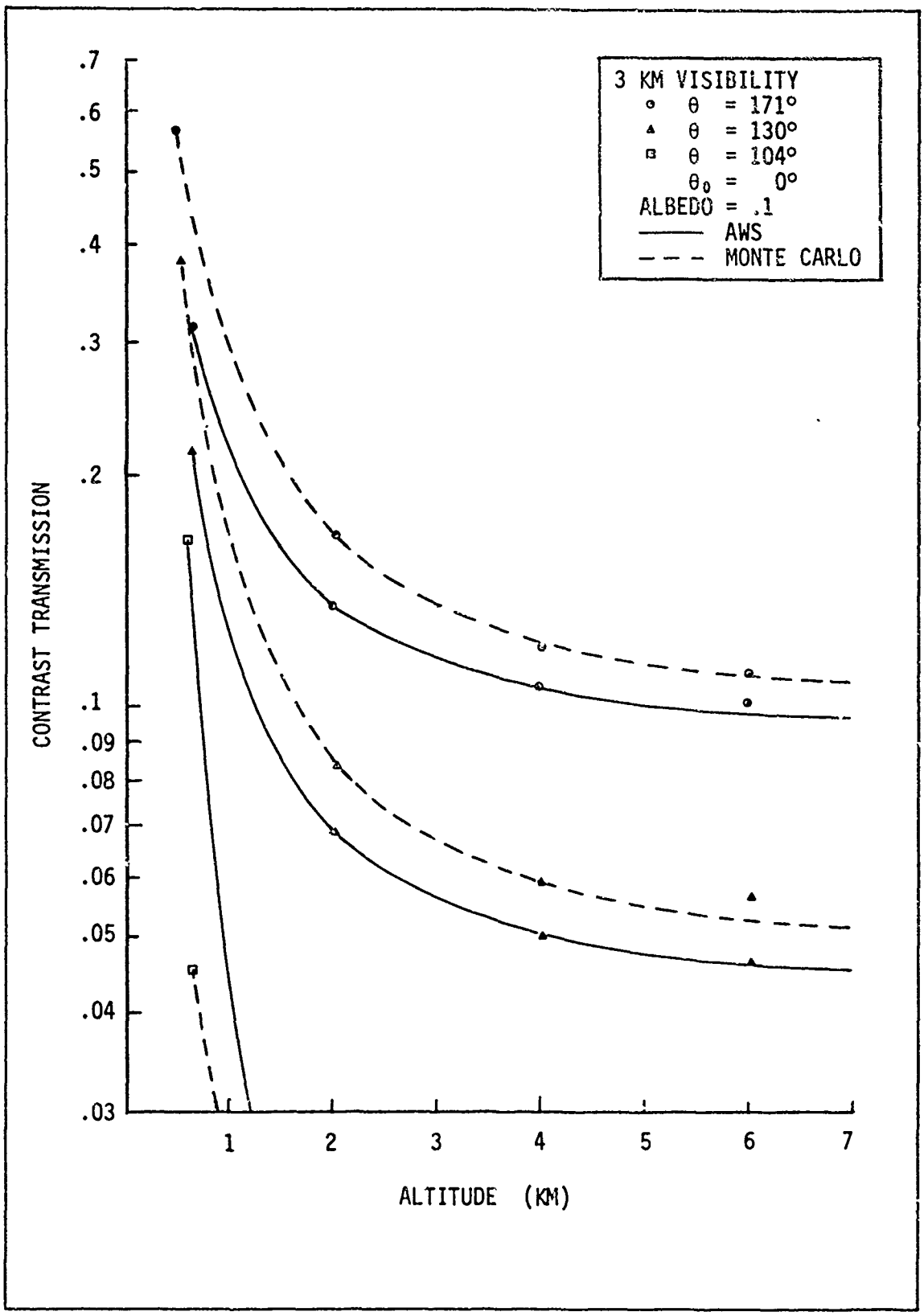

Fig. 29. Comparison of Calculation of Contrast Transmission by the AWS and RRA Monte Carlo Methods. The Wavelength is .55 μm, Solar Zenith Angle is 0°, Albedo is .1. The Surface Visibility is 3 KM.

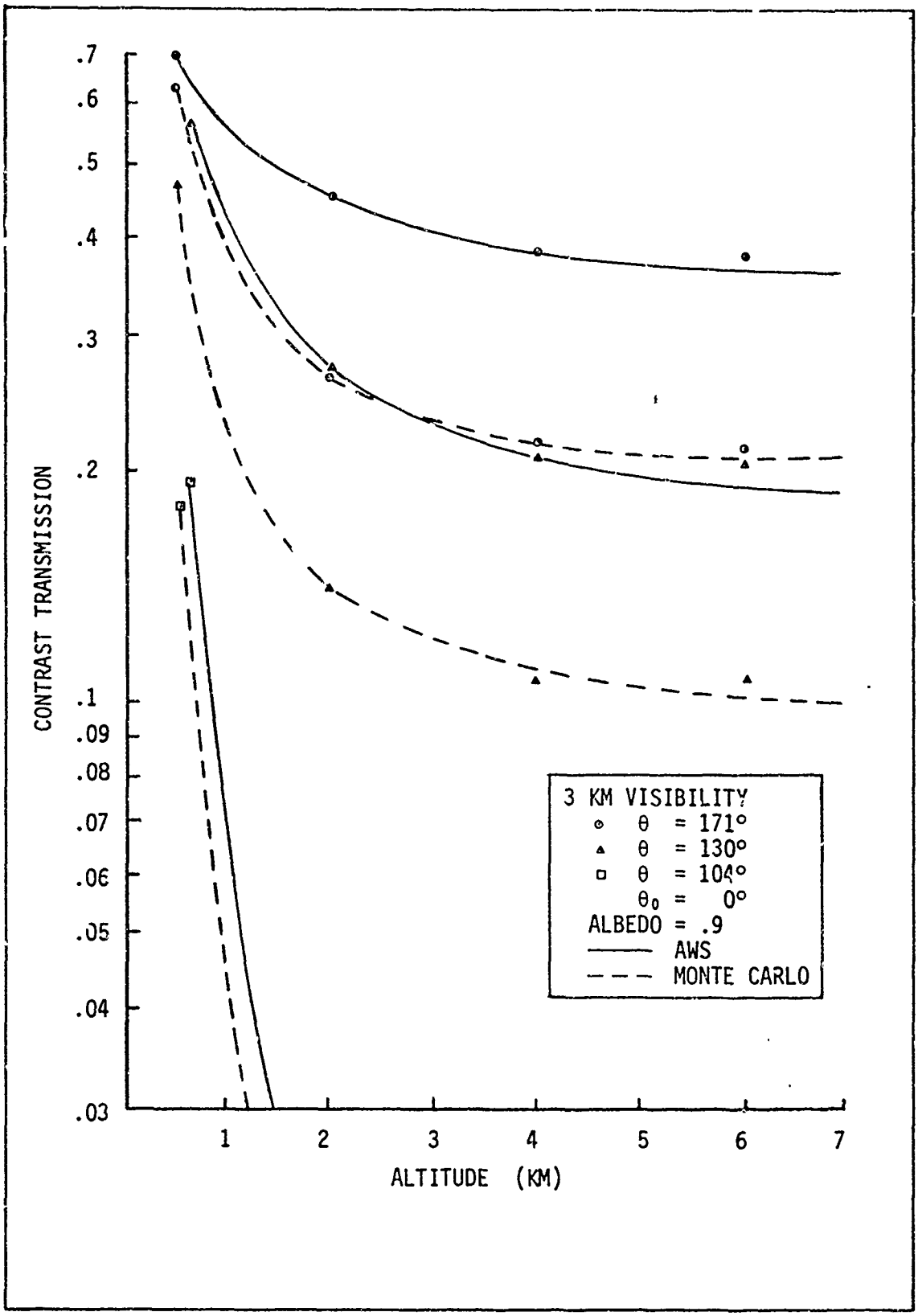

Fig. 30. Comparison of Calculation of Contrast Transmission by the AWS and RRA Monte Carlo Methods. The Wavelength is .55 μm, Solar Zenith Angle is 0°,Albedo is .9. The Surface Visibility is 3 KM.

albedo case. For the low albedo the AWS model is more pessimistic than the RRA Monte Carlo data, while for the high albedo the reverse is true. Figures 31 and 32 show the cases for solar zenith of 30° at an azimuth of 113°, and the low and high albedos. Again the agreement is quite good for the low albedo case with the Monte Carlo generally slightly higher although the data does cross for the look angle of 171°. For the high albedo case the AWS data predicts significantly higher results than the Monte Carlo data. The azimuth dependence is shown in Figs. 33 and 34. Here the data is plotted for an altitude of 2 KM. The agreement in shape is reasonable, but note the relative insensitivity to azimuth of the AWS data. This insensitivity was also noted in the 25 KM data. Figures 35 and 36 show the case of low sun, a solar zenith angle of 75°, at 113° azimuth, for the two albedos. Note that the same trend occurs as for the higher suns but now the agreement is better for the high albedo while for the low albedo the AWS data is significantly lower than the Monte Carlo data. Figures 37 and 38 show the azimuth variation for this sun angle. Again the AWS data is quite insensitive to azimuth change. This difference seems to be significant since in comparison to the 25 KM data in Figs 26 and 28 somewhat more change might be expected.

Thus one may conclude here that for the 3 KM case, for the high sun cases with low albedo, the AWS data agrees well with the Monte Carlo data with a trend to be slightly pessimistic. For the high albedo case, the AWS data predicts significantly higher results than the RRA model. For the low sun case the AWS data is significantly low for the low albedo case but agrees well for the high albedo case where it tends to be slightly more optimistic. The AWS data also appears to be much less sensitive to azimuth in the low visibility case than does the Monte Carlo data. So if one is to

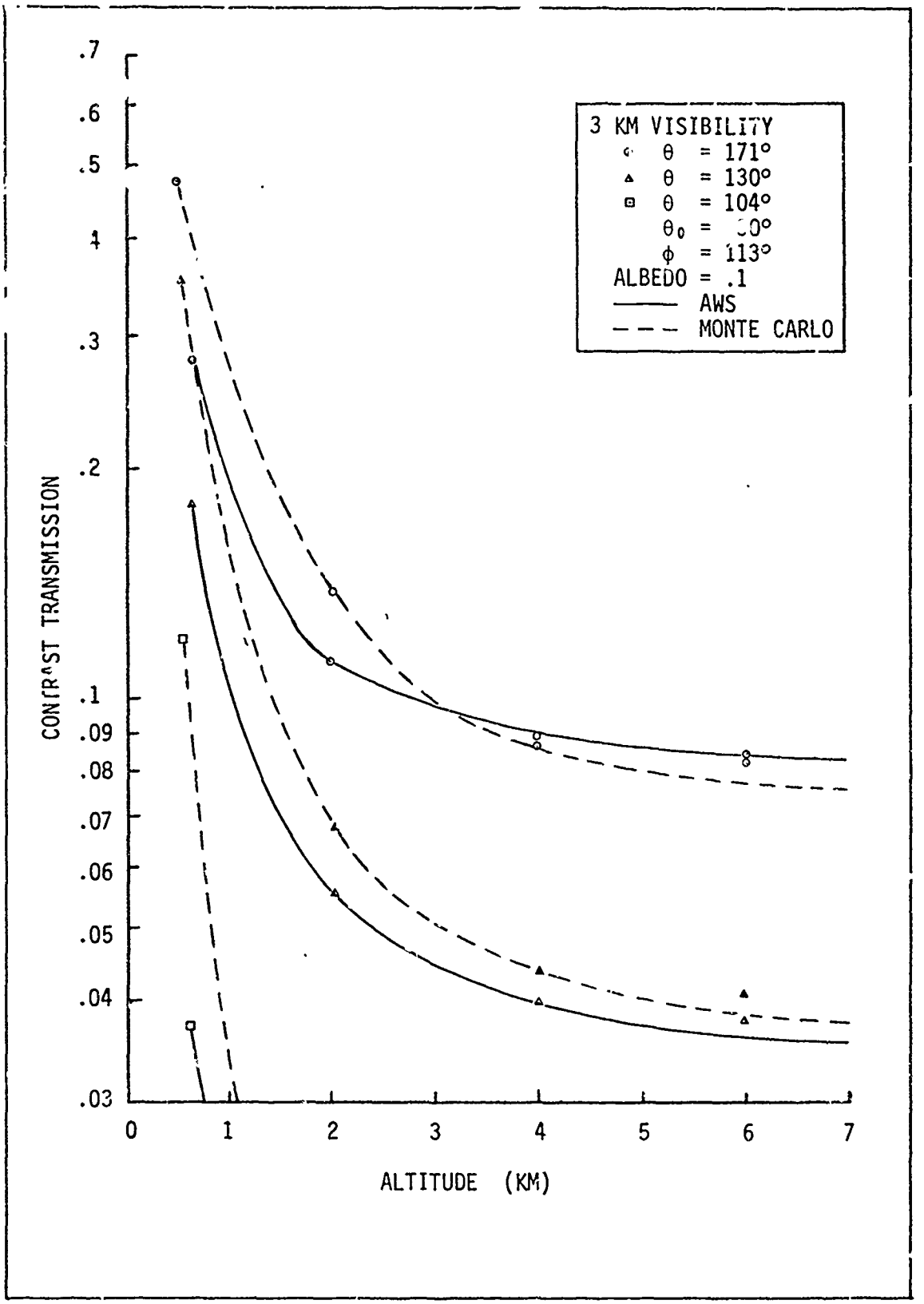

Fig. 31. Comparison of Calculation of Contrast Transmission by the AWS and RRA Monte Carlo Methods. The Wavelength is .55 μm, Solar Zenith Angle is 30°, Albedo is .1. The Surface Visibility is 3 KM.

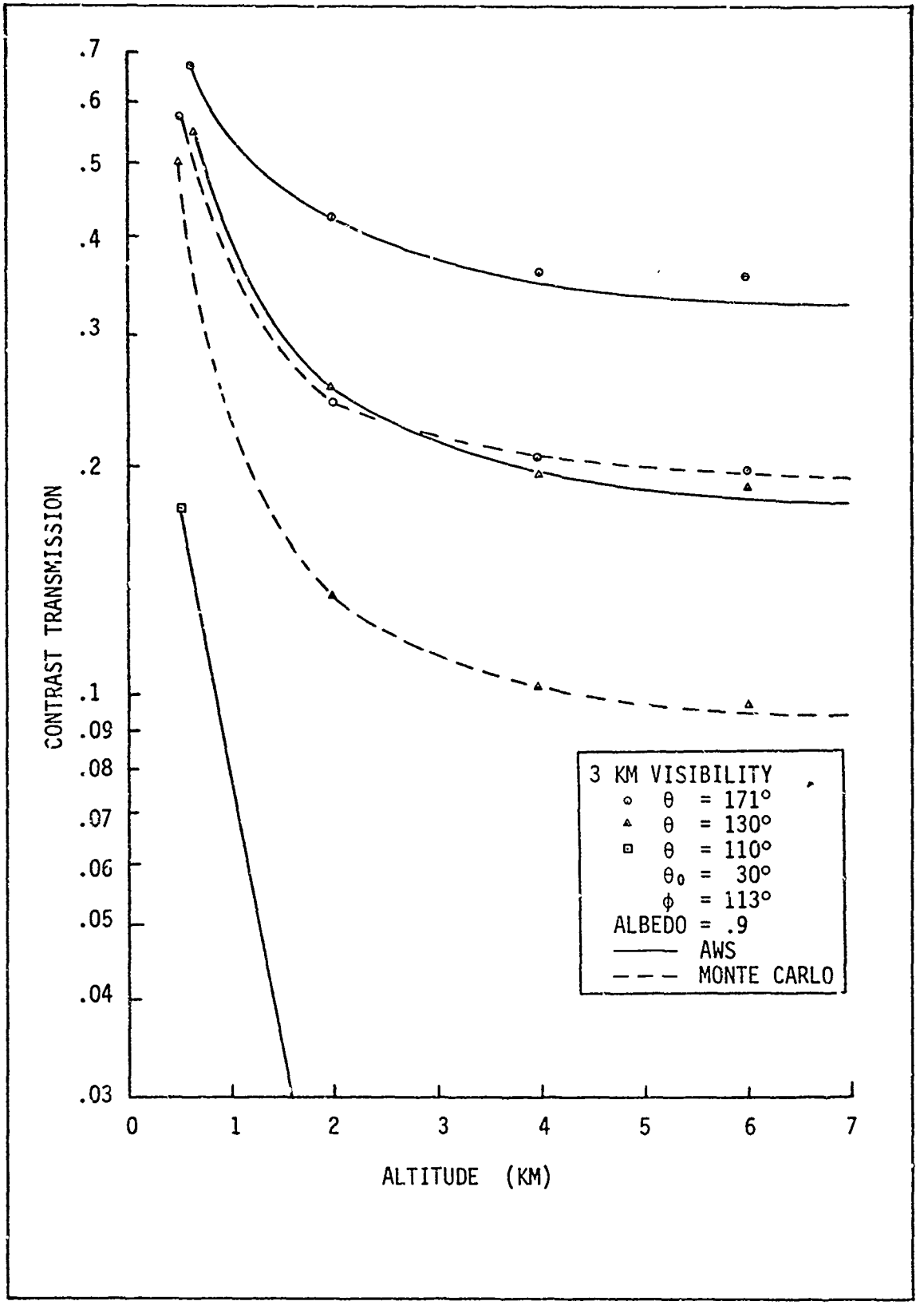

Fig. 32. Comparison of Calculation of Contrast Transmission by the AWS and RRA Monte Carlo Methods. The Wavelength is .55 μm, Solar Zenith Angle is 30°, Albedo is .9. The Surface Visibility is 3 KM.

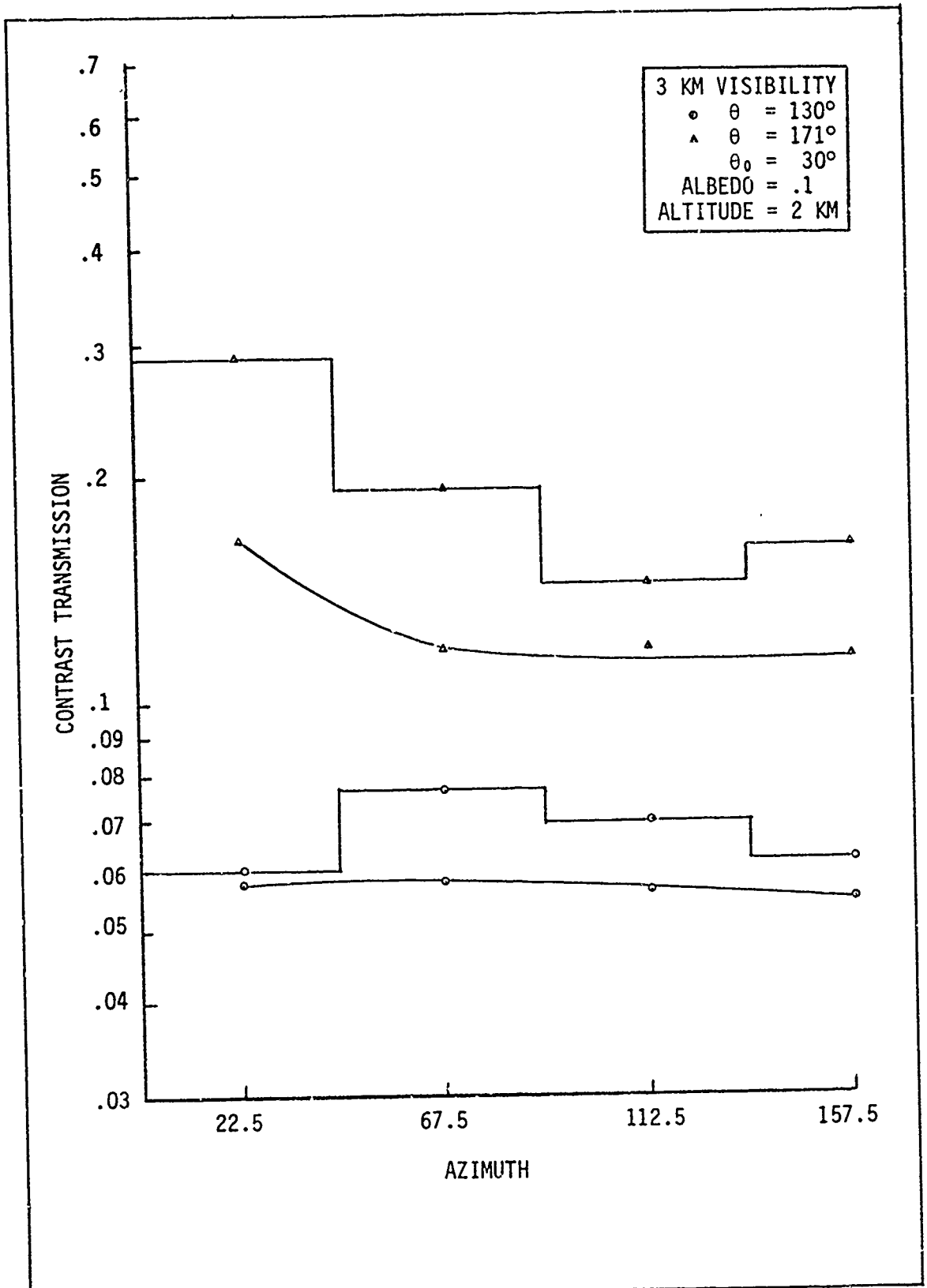

Fig. 33. Comparison of Calculation of Contrast Transmission by the AWS and RRA Monte Carlo Methods. The Wavelength is .55 μm, Solar Zenith Angle is 30°, Albedo is .1. The Surface Visibility is 3 KM.

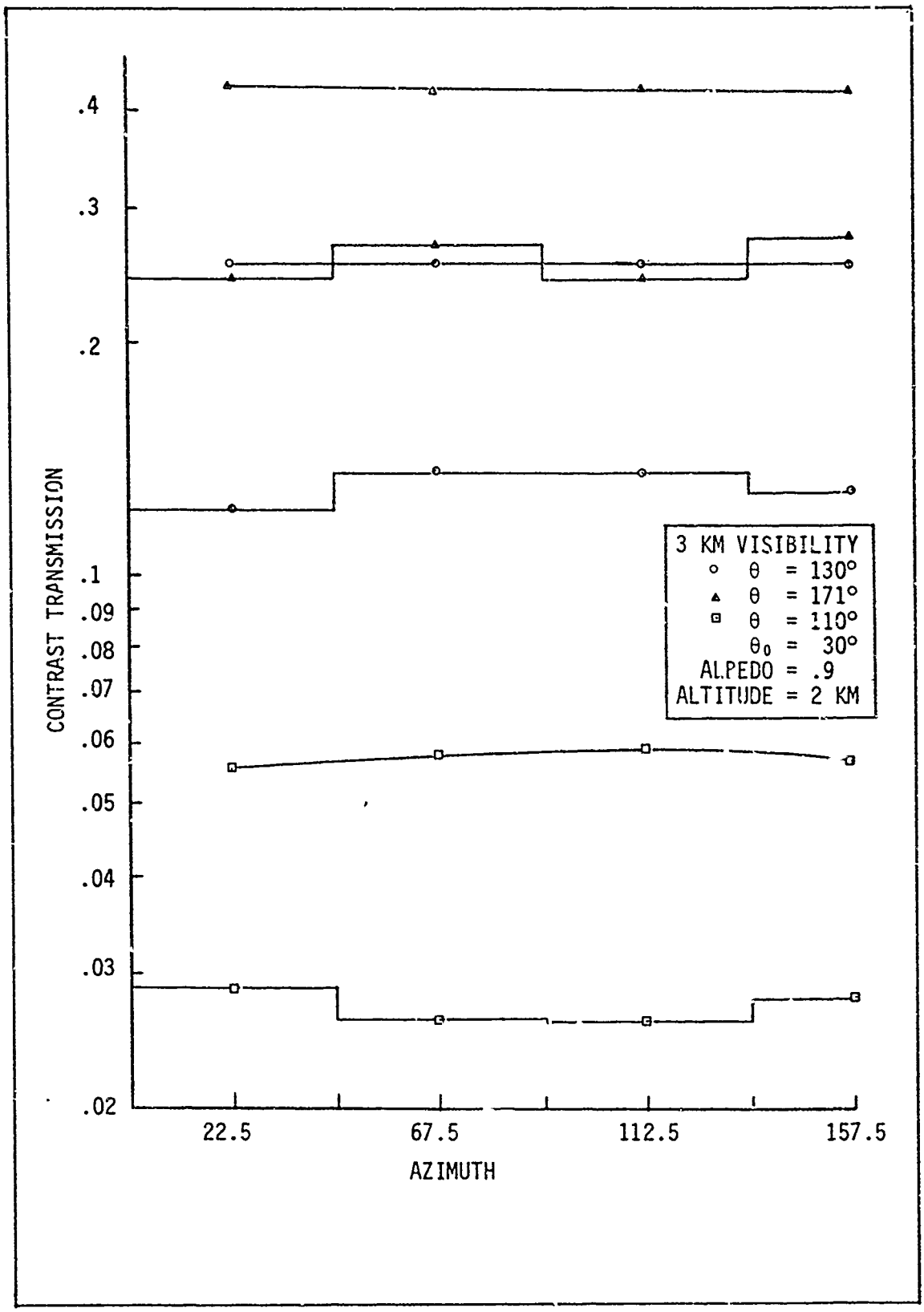

Fig. 34. Comparison of Calculation of Contrast Transmission by the AWS and RRA Monte Carlo Methods. The Wavelength is .55 μm, Solar Zenith Angle is 30°, Albedo is .9. The Surface Visibility is 3 KM.

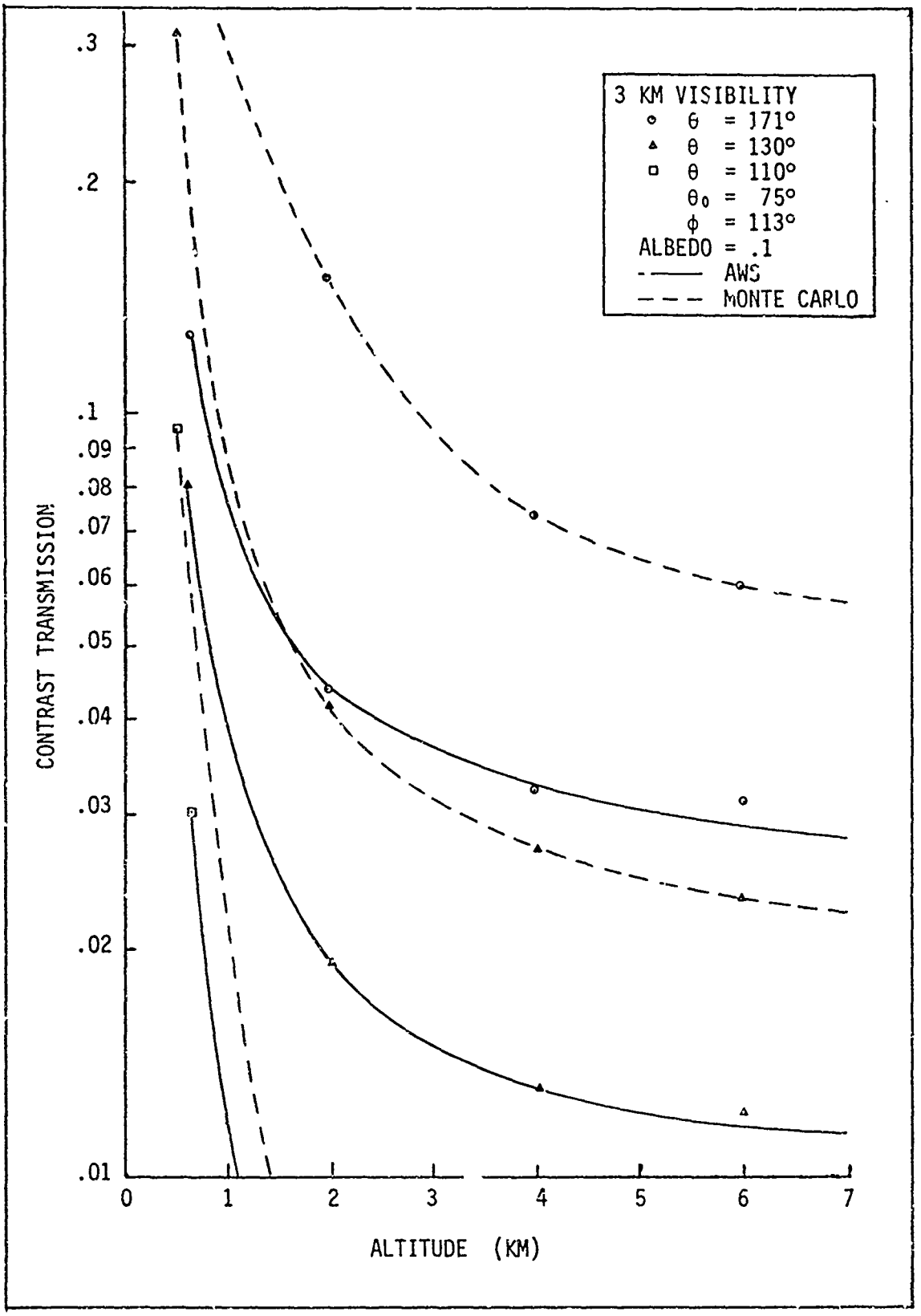

Fig. 35. Comparison of Calculation of Contrast Transmission by the AWS and RRA Monte Carlo Methods. The Wavelength is .55 μm, Solar Zenith Angle is 75°, Albedo is .1. The Surface Visibility is 3 KM.

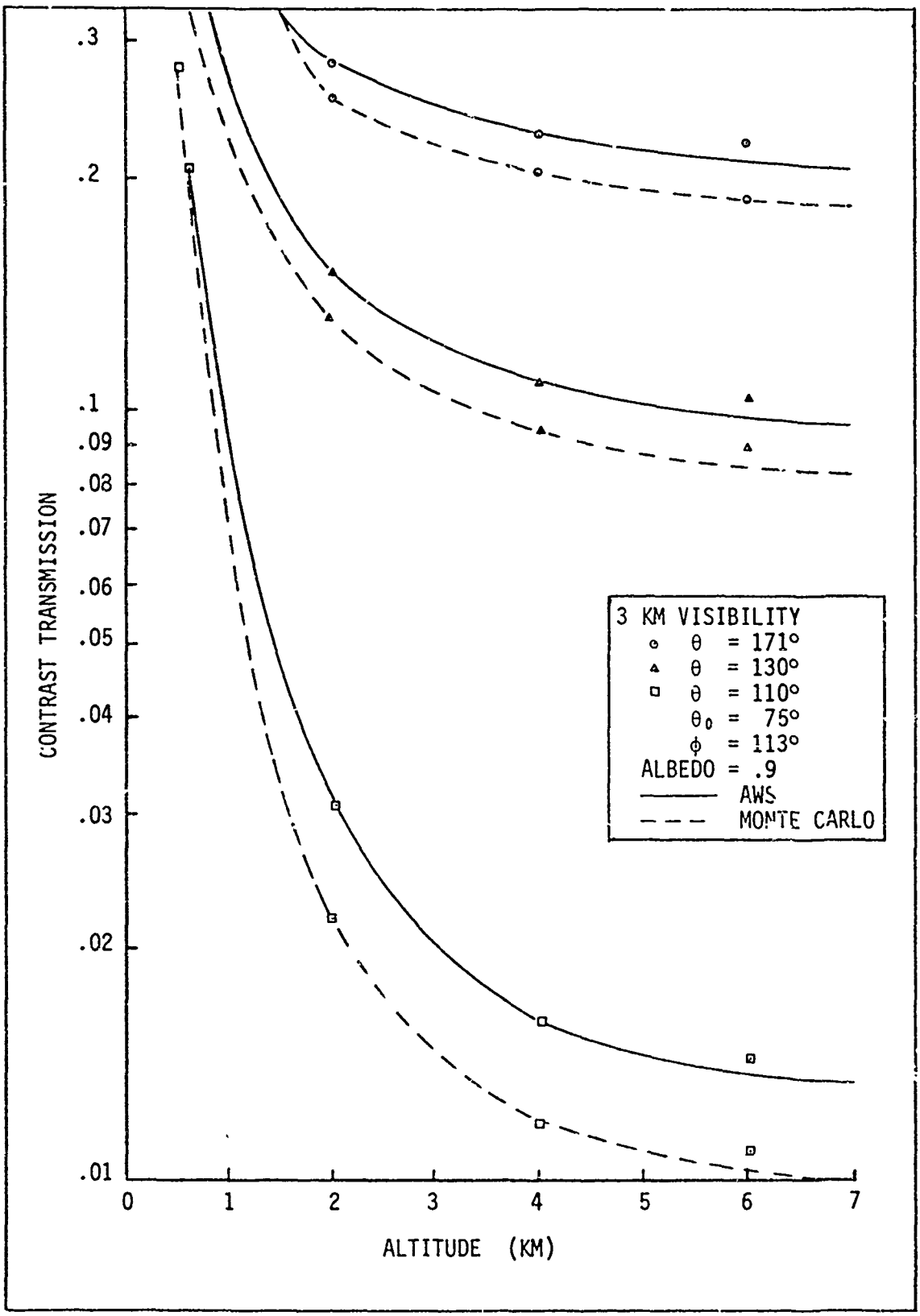

Fig. 36. Comparison of Calculation of Contrast Transmission by the AWS and RRA Monte Carlo Methods. The Wavelength is .55 μm, Solar Zenith Angle is 75°, Albedo is .9. The Surface Visibility is 3 KM.

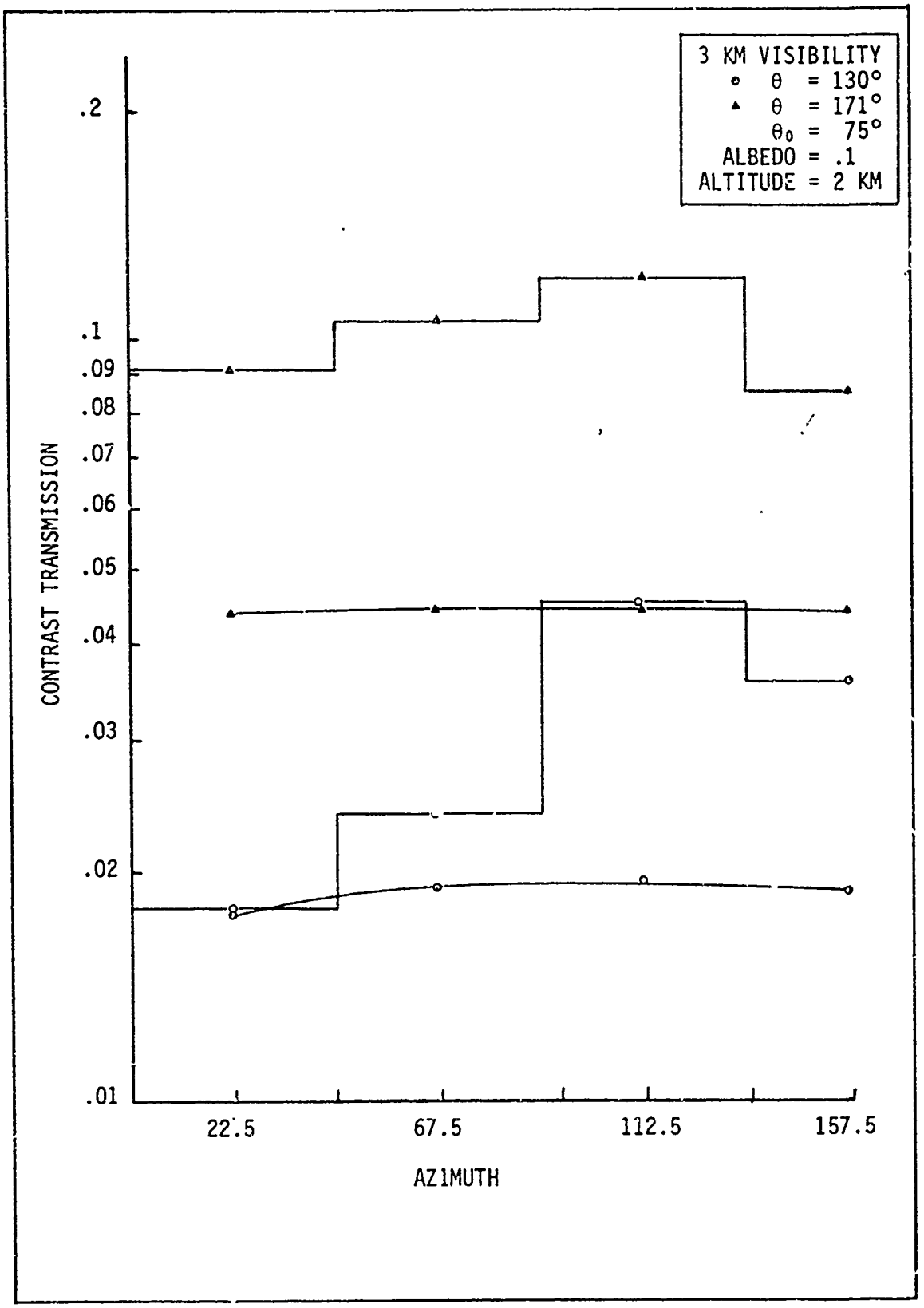

Fig. 37. Comparison of Calculation of ontrast Transmission by the AWS and RRA Monte Carlo Methods. The Wavelength is .55 μm, Solar Zenith Angle is 75°,Albedo is .1. The Surface Visibility is 3 KM.

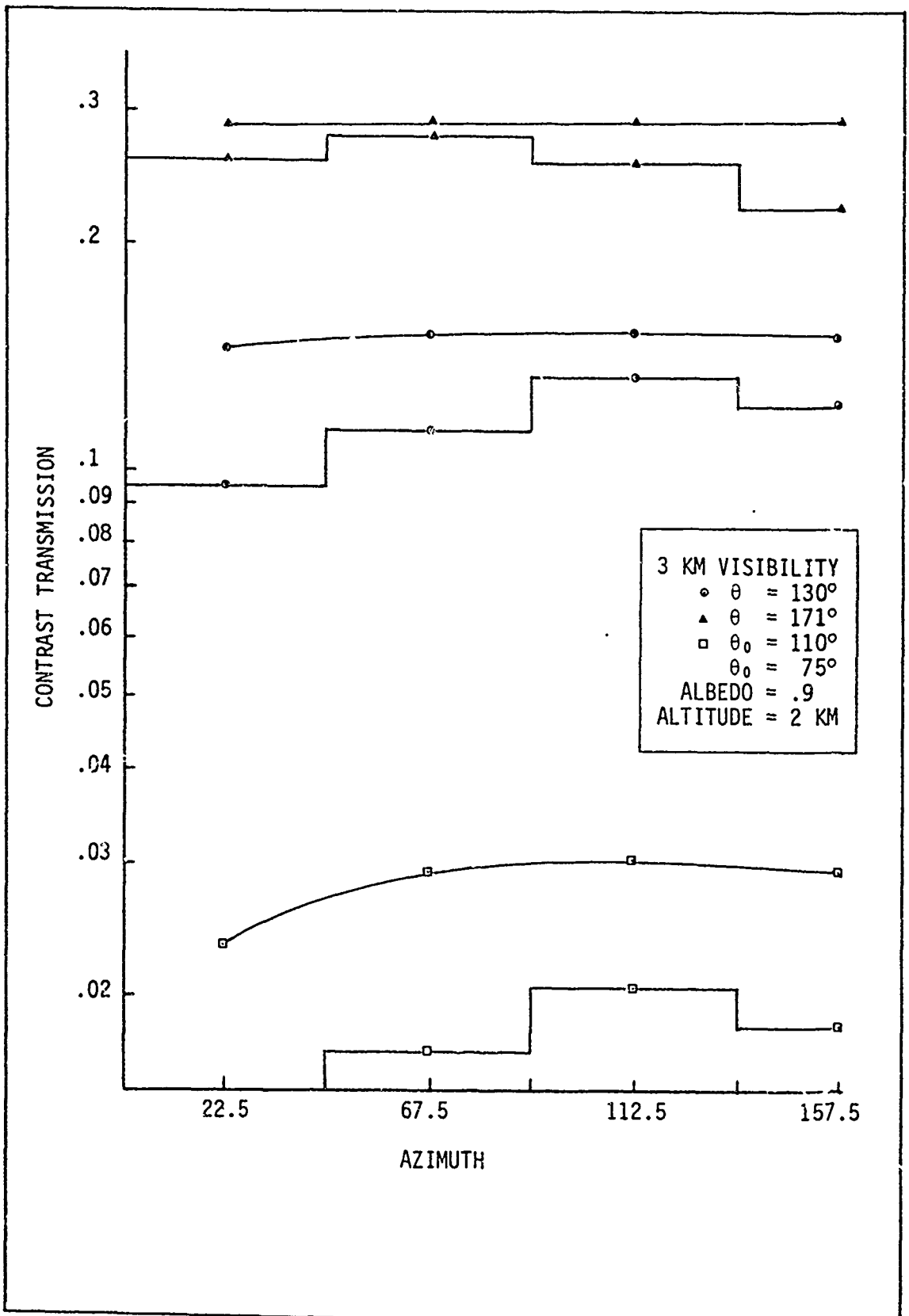

Fig. 38. Comparison of Calculation of Contrast Transmission by the AWS and RRA Monte Carlo Methods. The Wavelenyth is .55 μm, Solar Zenith Angle is 75°,Albedo is .9. The Surface Visibility is 3 KM.

use the AWS data for the low visibility case, more care is needed in handling the results.

Table VIII shows the overall performance of the AWS model compared to the RRA Monte Carlo data for the two visual ranges. Here the percentage of cases in which the AWS model predicted higher values of contrast transmission are shown as functions of sun zenith angle and albedo. This table

TABLE VIII

Percentage of Cases Where AWS Predicts Higher than RRA

Visibility	Albedo	Solar Zenith Angle		
		0°	30°	70°
25 KM	.1	83%	77%	79%
	.9	90%	96%	89%
3 KM	.1	28%	21%	17%
	.9	93%	100%	86%

tends to support the general trends noted in the previous figures. For the clear case, the AWS data is more optimistic than the RRA Monte Carlo data. For the low visibility case, AWS is more pessimistic for the low albedo and more optimistic for the high albedo case.

Table IX shows the percentage by which the AWS data predicts higher or lower than the Monte Carlo data. From Eq (75) a negative percentage indicates that the AWS data is predicting higher values of contrast transmission than the Monte Carlo data, and a positive percentage indicates AWS predicting lower. Also shown in parentheses is the standard deviation of the data set.

From Table IX it can be seen that the AWS model for the clear case

TABLE IX

Percentage Difference Between AWS and Monte Carlo Predictions of Contrast Transmission

Visibility	Albedo	Solar Zenith Angle 0°	30°	70°
25 KM	.1	-14% (17%)	-11% (14%)	-18% (21%)
	.9	-16% (12%)	-17% (11%)	-16% (12%)
3 KM	.1	11% (25%)	19% (21%)	30% (40%)
	.9	-80% (38%)	-70% (34%)	-28% (37%)

is uniformly predicting higher than the RRA data, and that the results are reasonably comparable for the six cases. If one felt that the Monte Carlo data were more accurate, he might use the AWS data because of its ease and quickness, and then scale the result according to the above table. A reasonable average might be -15%, so that one would divide the AWS predictions by 115% to get a number comparable to the RRA prediction.

From the inconsistency of the 3 KM results, the results of the simplifying assumptions of the AWS model with regard to the number of scattering events possible becomes apparent. But it should also be pointed out that the results of the AWS model are probably still useful, and they can be corrected from the above table to yield results in agreement with the Monte Carlo data.

In an attempt to determine the effect of the error introduced by using different input altitudes for the AWS and Monte Carlo data, the low altitude point was eliminated and the statistics recomputed. For the 25 KM case the percentage difference became more negative by 3 - 4%, but the standard deviation decreased by 1 - 3%. For the 3 KM case, the percentage

decreased 8 - 9% and standard deviation decreased 2 - 5% for the low albedo case. The percentage decreased 11 - 17% with standard deviation decreasing 4 - 18% for the high albedo case.

No attempt is made here to analyze why all the variation occurs, but much is probably due to the Monte Carlo data, since in the case of the solar zenith of 0°, the AWS program computes the same contrast transmission, independent of azimuth, while the Monte Carlo data does not. Thus the standard deviations which are present at zenith angle of 0° in the tables above are due in large part to the statistical nature of the Monte Carlo data. This statistical variation might be expected to carry over to the other solar zeniths as well.

Comparison to Flight Data

Calculations of contrast transmission based on the AWS model are compared to data collected in flight during Project Haven View (Ref 9). The flight measurement techniques were previously described in Chapter II. The processed data included $R^*(Z,\theta,\phi)$, $T(Z,\theta)$, and ${}_bR_0(Z_t,\theta,\phi)$. The data was presented for a narrow blue and a narrow red filter, and the photopic, and S-20 response. Here, only the photopic data is used. With R^*, and ${}_bR_0$, Eq (58) may be used to calculate $\tau_c(Z,\theta,\phi)$. The general weather conditions and solar zenith angle are shown in Table II in Chapter II.

The AWS data was calculated for a wavelength of .55 μm. The assumption that this is representative of the photopic region is made. Several visibility models were used to try to match the results of the model and flight data. The AWS model with a surface visibility of 15 KM gave the best fit in the three flights compared here.

The percentage difference between the flight data and the AWS calculation of contrast transmission is presented in Table X for three flights.

The standard deviation of the data is also reported in parentheses. Each entry is averaged over five altitudes and seven receiver zenith angles of 93°, 95°, 97°, 100°, 120°, 150°, and 180°. Slant ranges greater than 15 KM were ignored in the calculations.

TABLE X

Percentage Difference Between Flight and AWS Calculation of Contrast Transmission

Flight (see Chap II)	Azimuth From Sun 0°	90°	180°	Averaged
c-142	-21% (26%)	-2.4% (14%)	-6% (23.5%)	-10% (23%)
c-139	-6.5% (16%)	-3.8% (17%)	-.5% (16%)	-3.6% (16%)
c-137	-10% (23%)	-6% (24%)	-.5% (23%)	-5% (16%)

One may note first that the comparison is reasonable between the two sets of data. The azimuth of 0° is the largest difference, indicating that the AWS model may not be handling the multiple scattering well enough. Of course the comparison should not be carried too far, since the flight data was taken under skies which had varying amounts of clouds which the AWS model does not take into account. Also there is a rather wide disparity between the reported visibility at the time of the flight and the visibility used in the model (15 KM).

The scattering coefficient data measured in-flight shows that the flights had rather similar visibilities at the lowest altitude (between 22 and 26 KM) but that a strong inversion was present in all flights at about 1.5 KM, causing the extinction coefficient to be nearly constant up to that altitude. The exponential decrease in aerosol extinction coefficient up to 4 KM in the AWS model would not approximate the true profile

closely. The choice of a lower surface visibility in the AWS model caused the air-transmittance to match better so that the above reasonable comparison could be achieved.

The mismatch between atmospheric profiles here points out the need for continued flight testing to measure actual atmospheres so that adequate atmospheric models can be constructed for particular areas and particular weather patterns. The AWS program and most other atmospheric simulation programs contain the flexibility to enter any atmospheric extinction coefficient profile if it can be estimated. If not, the best model must be used.

V. Calculated Directional Path Reflectance and Contrast Transmission

In this chapter of the report, calculations are made for various combinations of conditions of sun position and geometry at $\lambda = .55$ μm. The AWS model is used to generate spectral directional path reflectance $R^*(Z,\theta,\phi)$ for each combination of solar zenith angle, geometry, and albedo. This data is then displayed in two forms. Directional path reflectance is plotted against azimuth for a constant altitude, so that the effect of the azimuth of the path of sight with respect to the sun may be determined. Then contours of constant directional path reflectance are plotted as a function of altitude and horizontal range. This presentation allows the effects of receiver zenith angle (or dive angle) to be determined.

The contours of constant R^* are determined by generating a table of values of $R^*(Z,\theta,\phi)$ for 10 values of altitude between 1 and 10 KFT; for 10 values of θ between 95° and 180°; and for 9 values of ϕ between 0° and 180°. Then θ and ϕ are held constant, and Z is determined such that R^* has one of several fixed values. The interpolation is done using the $\log_{10}R^*$ and $\log_{10}Z$ to improve the accuracy, and a straight line interpolation routine is used. Then slant range is calculated from Range (R^* = constant) = $Z|\sec\theta|$. This computed range is plotted against receiver zenith angle and the values of slant range for constant R^* are connected with straight lines.

Contours of constant contrast transmission are generated from the $R^*(Z,\theta,\phi)$ data in a similar way. Equation (58), repeated here, is used to determine $\tau_c(Z,\theta,\phi)$ where the ${}_bR_0(Z_t,\theta,\phi)$ data is taken from measured data

in the photopic region for the same solar zenith angle and albedo.

$$\tau_c(Z,\theta,\phi) = \{1 + [R^*(Z,\theta,\phi)/{}_bR_0(Z_t,\theta,\phi)]\}^{-1}$$

The assumption is made that the R* calculated at .55 μm is representative of a non-spectral R* for the entire photopic region. Then the contrast transmission is representative of the photopic region. The same interpolation method as for R* above is used to determine the contours of constant contrast transmission.

With presentations of this type it appears that a good start may be made into predicting lock-on ranges or detection ranges for sensor systems. The presentations should also be quite useful for predicting the areas of azimuth and dive angle where the effects of non-image forming light will be at a minimum; thus the seeing conditions should be the best for whatever sensor system is being used.

The data presented here from the AWS model calculations is computed for the same solar zenith and albedo as for flight data previously reported by Duntley in Ref 7, Appendices C and D. The ${}_DR_0(Z_t,\theta,\phi)$ is taken from earlier publications. As noted in Chapter III of this report, other background surfaces have also been measured under similar conditions and their directional reflectances may be used. Table XI shows the values of the parameters for which data is presented. The figures are self-explanatory. The AWS model or other mathematical model easily generates them for any situation of interest and allows parameters such as visibility, solar zenith angle and albedo to be varied to determine their effects on contrast transmission.

TABLE XI

Parameters for AWS Calculations

Solar Zenith Angle	Albedo	Altitudes	Visibility	Reference for $_bR_0$ data
42°	.06	1-10 KFT	23 KM	(Ref 26:559), also see Chap. III, Figs. 16 and 17
78°	.06	1-10 KFT	23 KM	(Ref 23:804)

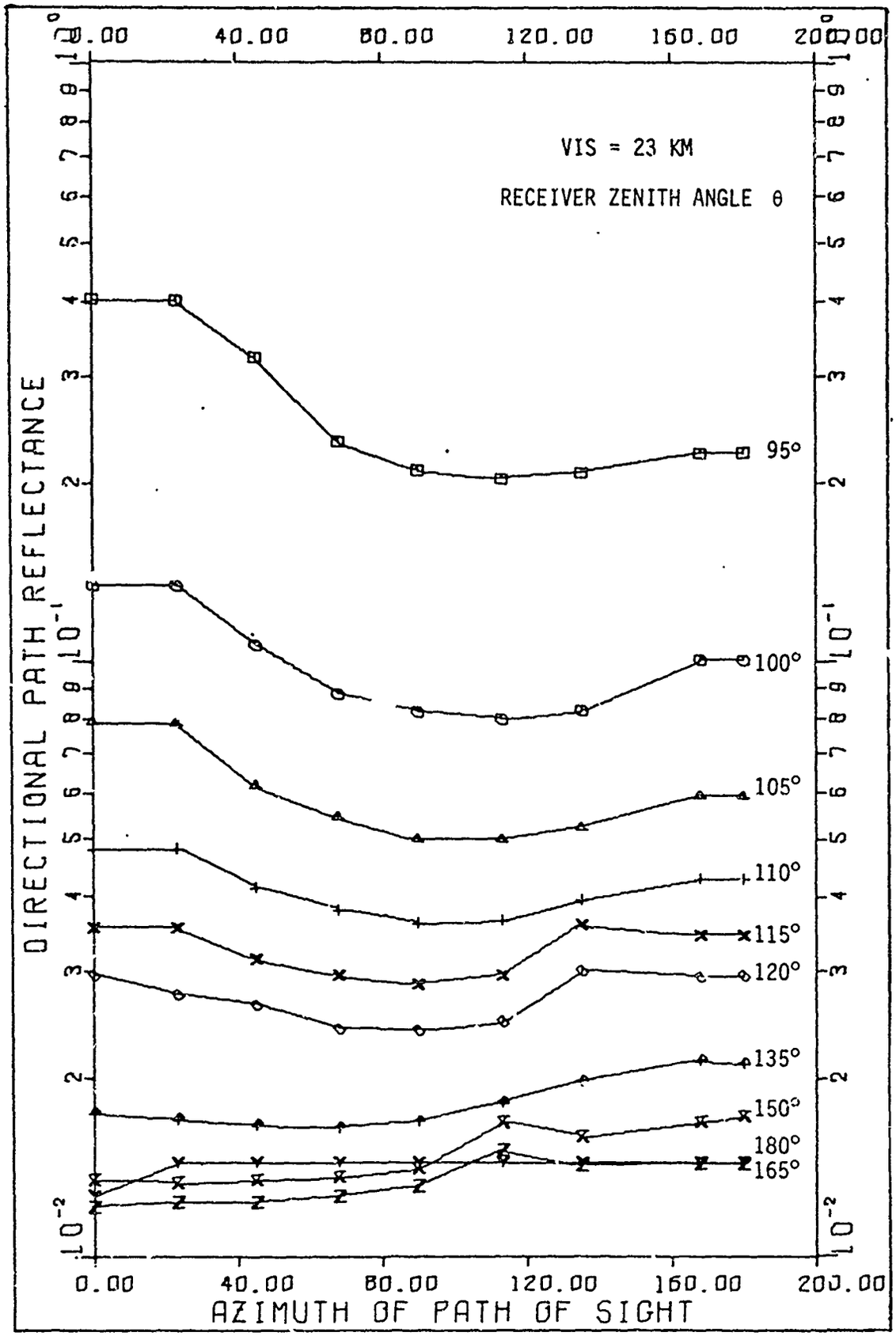

Fig. 39. Directional Path Reflectance Versus Azimuth for a Solar Zenith Angle of 42°. The Albedo is .06, Wavelength is .55 μm and the Altitude is 2 KM. Data from AWS Model.

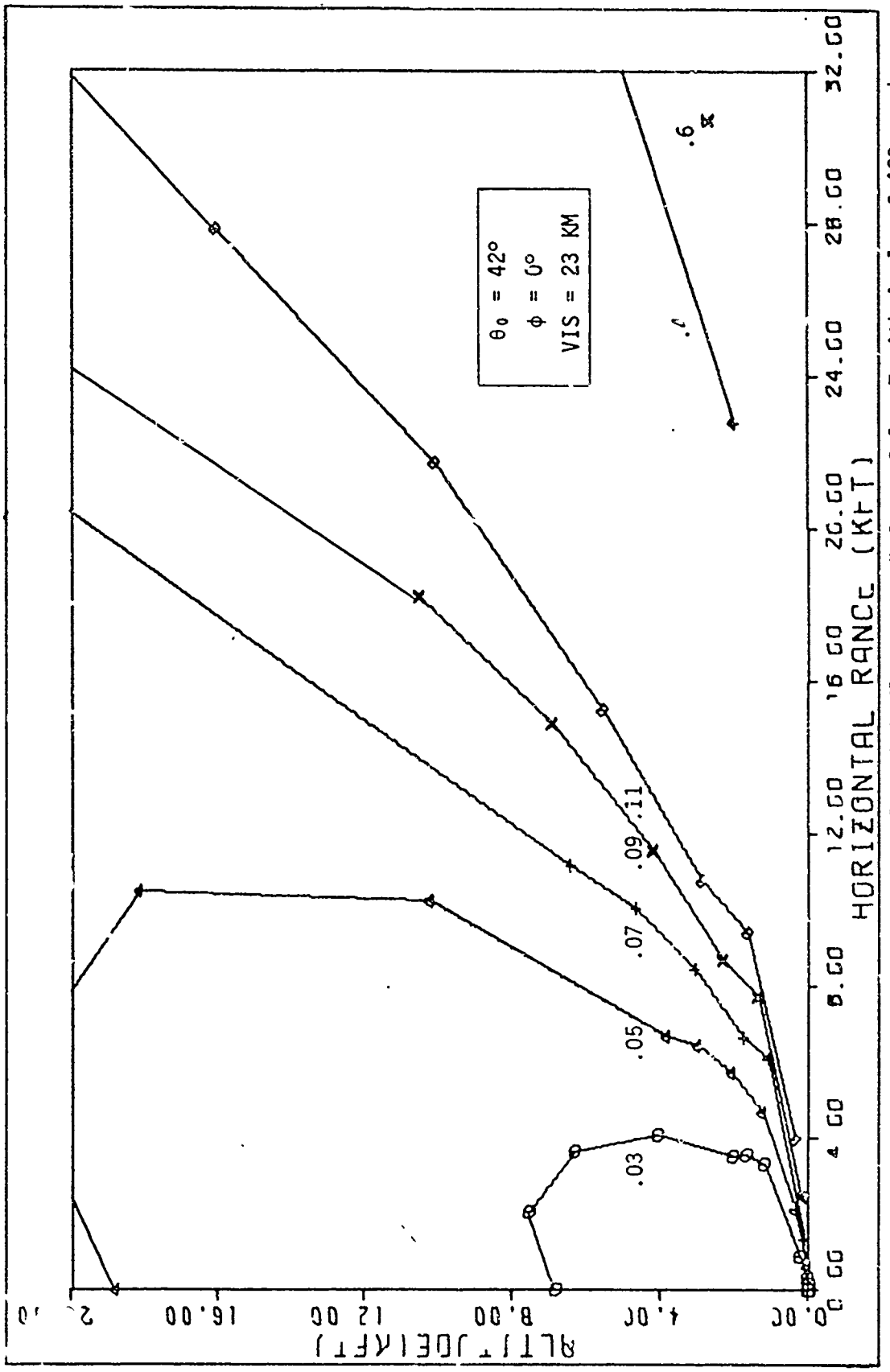

Fig. 40. Contours of Constant Directional Path Reflectance R* for a Solar Zenith Angle of 42°, and an Azimuth of 0°. The Albedo is .06 and the Wavelength is .55 μm. Data from AWS Model.

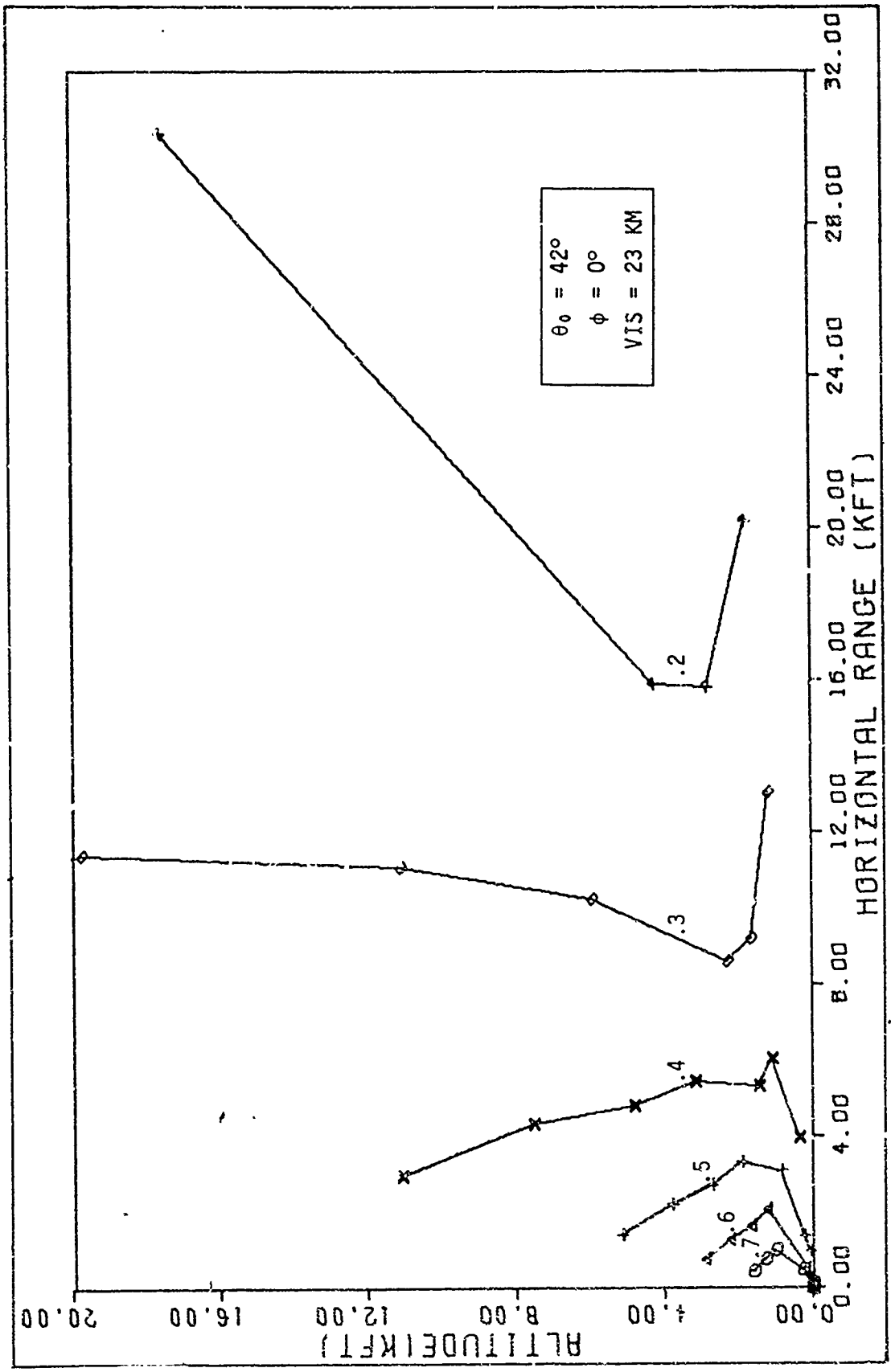

Fig. 41. Contours of Constant Contrast Transmission τ_C, for a Solar Zenith Angle of 42°, and an Azimuth of 0°. The Albedo is .06, and the Wavelength is .55 μm. R* Data is from AWS Model, ${}_bR_0$ Data is Measured Background Reflectance.

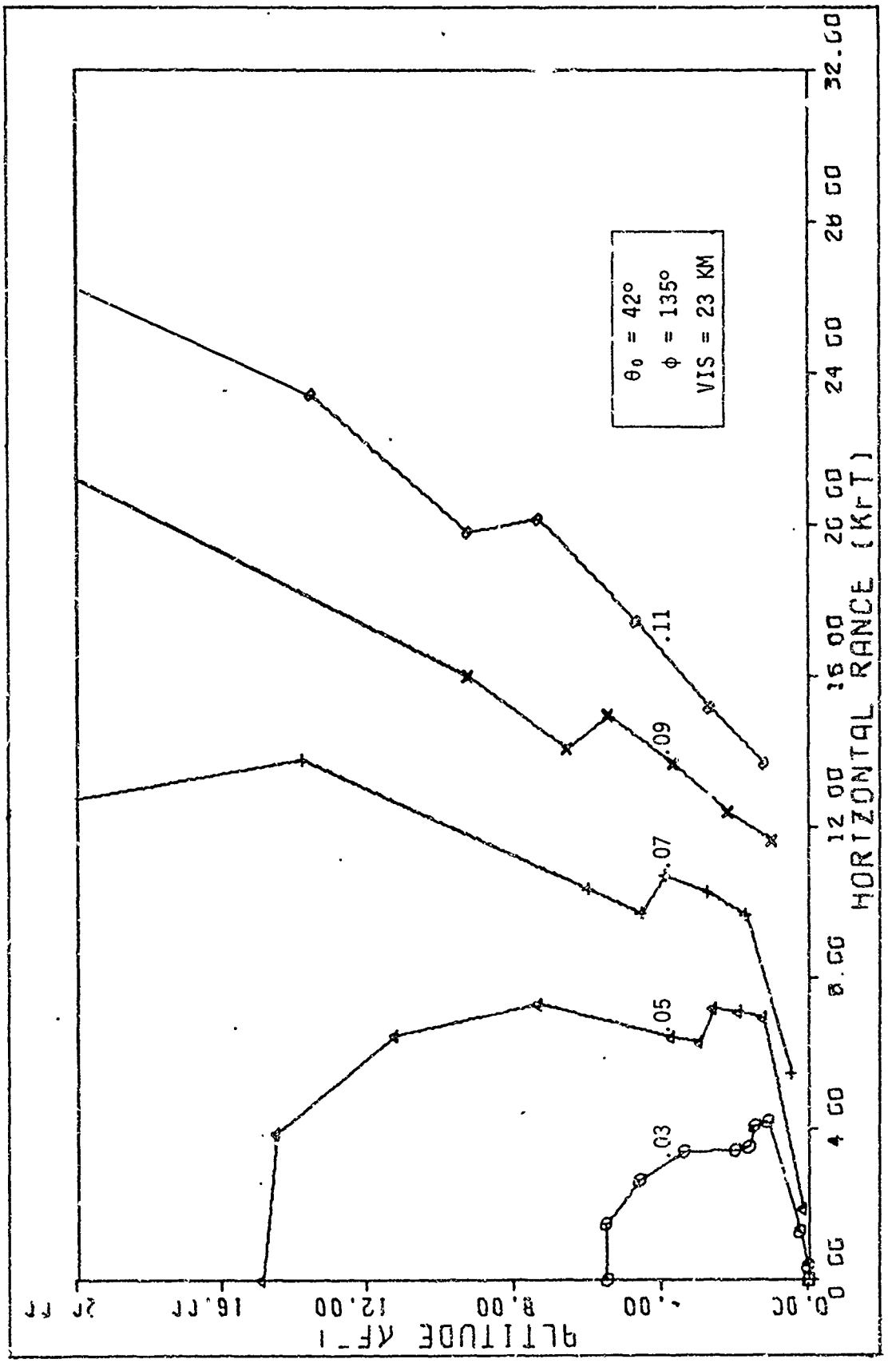

Fig. 42. Contours of Constant Directional Path Reflectance R* for a Solar Zenith Angle of 42°, and an Azimuth of 135°. The Albedo is .06 and the Wavelength is .55 μm. Data from AWS Model.

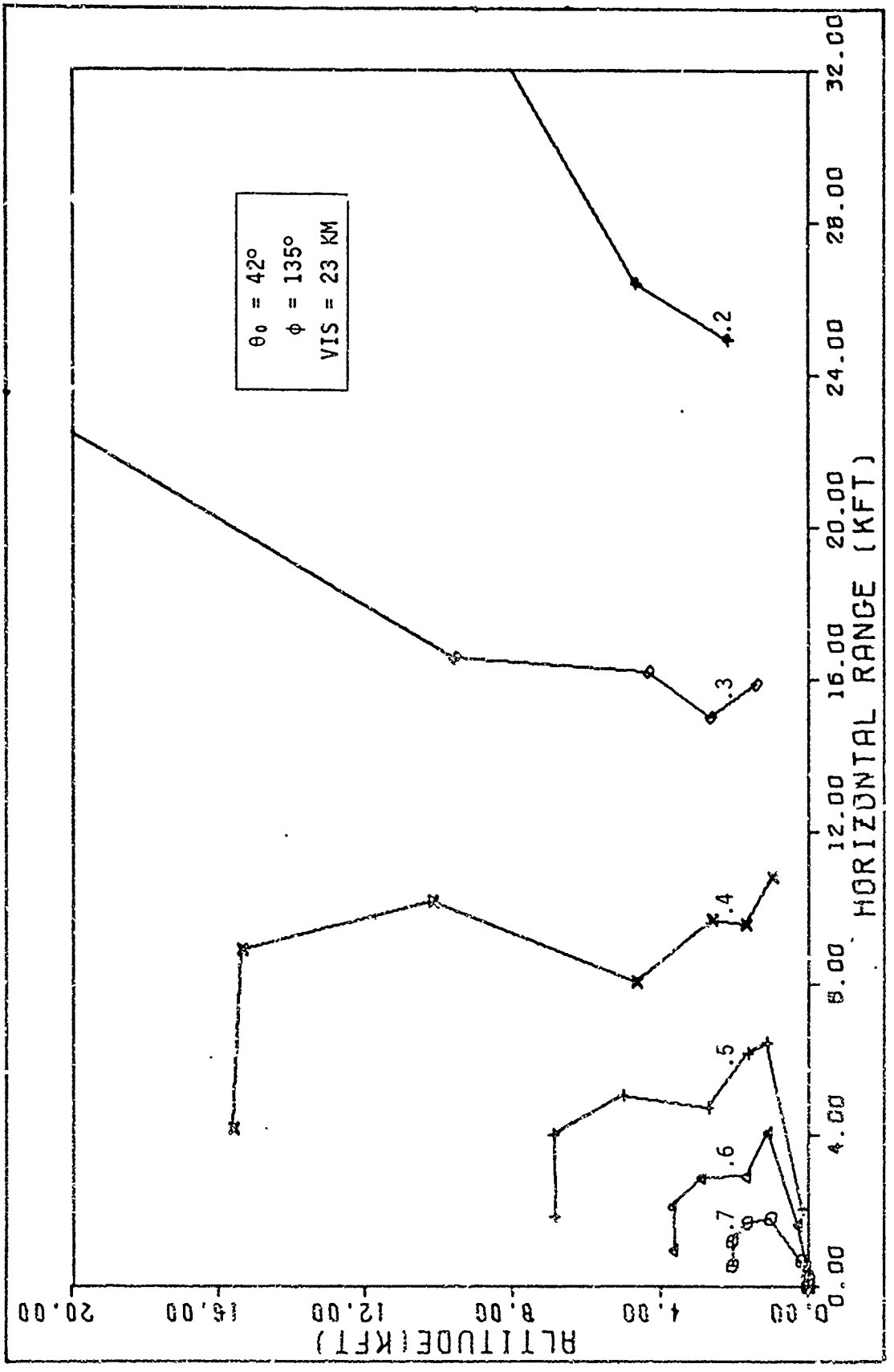

Fig. 43. Contours of Constant Contrast Transmission τ_c, for a Solar Zenith Angle of 42°, and an Azimuth of 135°. The Albedo is .06, and the Wavelength is .55 μm. R* Data is from AWS Model, bR_o Data is Measured Background Reflectance from Figs. 16 and 17.

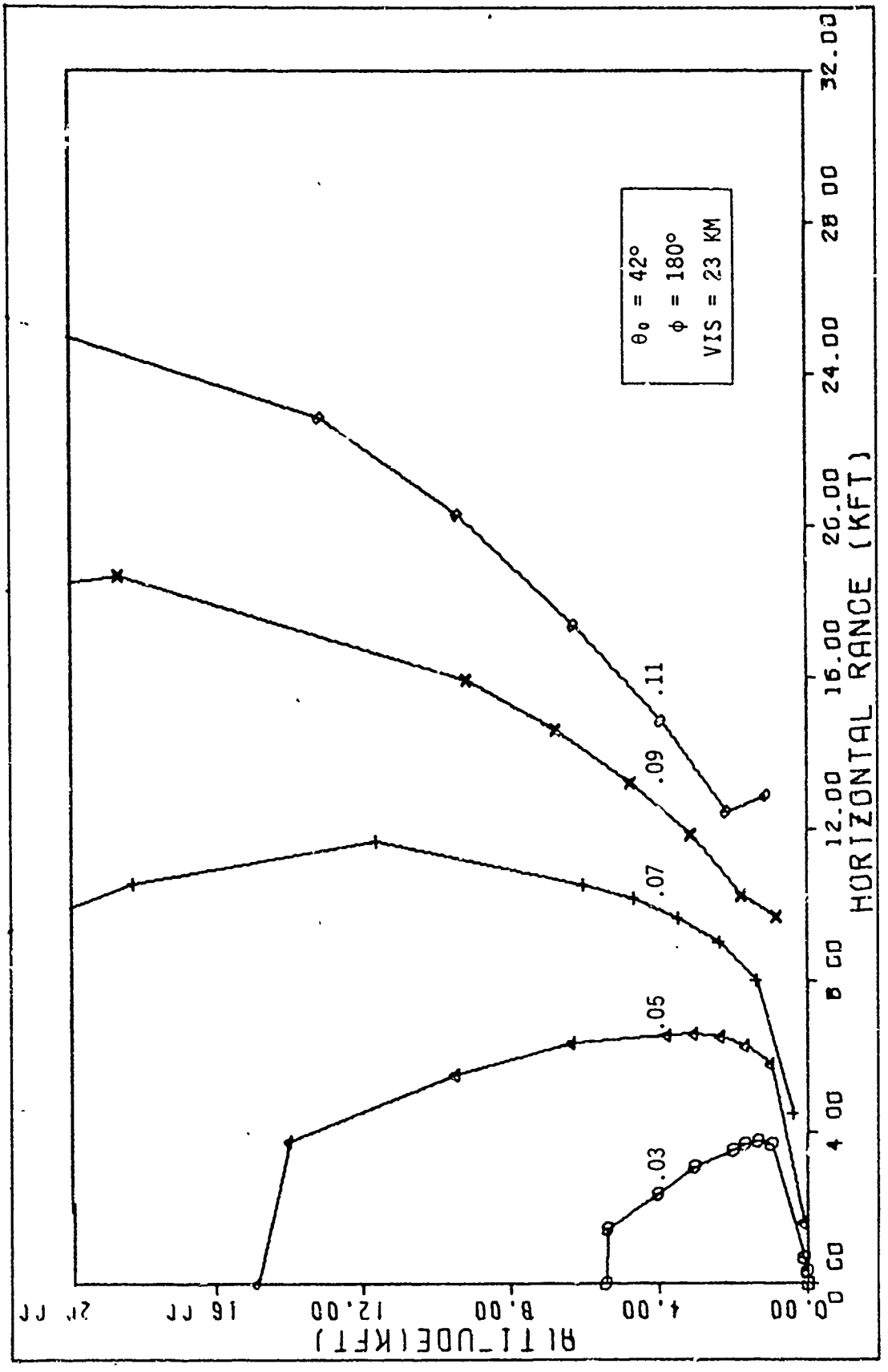

Fig. 44. Contours of Constant Directional Path Reflectance R* for a Solar Zenith Angle of 42° and an Azimuth of 180°. The Albedo is .06 and the Wavelength is .55 μm. Data from AWS Model.

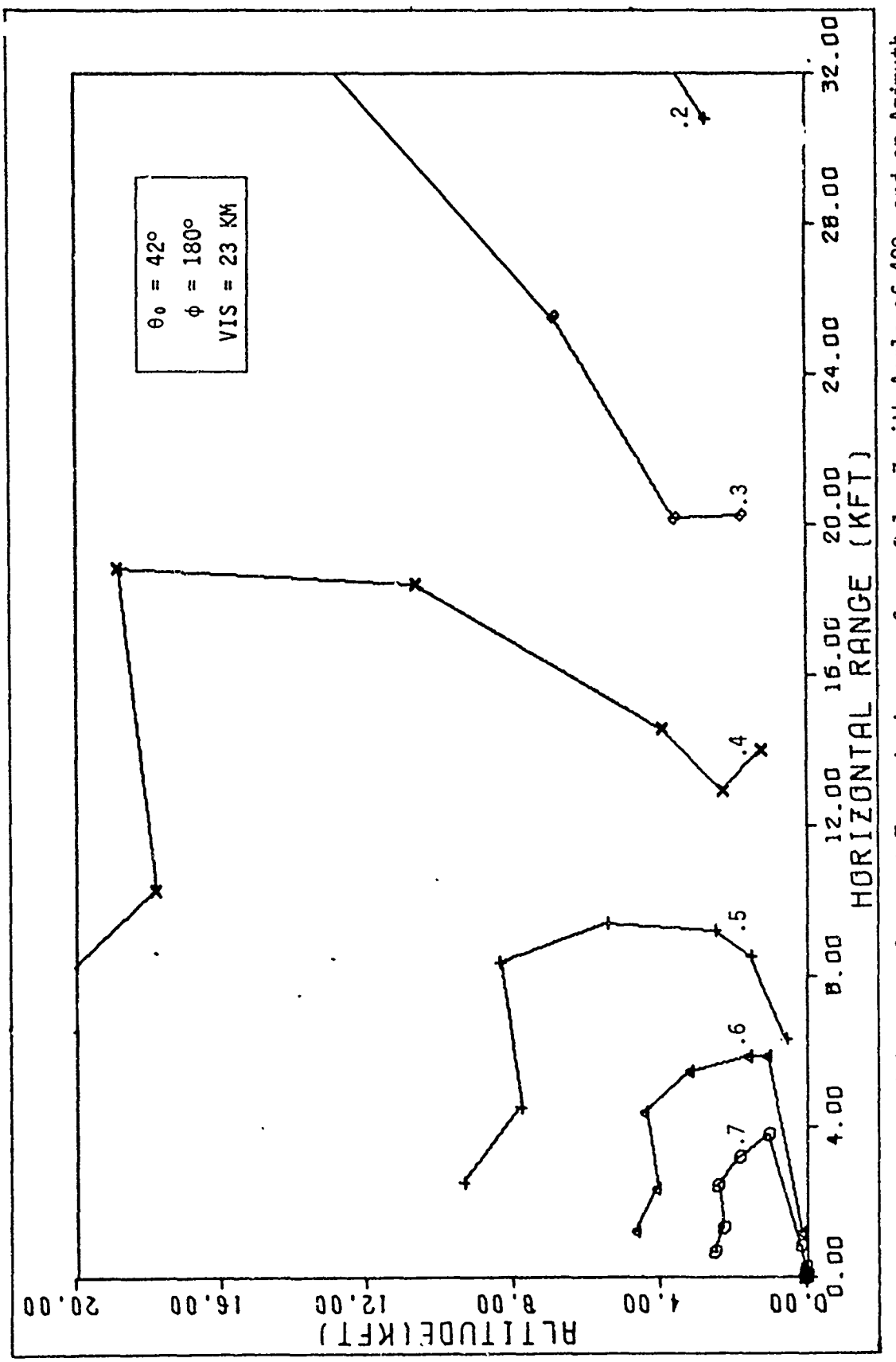

Fig. 45. Contours of Constant Contrast Transmission τ_C, for a Solar Zenith Angle of 42°, and an Azimuth of 180°. The Albedo is .06 and the Wavelength is .55 μm. R^* Data is from AWS Model, $_bR_o$ Data is Measured Background Reflectance from Figs. 16 and 17.

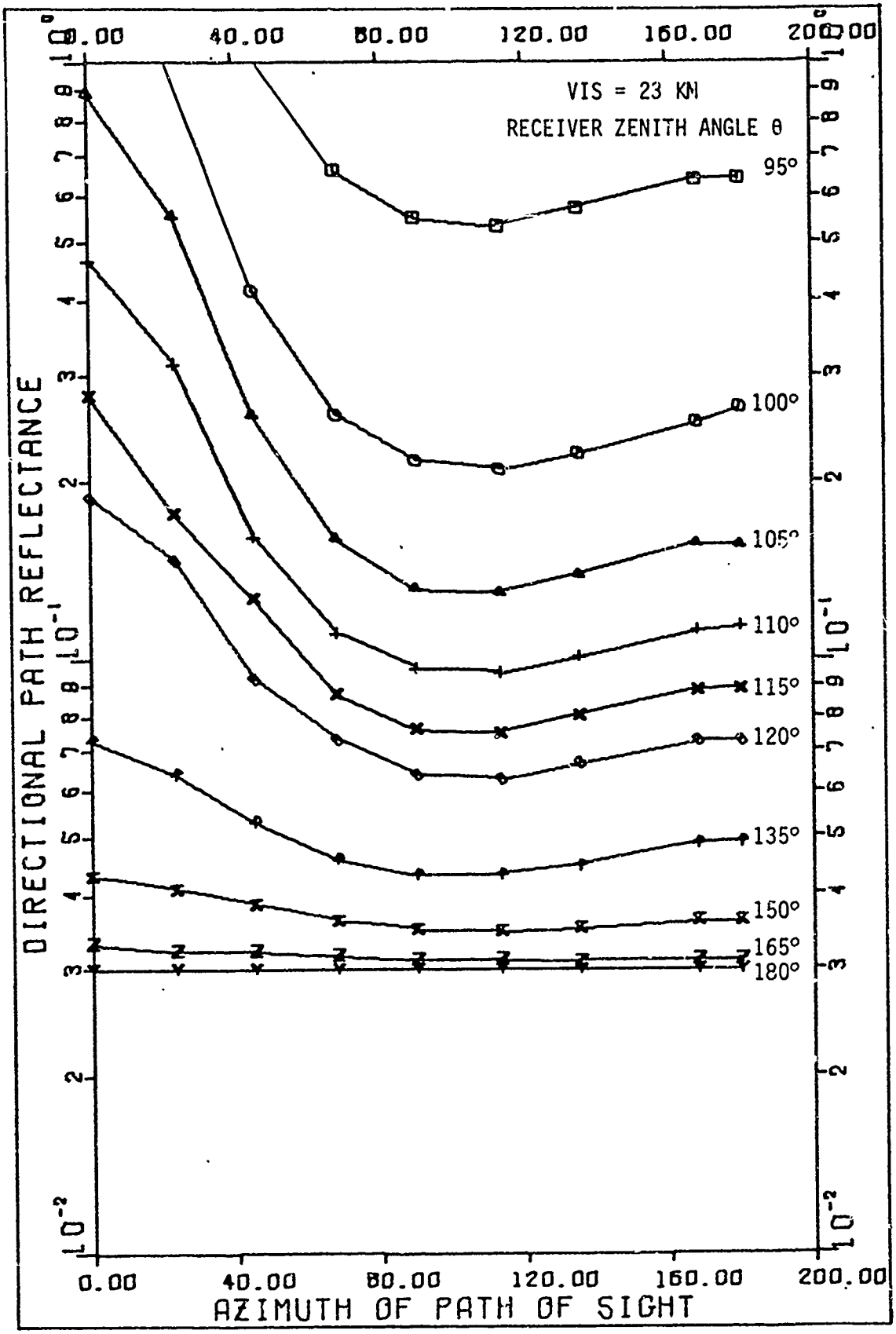

Fig. 46. Directional Path Reflectance Versus Azimuth for a Solar Zenith Angle of 78°. The Albedo is .06, Wavelength is .55 μm, and the Altitude is 2 KM. Data from AWS Model.

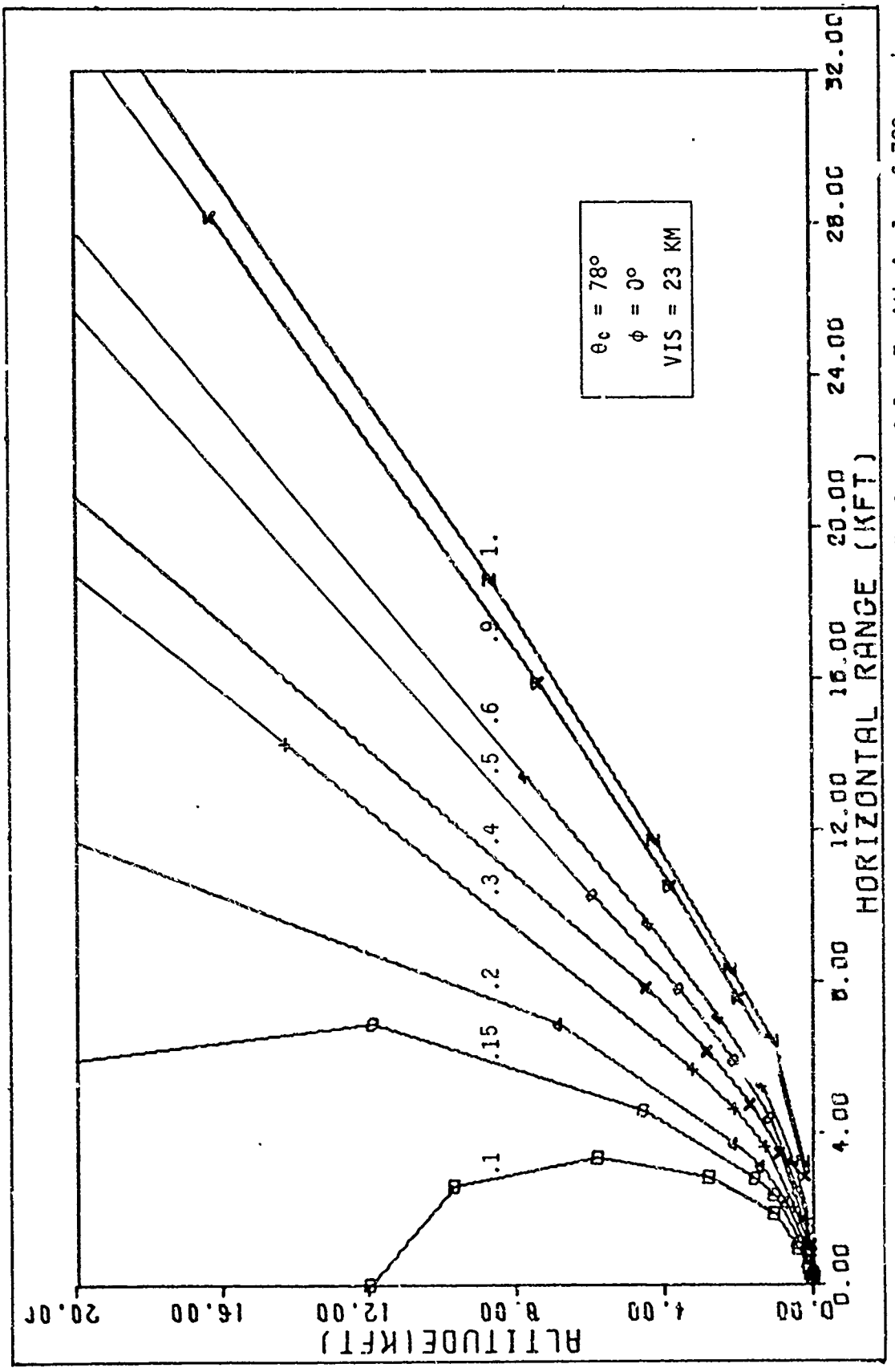

Fig. 47. Contours of Constant Directional Path Reflectance, R*, for a Solar Zenith Angle of 78°, and an Azimuth of 0°. The Albedo is .06 and the Wavelength is .55 μm. Data from AWS Model.

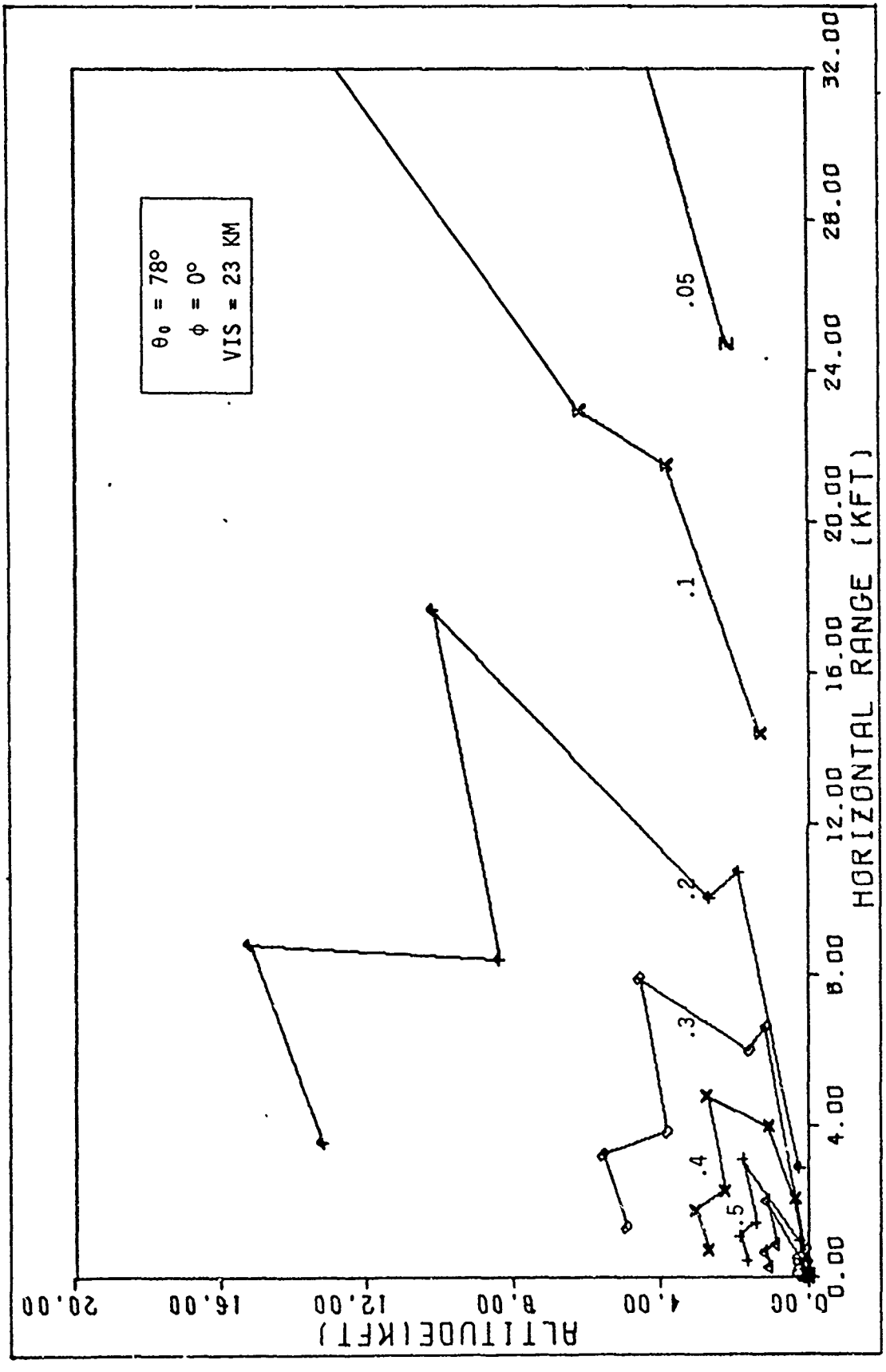

Fig. 48. Contours of Constant Contrast Transmission τ_C, for a Solar Zenith Angle of 78°, and an Azimuth of 0°. The Albedo is .06, and the Wavelength is .55 μm. R^* Data is from AWS Model, $_bR_o$ Data is Measured Background Reflectance (Ref 23:804).

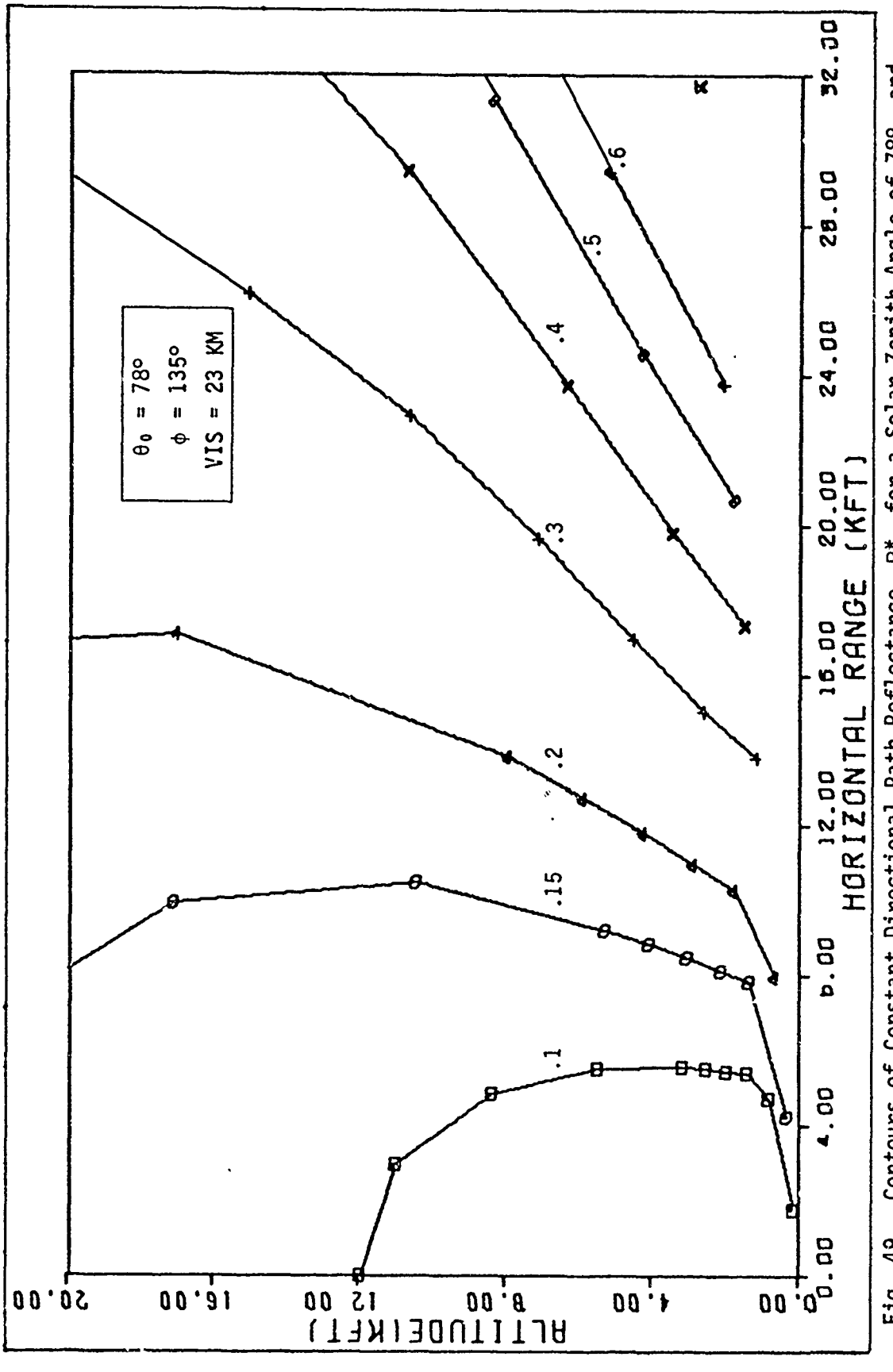

Fig. 49. Contours of Constant Directional Path Reflectance, R*, for a Solar Zenith Angle of 78°, and an Azimuth of 135°. The Albedo is .06 and the Wavelength is .55 μm. Data from AWS Model.

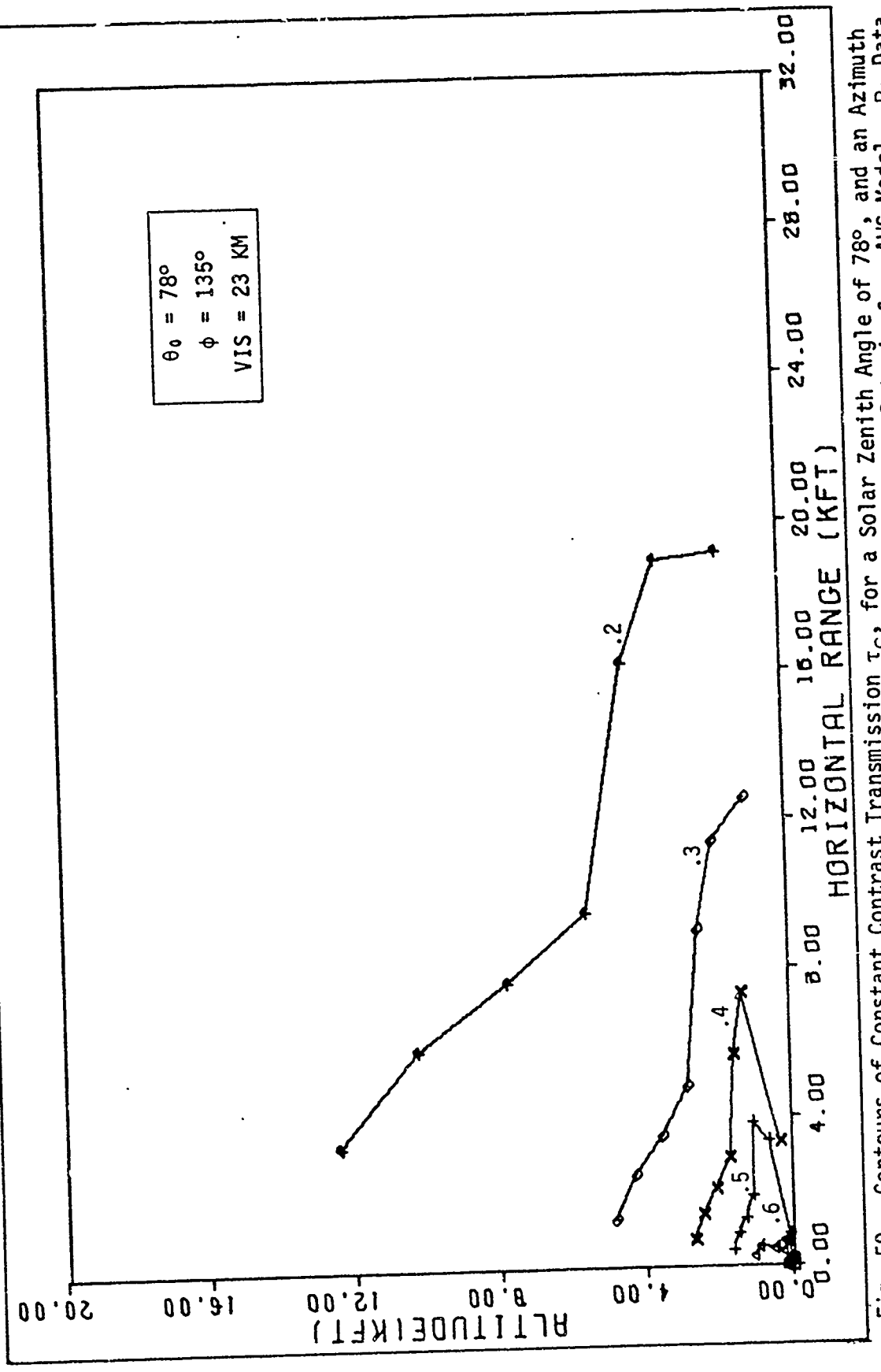

Fig. 50. Contours of Constant Contrast Transmission τ_C, for a Solar Zenith Angle of 78°, and an Azimuth of 135°. The Albedo is .06, and the Wavelength is .55 μm. R^* Data is from AWS Model, $_bR_o$ Data is Measured Background Reflectance (Ref 23:804).

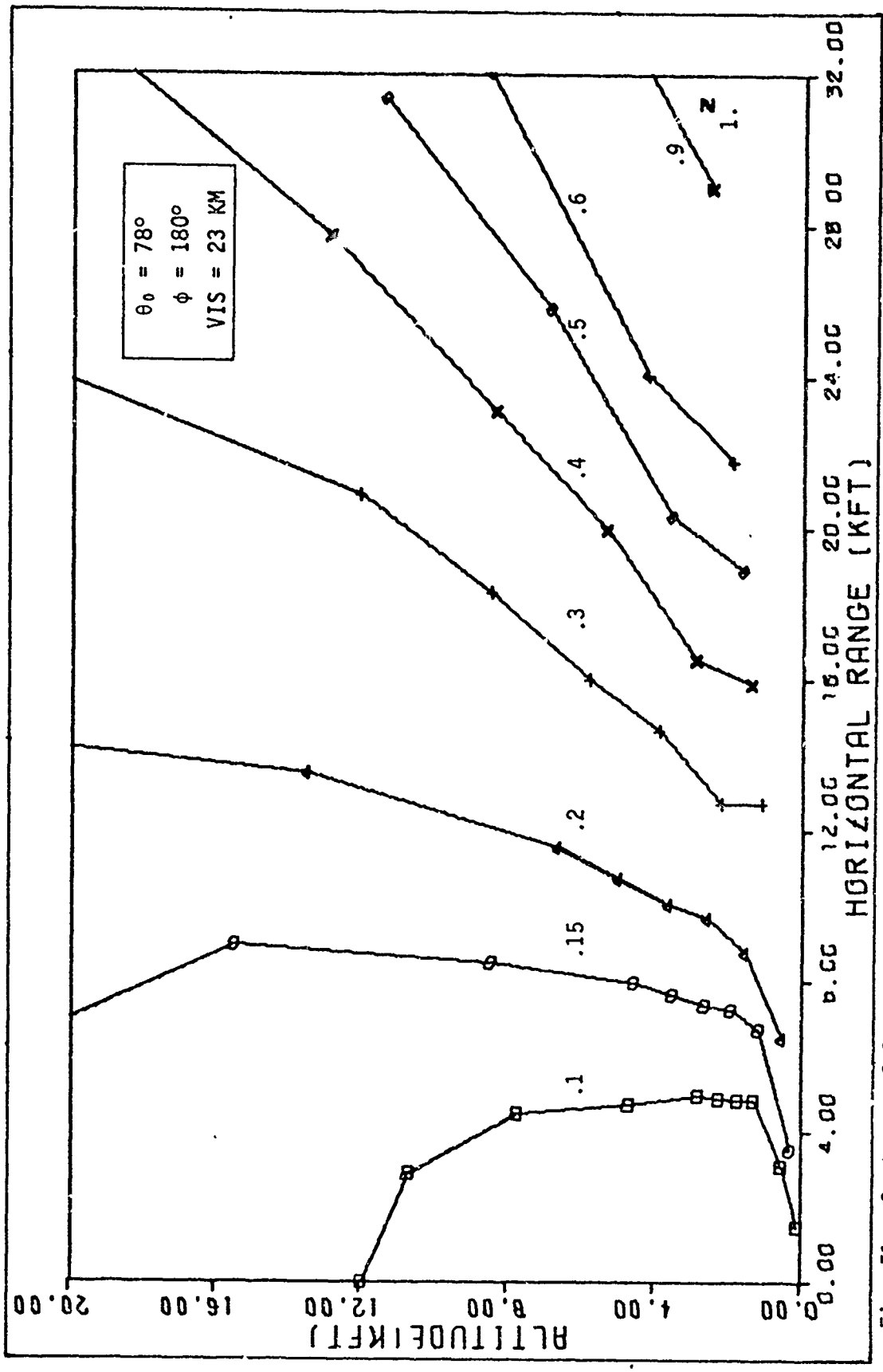

Fig. 51. Contours of Constant Directional Path Reflectance, R*, for a Solar Zenith Angle of 78°, and an Azimuth of 180°. The Albedo is .06 and the Wavelength is .55 μm. Data from AWS Model.

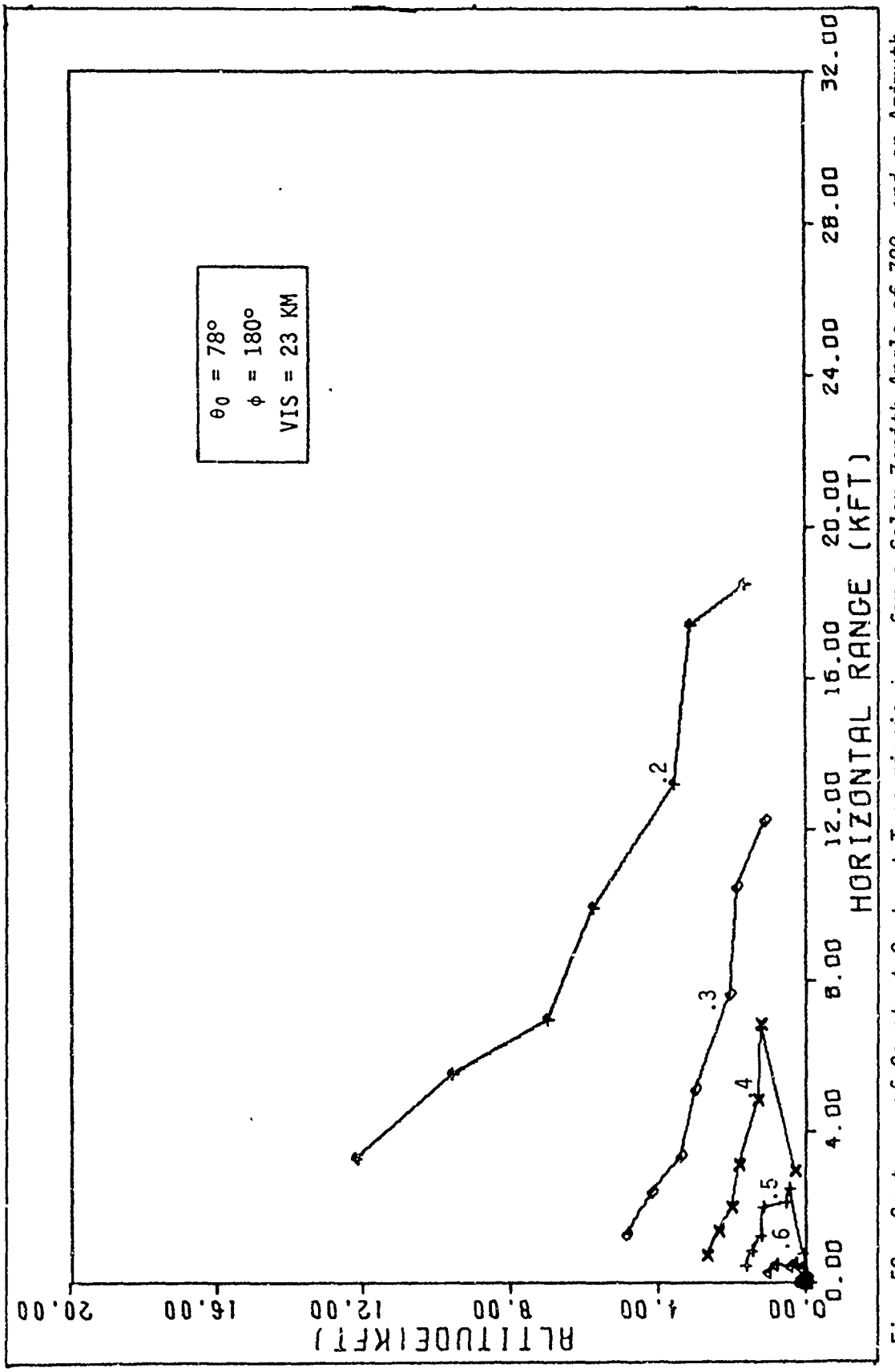

Fig. 52. Contours of Constant Contrast Transmission τ_C, for a Solar Zenith Angle of 78°, and an Azimuth of 180°. The Albedo is .06, and the Wavelength is .55 µm. R* Data is from AWS Model, $_bR_0$ Data. is Measured Background Reflectance (Ref 23:804).

VI. Inherent Contrast and Spectral Considerations

In this chapter some techniques for measuring the contrast between target and background will be discussed. Measurements made at Wright-Patterson AFB using a telephotometer and a teleradiometer will be presented. Measurements by photographic means will also be shown. The photographic technique proved to be quite convenient and gave comparable results to the telephotometer. The photographic technique was recommended for use in the recent adverse weather tests of the Maverick missile in Europe and provided much useful data on the inherent contrast of military vehicles. Some sample data is presented. Attempts to measure sky-ground ratio by the technique suggested by Duntley using a telephotometer, and photographic means are presented and compared with data computed from contrasts measured at the target and at a slant range of 3000 feet.

Telephotometer Measurements

A Gamma Scientific photometer-monochromator with telescopic attachment was used. The photometer has a photopic response. An aperture of 6 minutes of arc was used for all measurements. The distance from the target and background was approximately 200 feet. The area subtended with the measurement aperture was approximately .35 feet. A 2-1/2 ton Army olive-drab truck was measured during seven separate time periods between 19 and 27 October 1971. The time periods corresponded to preliminary adverse weather flight tests being conducted by the Maverick Missile System Program Office. The position of the target and the photometer is shown in Fig. 53. Measurements were conducted both from the ground (Fig. 53a) and with the photometer mounted on a platform 28 feet in the air (Fig. 53b)

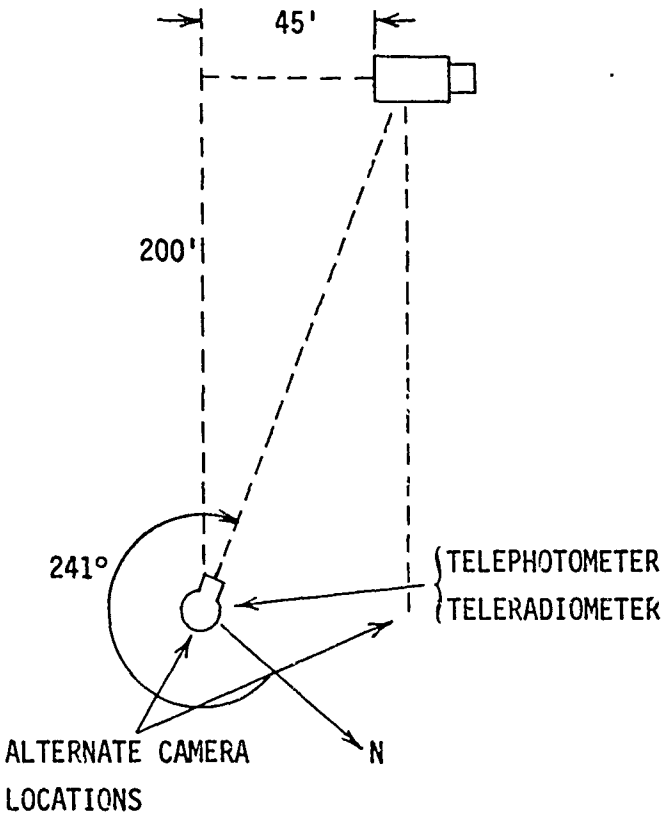

Fig. 53a. Horizontal Plane View

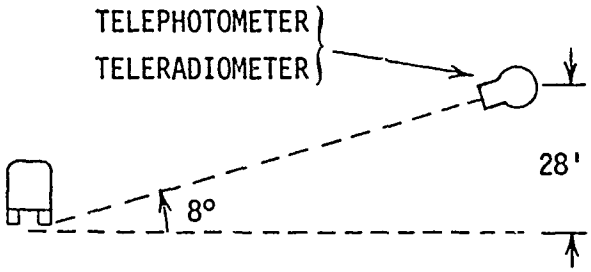

Fig. 53b. Vertical Plane View

Fig. 53. Schematic Showing the Positions of Camera and Photometer-Radiometer During Inherent Contrast Measurements

to approximate an 8° look-down angle, the approximate dive angle of the aircraft.

The reflected radiance in foot-lamberts was read from the background near the truck, and from two areas of the truck: the canvas cover, and the cab. Scans of different areas of the truck indicated that it was very uniform in reflected radiance, so this procedure was thought to be representative. The background was green grass, about 6 inches high and usually wet with dew. Contrast was calculated by averaging the canvas and cab reading as the target signal and using Eq (9).

The results of the measurements are shown in Table XII. The several sets of contrast measurements during a particular time period are averaged and data measured photographically is also presented.

Photographic Measurements

Photographs of the target-background scene were taken during the same time periods as the telephotometer measurements. A Honeywell Pentax camera with an $f/1.4$ 50-mm focal length, Takumar lens was used. Plus X film was used with a Kodak Wratten 102 filter. The Wratten 102 filter is used to correct the response of the film to a photopic or near photopic response.

The camera was located on the ground as shown in Fig. 53a. The film data was reduced in the following way: Prior to film development, a standard neutral density step wedge was exposed on the film end as a check on the development process and for calibration purposes. The step-wedge has twenty-one density steps. The film is then developed to a gamma of approximately 1. and the neutral density step wedge scanned with a densitometer to provide a D-log E curve, where D is the density, and log E is the relative log of the exposure. A sample curve is shown in Fig. 54. Although one can

TABLE XII

Comparison of Inherent Contrast Measurements

Date, Time (EDT)	Solar Zenith	Azimuth From Sun	Receiver Zenith	Weather Visibility	Inherent Contrast		
					Photometer	Photograph	Monochromator Computed
19 Oct 71							
1340-1415	49°-51°	67°-50°	90°	Clear 5H	-.84 (1)		
20 Oct 71							
0915-0940	77°-74°	126°-122°	90°	Clear 7	-.71 (2)		
21 Oct 71							
0900-0945	78°-63°	127°-120°	90°	Overcast 7	-.72 (5)		
21 Oct 71							
1305-1355	50°	70°-50°	90°	Overcast 7-10	-.70 (8)	-.69 (13)	
1415-1420	52°	43°	98°	Overcast 10	-.74 (1)		
26 Oct 71							
1020-1120	65°-57°	115°-100°	90°	Overcast to	-.75 (8)	-.66 (7)	
1130-1200	55°-53°	98°-85°	98°	broken 2-4	-.72 (1)		-.66 (1)
26 Oct 71							
1400-1445	50°-55°	51°-31°	90°	Broken 4-5	-.73 (6)	-.62 (15)	
1455-1530	55°-58°	31°-23°	98°	Broken 4	-.71 (1)		-.66 (1)
27 Oct 71							
0912-1008	78°-67°	120°-113°	90°	Clear 3-4H	-.76 (8)	-.73 (11)	
1020-1050	65°-60°	110°-103°	98°	Clear 4-5H	-.78 (1)		-.89 (1)

Note: Visibilities are in miles
Numbers in parentheses are the number of samples averaged
H indicates haze obstructing visibility
Negative sign on contrast indicates target darker than background

actually determine absolute log E from the source used for the calibration exposure, this is not necessary for the computation of contrast. If one wants the absolute radiance or luminance of the target or background, the absolute log E must be used. An authoritative treatment of the photographic process is given by Mees (Ref 27:Chaps. 5, 19, 20).

The negative of the target-background scene is measured to yield the density of the target and background. The truck image size was about 5 mm. The aperture on the Macbeth densitometer was .5 mm. As with the photometer, an area of the canvas and an area of the cab of the truck were measured. Also an area of the background near the truck was measured. The D-log E curve was then used to convert the neutral density to relative log exposure values. After taking anti-logs to yield relative exposure, the canvas and cab readings from the truck were averaged and contrast computed, using Eq (9).

Averaged values of inherent contrast are presented in Table XII with the telephotometer readings for comparison. In addition, the sun position and sky conditions under which the measurements were taken are listed. The sun position data was computed from a subprogram of the Aerial Photographic Energy Model (Ref 15). The visibility is the estimated visibility in the direction of measurement. The number of data points averaged is also shown.

Radiometric Measurements

The Gamma Scientific photometer had a monochromator attachment which allowed measurement over discrete wavelength intervals of width approximately 20 Å. Measurements were made from the platform as shown in Fig. 53b of the truck and the background. The wavelength intervals covered were from .45 μm to .75 μm. The canvas and cab were measured with the same aperture used for the telephotometer measurements. The results for one set of measurements are

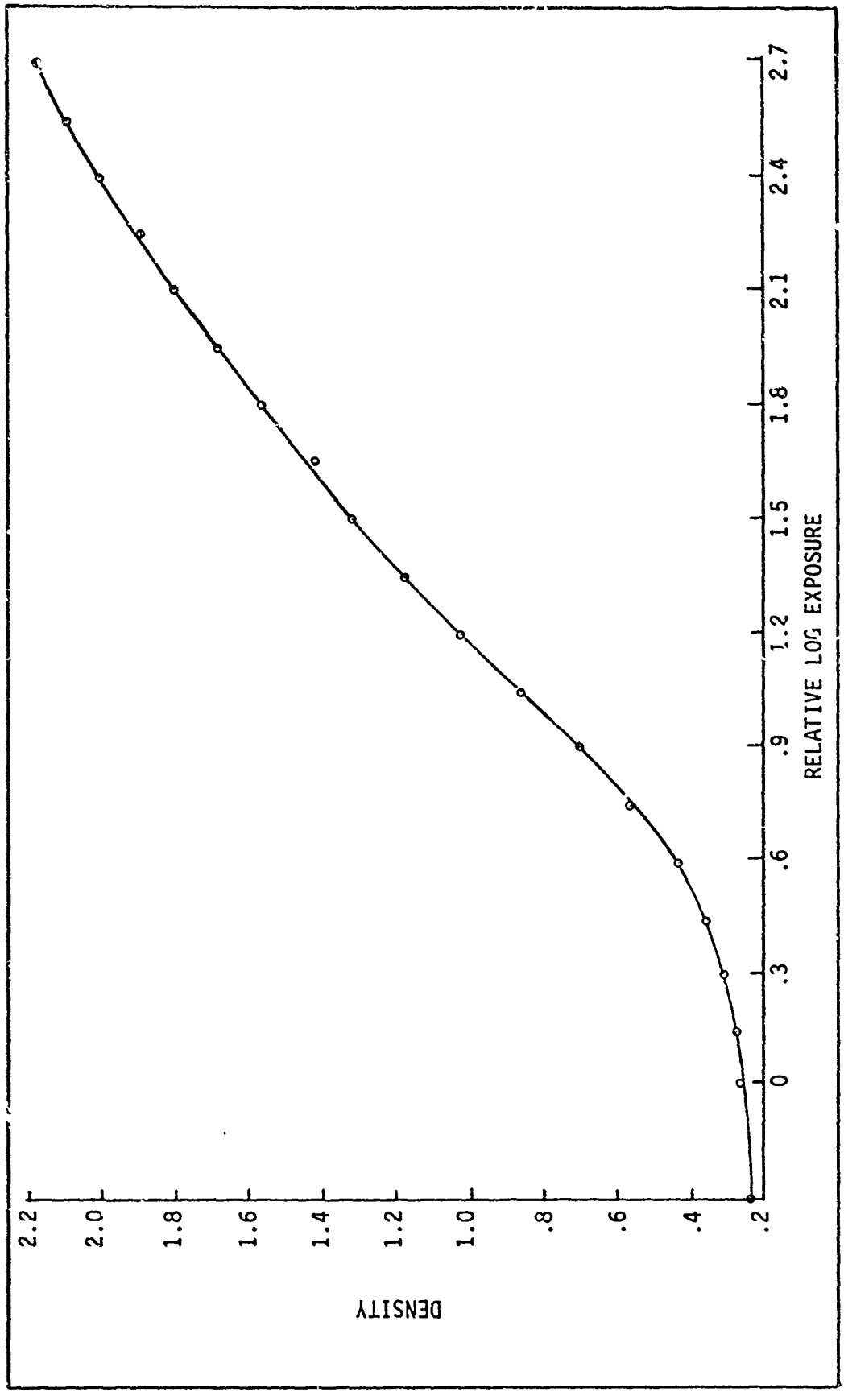

Fig. 54. D-log E Curve for Kodak Plus-X Film with Wratten 102 Filter During Flight AW-4, 23 October 1971. Camera had 1000 mm Lens Located 3000 Feet from Target.

shown in Fig. 55. The reflected spectral radiances are presented in arbitrary units since no calibrated source of known radiance was available. However, for contrast measurements only relative values are required. The data has been corrected for the response of the S-20 phototube which was used in the system based on manufacturer-supplied data. The contrast can then be computed from Eq (9) where the relative target and background reflected radiances are computed as follows:

$$N_0(Z_+,\theta,\phi) = \int_{\lambda=.45\mu m}^{\lambda=.75\mu m} N_e(Z_+,\lambda,\theta,\phi)S(\lambda)d\lambda \qquad (76)$$

where $N_0(Z_+,\theta,\phi)$ is the inherent relative reflected radiance in the range .45 - .75 um; $N_0(Z_+,\lambda,\theta,\phi)$ is the spectral reflected radiance as a function of wavelength λ; and $S(\lambda)$ is the response of the system "seeing" the radiation as a function of wavelength, λ.

If the relative response of the eye is used for $S(\lambda)$, then the integration carried out, the result is the relative reflected radiance available to the eye. The photopic contrast can then be computed. This was done using Simpson's Rule integration and data for three sets of measurements. The results are shown in Table XII for comparison with the photometer and photographic data. Figure 56 shows the relative radiances available in the photopic region. The response function for the eye was taken from Brown (Ref 28:223).

It can be noted from Table XII that all contrasts were negative indicating that in all cases the background was brighter than the target. This is as anticipated since grass is normally expected to have a reflectance of 10 to 15%, and olive-drab canvas or paint about 5 to 10%. The agreement in the photometric measurements between the ground and platform measurements is good, indicating that the inherent contrast does not change

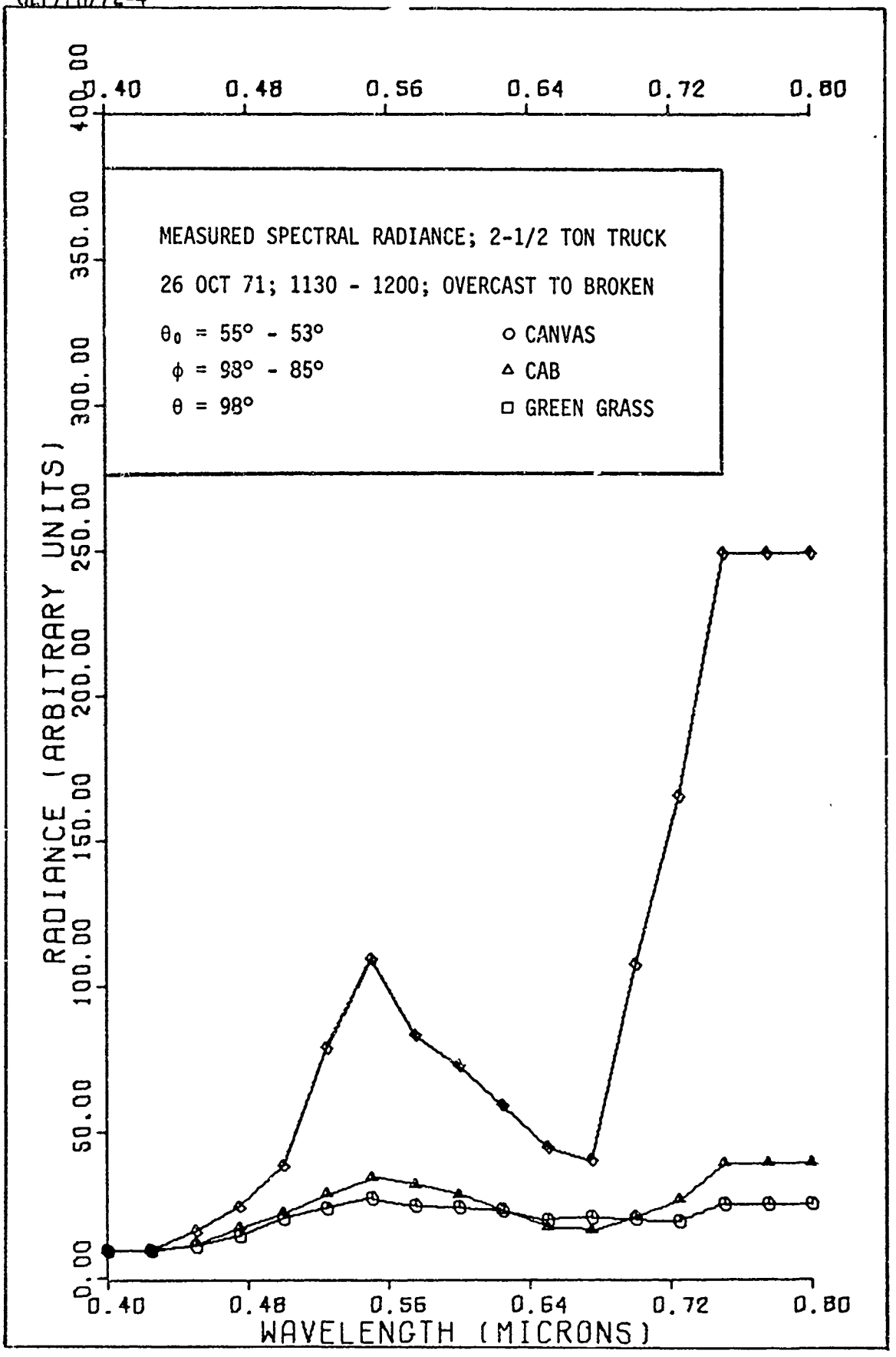

Fig. 55. Measured Spectral Radiance for Truck Against Grass Background in Arbitrary Units

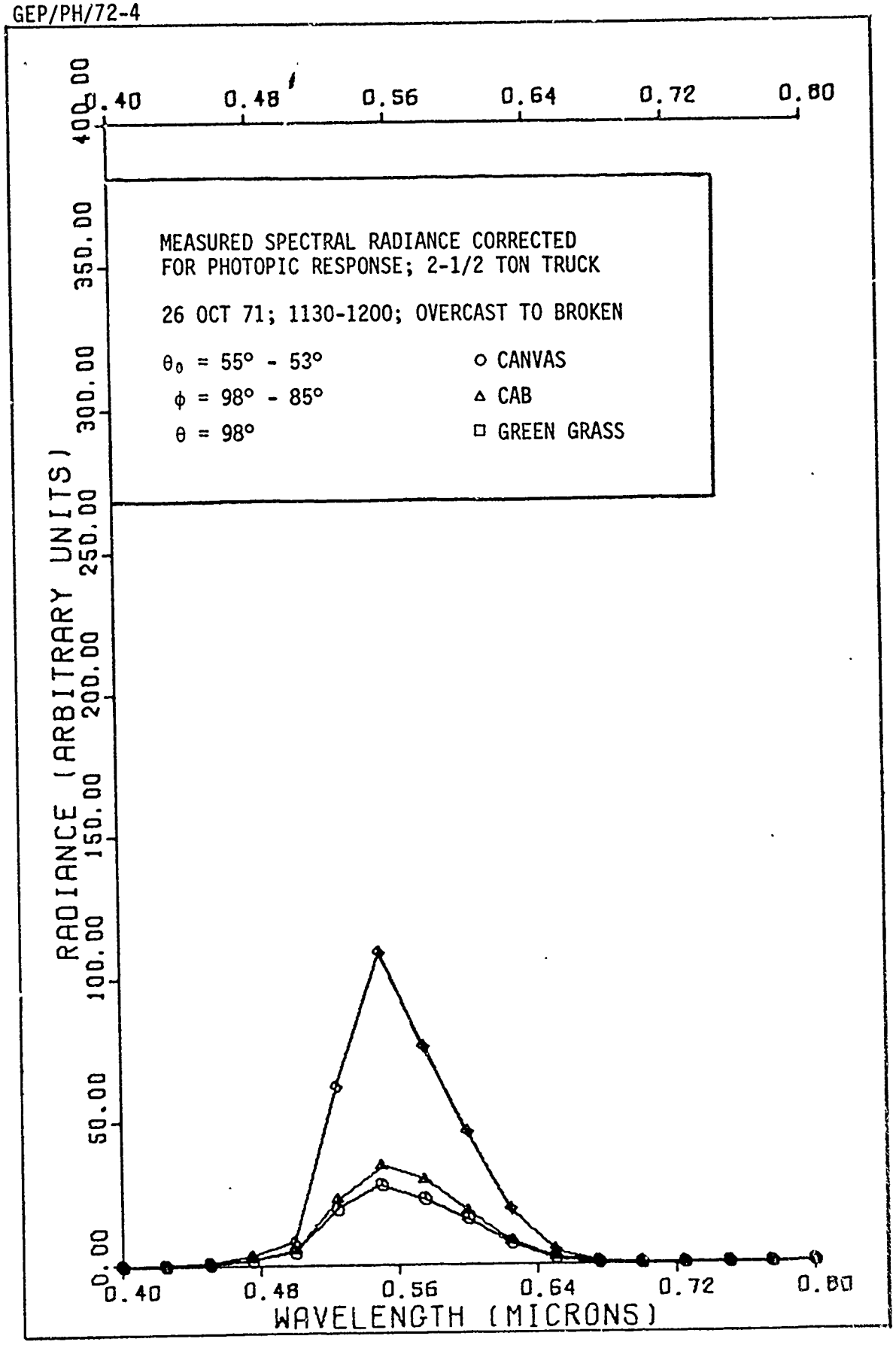

Fig. 56. Measured Spectral Radiance for Truck Against Grass Background. Data Corrected for Photopic Response

sharply with small angular changes. Thus contrast taken from the ground may be used reasonably for low dive angles as long as pronounced shadowing is not occuring. Comparison between the photometer and photographic data shows the latter to be lower but comparable to the photometer data, supporting the idea that photographs may be reasonably used in the field environment to yield inherent contrast. The technique used here was rather simple since only two density readings were made on the target and one on the background. This is justified if the target and background are relatively uniform as was the case here. However, more complex targets or backgrounds should be carefully evaluated using a microdensitometer to determine whether the simple technique used above or a microdensitometer should be used. Figure 57 shows two scans made by a Joyce-Loebel microdensitometer from one of the frames. An aperture of 25 μm by 615 μm was used. The large density change between target and grass background can be clearly seen. But note also the relatively smooth density readings from the canvas near the top of the truck (Figure 57a), but the more irregular readings near the bottom (Figure 57b).

Figures 58 and 59 show microdensitometer maps of a 2-1/2 ton truck and a Chapparal weapons carrier. They were generated by computer from negatives using the same camera and film as above. These were taken in Germany during the recent adverse weather tests of the Maverick missile. Only the target vehicle and the surface background are displayed, the relative density values being indicated by the darkness or lightness of the areas. Note the uniformity of the truck with certain darker shadows near the wheels, while the Chapparal weapons carrier is much less distinct and blends with the background. Note also that this is a "positive" while the densities shown in Figs. 57a and 57b are "negatives." To get

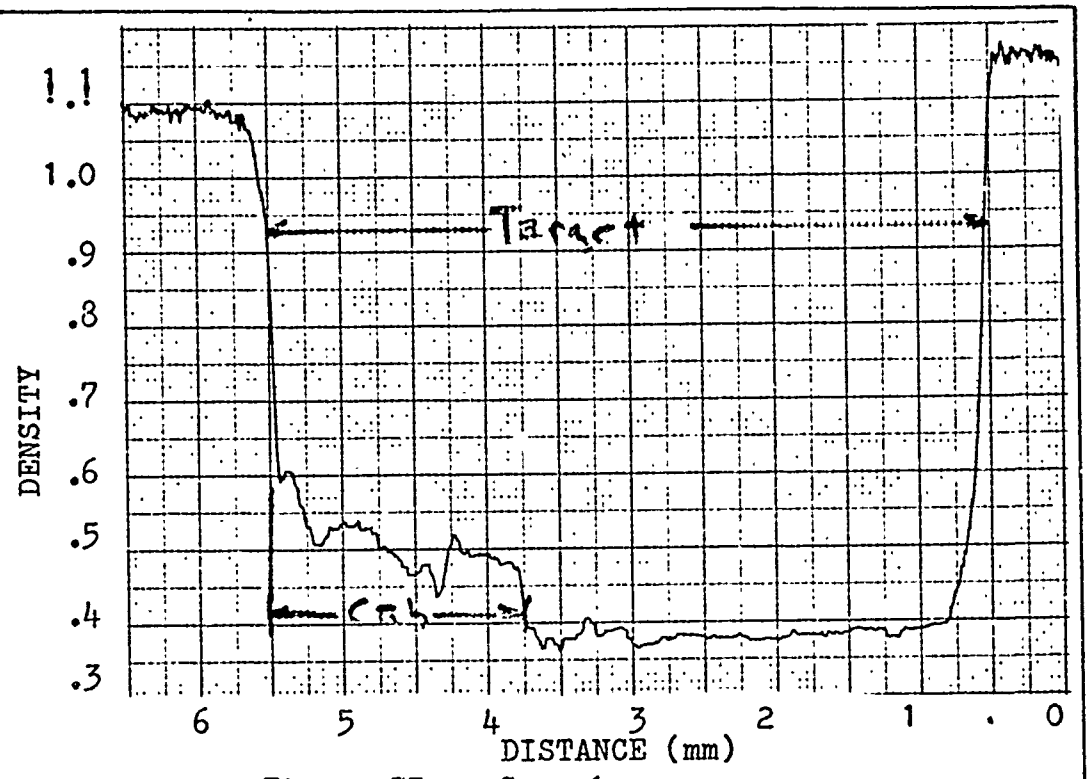

Figure 57a. Scan 1

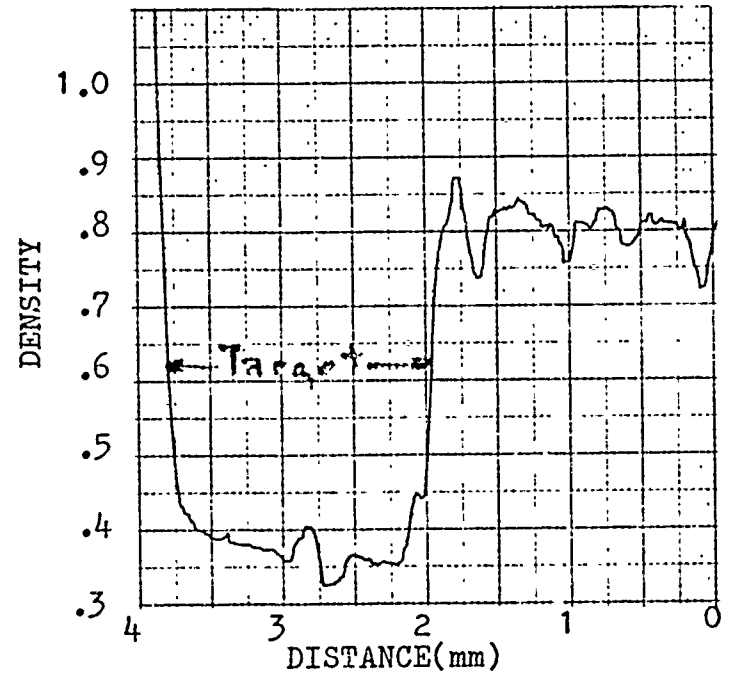

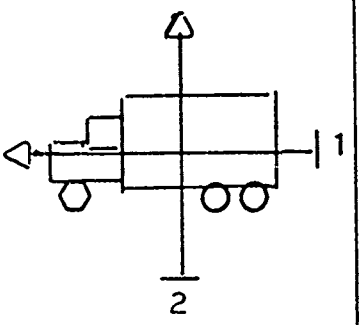

Figure 57b. Scan2

Figure 57. Two scans of an Army olive-drab 2-½ ton truck using a Joyce Loebl microdensitometer. The backgrond is green grass. Data taken during Flight AW-6, 26 Oct 71.

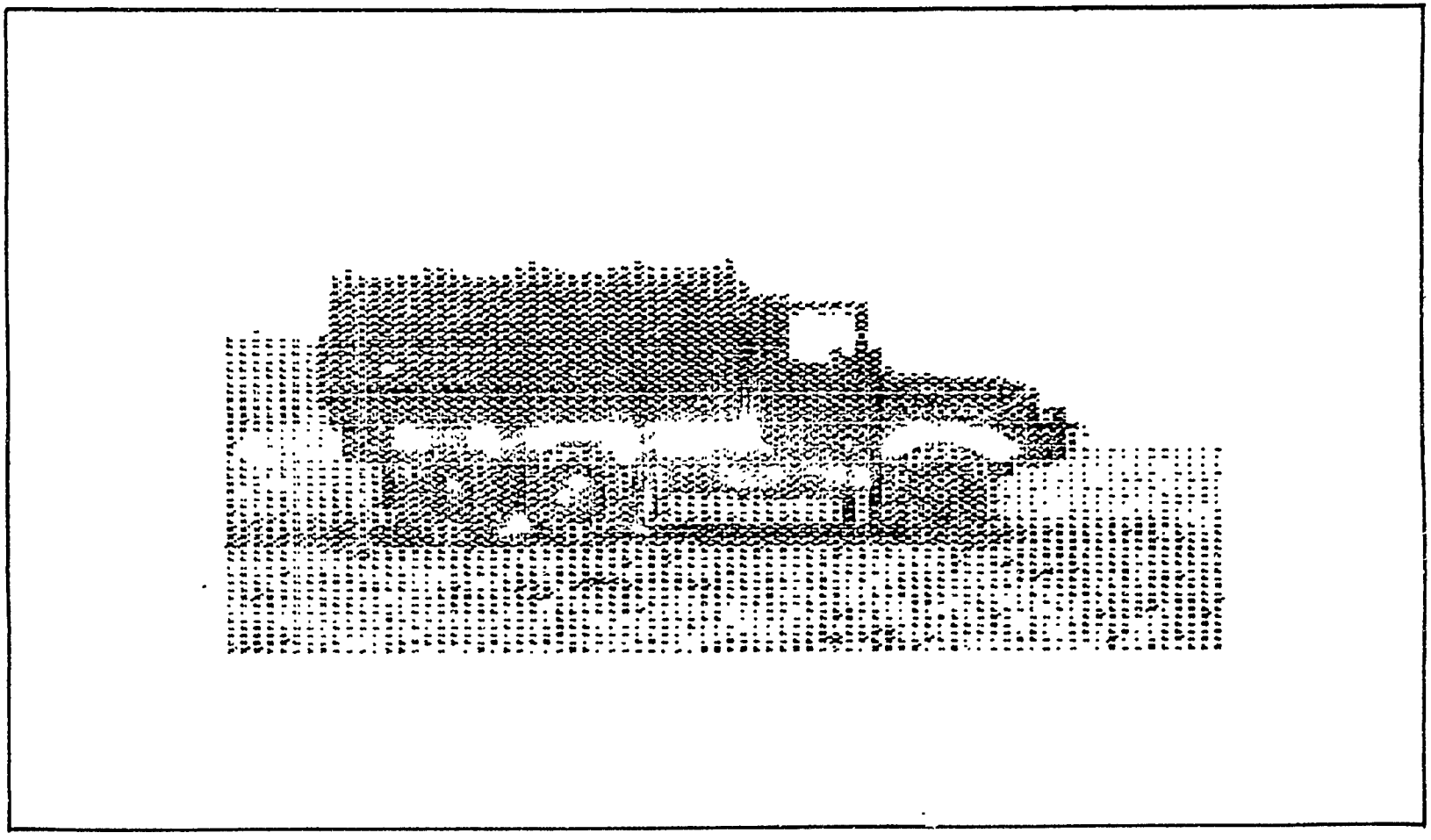

Fig. 58. Computer Generated Picture of 2-1/2 Ton Truck Used During Maverick Adverse Weather Tests in Germany. (A photographic negative was scanned by a Mann microdensitometer to determine the density of the target and background. The sampling slit was 24 × 60 μm. Data was sampled every 300 μm horizontally and every 180 μm vertically. The number of dots in each small square is representative of the reflective properties of the area. The more dots, less the reflectivity.)

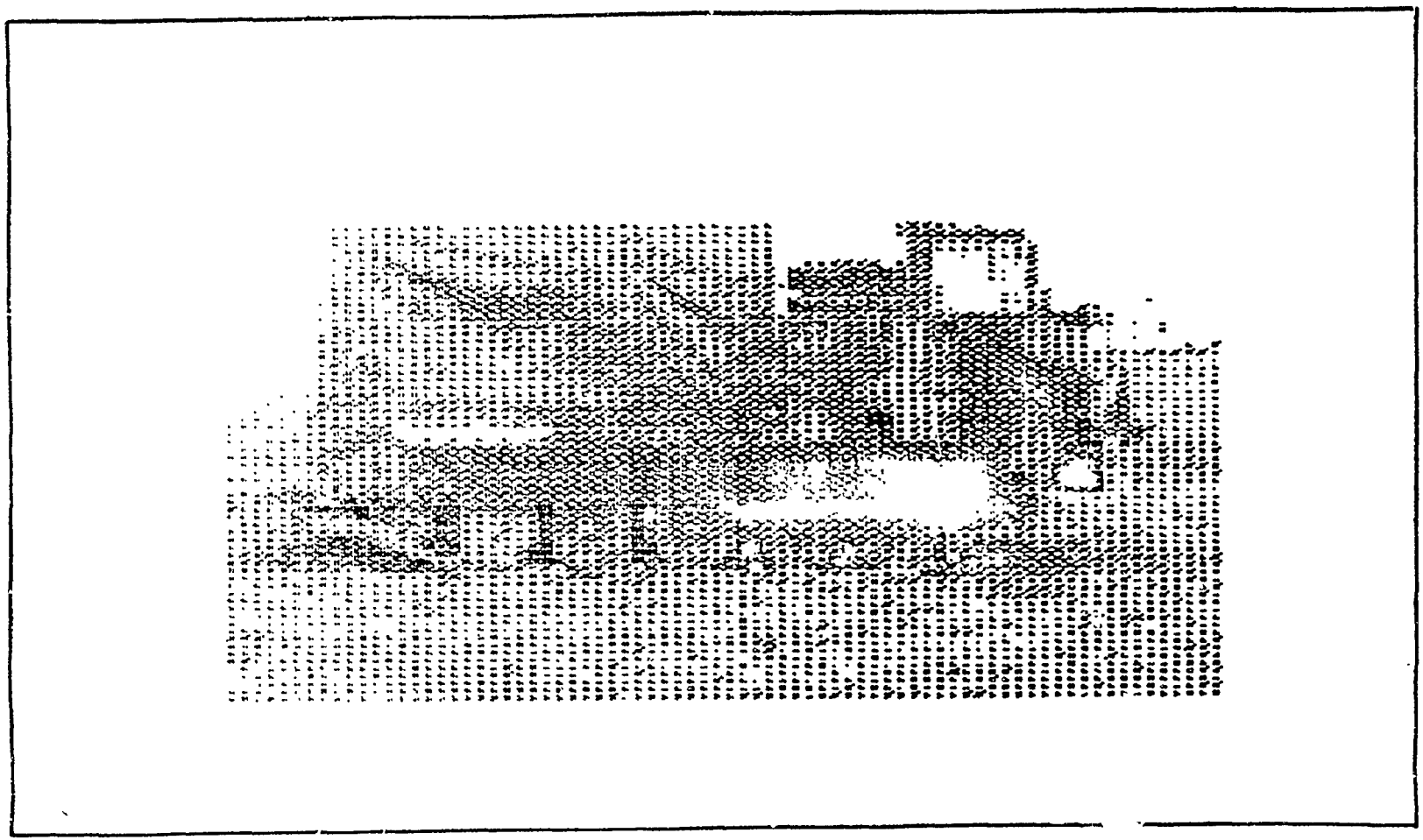

Fig. 59. Computer Generated Picture of Chapparal Weapons Carrier Used D[illegible]v[illegible]ck Adverse Weather Testing in Germany. (Picture was generated by the same techn[illegible]58. Note the lower contrast presented by this target in comparison to the 2-1/2 [illegible]ote also the very bright strip and the dark areas between the treads.)

meaningful inherent contrasts on the Chaparral it might be necessary to go to the microdensitometer technique. Inherent contrasts achieved in Europe during the Maverick tests will be reported in a Flight Test report to be published by the Maverick System Program Office.

Spectral Considerations

Throughout the report, the fact that the radiometric and atmospheric quantities are spectral in nature has been mentioned, but ·hing has been done further than to assume that a wavelength of .55 μm ·esentative of the photopic region and state that this is the area o ·ern. For an electro-optical sensor, this is not always the case. If, for example, the measured spectral radiancesfrom the truck and background presented in Fig. 55 are integrated over wavelength using the spectral response of the vidicon, Fig. 61 results. The response function for the vidicon was taken from a Hughes technical report with the vidicon corrected by a yellow haze filter. The response function of the vidicon is shown in Fig. 60. From Fig. 61 it can be seen that the vidicon sees more contrast in the red end of the spectrum, having sensitivity into the near IR. ·e inherent contrast was computed for the three data sets from Table XII where radiometric measurements were available. The integration was carried out from .45 μm to .75 μm using the measured data, and the data at the end points was then extrapolated to .4 μm and .8 μm as shown in Fig. 55. The integration was then carried out from .4 μm to .8 μm. The results are presented in Table XIII. Note from the table that more contrast exists for the vidicon than for the eye and that integration to longer wavelengths is helpful for improving the contrast available. From the response curve for the vidicon, integration to about .85 μm would be justified and would probably show that even more inherent contrast is available to the vidicon than to the eye

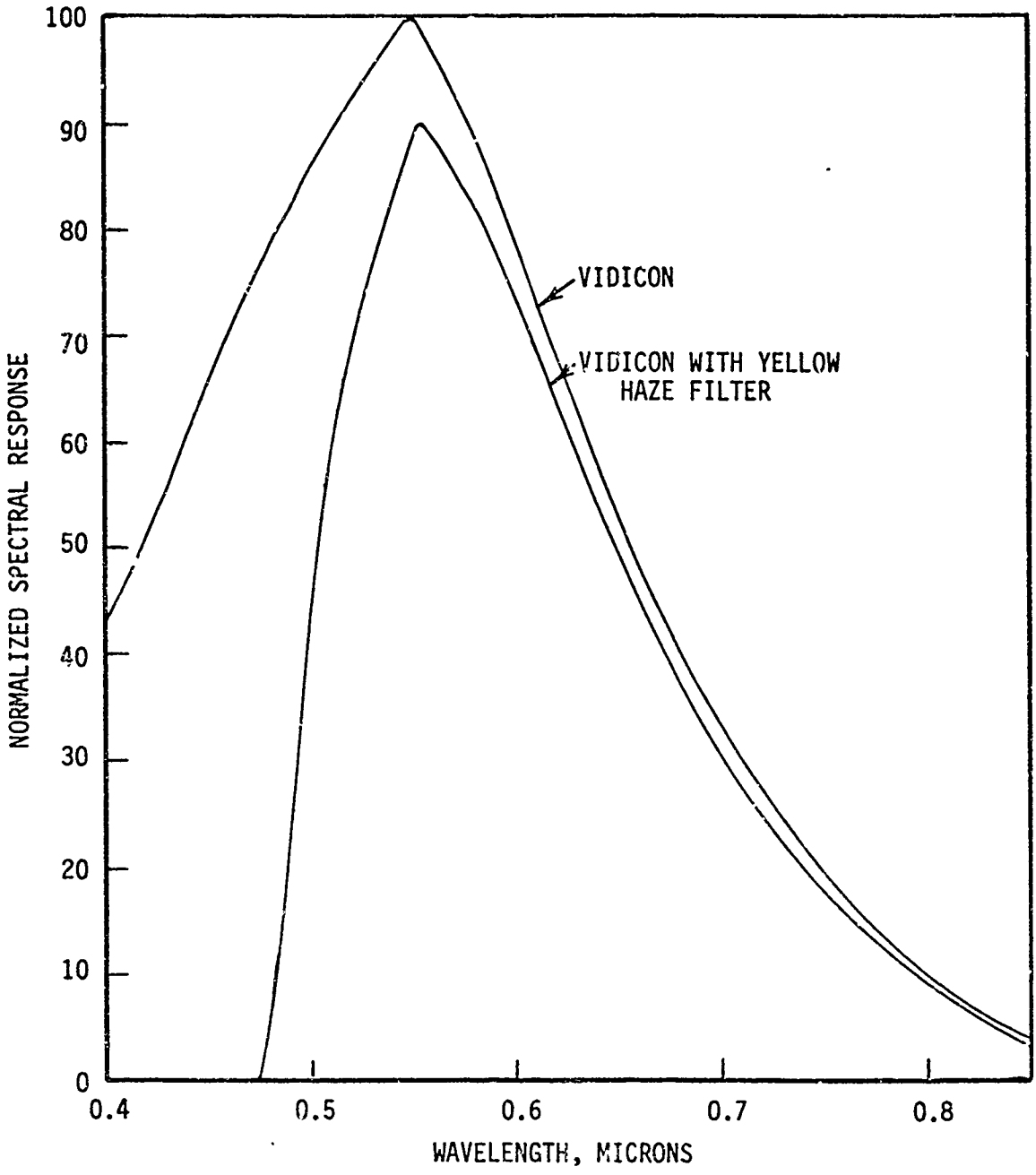

Fig. 60. Relative Spectral Response of Maverick Vidicon And With Yellow Haze Filter

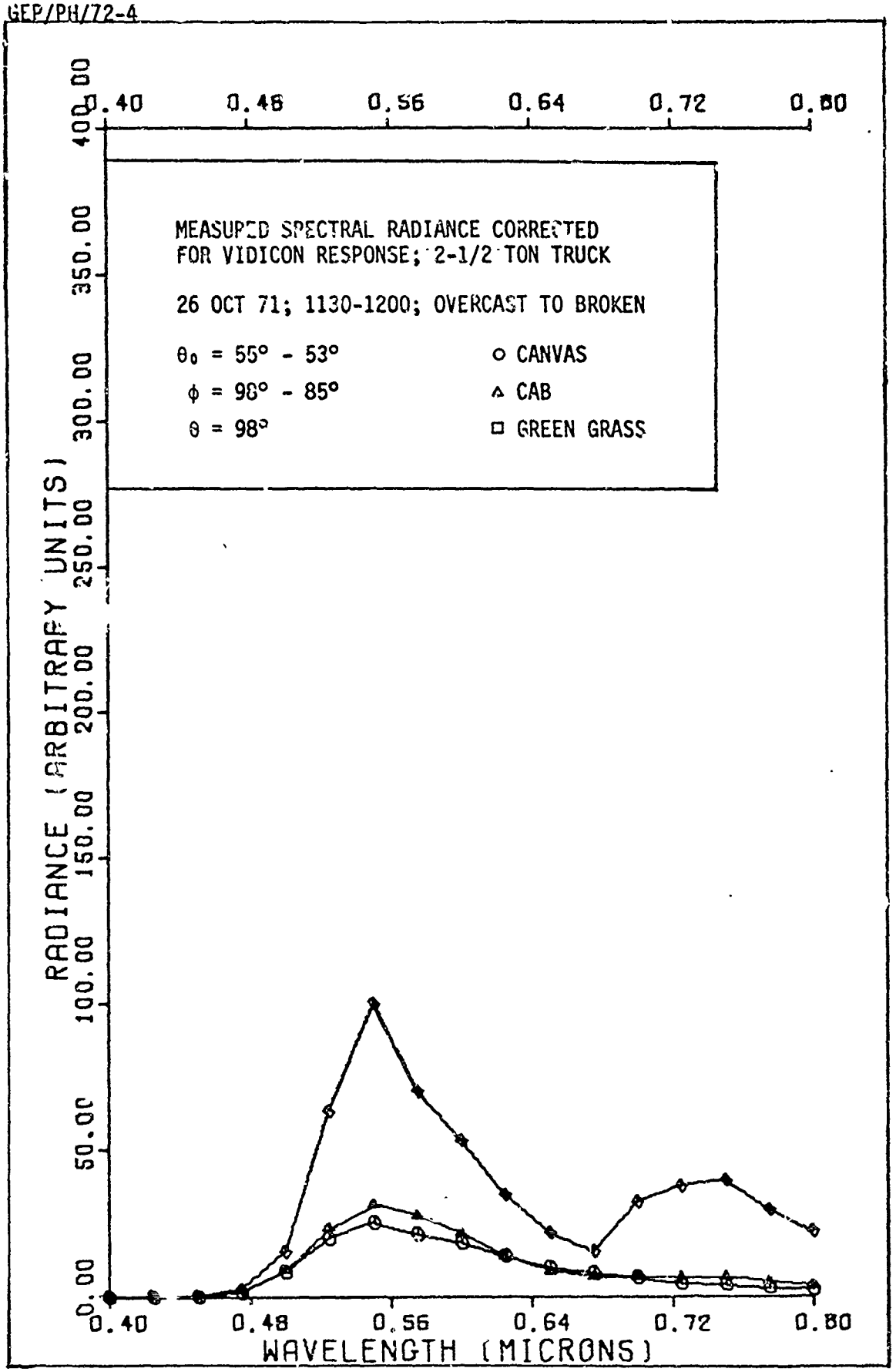

Fig. 61. Measured Spectral Radiance for Truck Against Grass Background. Data Corrected for Vidicon Response.

TABLE XIII

Inherent Contrast Available to the Eye and to a Vidicon

Date, Time (EDT)	Inherent Contrast			
	Photopic Response		Vidicon With Filter	
	.45-.75 μm	.4-.8 μm	.45-.75 μm	.4-.8 μm
26 Oct 71 1130-1200	-.66	-.66	-.68	-.70
26 Oct 71 1455-1530	-.66	-.66	-.69	-.71
27 Oct 71 1020-1050	-.89	-.89	-.90	-.91

for this target background situation. In this situation an advantage exists for this vidicon over the eye with regard to inherent contrast available.

The atmospheric contrast transmission is also more favorable for the longer visible wavelengths. The RRA Monte Carlo data for an isotropic source with albedo of .1, receiver at .5 KM, and a receiver zenith angle of 98° is given in Table XIV. This data would indicate a higher apparent contrast available at the sensor for the vidicon than for the eye, due to increased contrast transmission. Thus in any careful analysis in which predictions of sensor performance are to be made, the spectral considerations should be taken into account. Then the apparent contrast should be determined from

$$C_r(Z,\theta,\phi) = \int_{\lambda \text{ of sensor}} \tau_c(\lambda,Z,\theta,\phi) C_0(\lambda,Z_t,\theta,\phi) d\lambda \qquad (77)$$

TABLE XIV

Spectral Contrast Transmission From Monte Carlo Data

Wavelength	Contrast Transmission
.45 μm	.263
.55 μm	.306
.65 μm	.328
.75 μm	.308
.85 μm	.353

and the required apparent contrast of the system should be specified in terms of the response of the system.

Apparent Contrast Measurements

During the periods while measurements were made at Wright-Patterson AFB, a camera with a 1000 mm focal length, *f*/12 lens was positioned approximately 3000 feet from the truck. The camera was located along the same azimuth as the photometer and inherent contrast camera. It was on a small hill giving a look-down angle of .8°. The camera also used Kodak Plus-X film and a Wratten 102 filter. Photos of the truck-background scene were taken simultaneously with those taken at close-range and the film processed and analyzed in the same way to yield contrast. Thus the apparent contrast at this position was determined. The contrast transmission could then be calculated from the ratio. The results are shown in Table XV. From the estimated visibility and the measured contrast transmission the sky-ground ratio was calculated using Eq (43). These values are shown also in Table XV. In an attempt to determine whether the sky-ground ratio could be measured in the way indicated by Duntley, photometer measurements of the sky and

TABLE XV

Comparison of Computed and Measured Sky-Ground Ratios

Date, Time (EDT)	Solar Zenith	Azimuth From Sun	Receiver Zenith	Weather Visibility	C_0	C_r	τ_c	Sky-Ground Ratio Computed	Photometer	Photographic
21 Oct 71 1305-1355	50°	70°-50°	91°	Overcast 7-10	-.69(5)	-.57(15)	.83	.71-1.1	3.66(8)	4.29(26)
26 Oct 71 1020-1120	65°-57°	115°-100°	91°	Overcast to broken 2-4	-.66(7)	-.25(10)	.38	1.5-2.2	3.35(9)	3.54(25)
26 Oct 71 1400-1445	50°-55°	51°-31°	91°	Broken 4-5	-.62(15)	-.30(2)	.48	1.4-2.1	3.97(6)	5.85(32)
27 Oct 71 0912-1008	78°-67°	126°-113°	91°	Clear 3-4H	-.73(11)	-.39(11)	.53	1.2-1.7	1.93(8)	2.13(24)

Note: Visibilities are in miles
Numbers in parentheses are the number of samples averaged
H indicates haze obstructing visibility
Negative sign on contrast indicates target darker than background

the ground were taken in the appropriate direction. In this case as can be seen from Eqs (37) and (38), the situation reduces to the case where the sky should be measured in the same direction as the sensors are looking at the truck. The averaged sky-ground ratios by this technique are shown in Table XV with the number of samples averaged. Here as in all cases the "ground" value is the reflected radiance from the direction of the target along the inclined path to the sensor. Similar measurements were made from the inherent contrast photos of sky and ground in the direction of the target. The averaged values are shown in Table XV.

From this table it can be seen that the measured contrast transmissions and visibilities yield significantly lower values of sky-ground ratio except in the case where the sky is clear. Thus the results indicate that when there is an overcast or broken sky condition, the sky-ground ratio cannot be measured directly. With the clear sky condition, significant haze was present, causing the sky-ground ratio values to differ from what could be measured by the technique suggested by Duntley. Two values are shown for the values of sky-ground ratio computed from inherent and apparent contrast due to the uncertainty in the estimated visibility. The larger value is based on studies which show that the meteorologist typically estimates about 75% of the true meteorological range. True meteorological range is defined as that range where a large black object is just visible against the horizon sky. The apparent contrast threshold of the eye is assumed to be .02.

VII. Conclusions and Recommendations

As a result of the study several conclusions may be drawn:

1. The prediction of contrast transmission by using the sky-ground ratio and optical standard atmosphere must be modified to take into account the more realistic values of sky-ground ratio and atmospheric air-transmittance given in Chapter II.
2. The directional path reflectance R*, proposed more recently by Duntley, is a much better single parameter for use in evaluating the condition of the atmosphere for seeing. It is representative of the solar zenith, viewing angle, atmosphere and general scene albedo. R* may be used to evaluate the best azimuths and dive angles for any particular task. The value may be obtained from flight measurements or from model calculations in which assumptions are made.
3. Comparison of the RRA Monte Carlo model and the AWS model for the prediction of contrast transmission showed that the AWS model predicted higher contrast transmission for the 25 KM case by 15%. For the 3 KM case, the AWS data predicted lower contrast transmission for the low albedo case but mugh higher contrast transmission tor the high albedo case. This inconsistency is probably explained by the fact that the AWS model accounts for only first and second order scattering, while the atmospheric optical path becomes very long for low sun angles and low visibilities. The Monte Carlo data takes into account higher order scattering. The AWS model or other models of its type are optimized for fast running on the computer. They provide a valuable tool for

generating the needed data for making predictions of atmospheric effects on contrast transmission.

4. The inherent directional background reflectance was shown to be very important in the prediction of contrast transmission. A general tendency observed in measured data for the directional reflectance to increase at the lower dive angles tends to partially compensate for a decrease in air-transmittance. There is also generally an increase near the specular and anti-solar angles. Thus the contours of constant contrast transmission may be significantly modified when compared to those resulting from the assumption of a purely Lambertian surface.
5. Techniques were investigated for the measurement of contrast. The photographic technique was found to be comparable to the photometer technique. Simple densitometer techniques proved adequate for relatively uniform target and background scenes. This photo technique provides a very simple method of making inherent or apparent contrast measurements during flight tests.
6. Attempts to measure the sky-ground ratio by the technique suggested by Duntley in 1948 proved to be a failure when the skies were broken to overcast. The agreement was closer when the skies were clear although moderate haze was present. This confirmed Duntley's observation that the equilibrium radiance was equal to the radiance along the horizon only in the case of clear skies.

It is recommended that several actions be taken to improve predictive techniques and to validate the models through testing:

1. The AWS model and the RRA Monte Carlo model should be compared to

other of the existing mathematical models and to flight data to validate the models and determine their limitations. A data set has been requested from the University of Michigan. This will allow comparison under the same conditions as described in Chapter IV.

2. A desirable outcome of this research would be to generate a closed form analytic model which predicts contrast transmission based on the geophysical and weather parameters. The computer models, particularly the fast models, provide a good opportunity to generate large amounts of data under varying parameters for use in multiple regression analysis. Thus the effects and magnitudes of the effects of different parameters can be investigated and perhaps an analytic model evolved.
3. Models are only as good as the correct predictions they make. They must be checked against measured data. There is a clear lack of reliable meteorological and optical data during almost all flight tests of electro-optical systems. This is largely because the requirements of the atmospheric physicists and the system program engineers do not overlap. The atmospheric data is usually an afterthought, with test engineers accepting the standard meteorological information available. It is only through close planning at high levels that the two requirements can be overlapped. This requires that flight tests be planned far enough in advance that the atmospheric aspects may be considered and integrated into the program.
4. Many of the effects important to atmospheric contrast transmission can be studied without the particular electro-optical sensor being

present. For example, the decoupling of the target from the atmospheric contrast transmission implies that inherent contrasts may be measured for typical military targets against typical backgrounds without the particular aircraft and sensor flying around. This means that much more data can be achieved on inherent contrast under a wide variety of conditions, and at an enormously decreased price. Measurements like these would also provide inherent directional background reflectances which are important to contrast transmission. This requires that continued emphasis be given to applied research programs, so that the answers will be available for future systems in the concept stages and not later in the testing phase.

Bibliography

1. Koschneider, H. "Theorie der horizontalen Sichtweite." Beitr. Phys frein Atm. 12:33-53, and 171-181, 1924.

2. Duntley, S. Q. "The Reduction of Apparent Contrast by the Atmosphere." Journal of the Optical Society of America, 38:179-190 (February 1948).

3. Middleton, W. E. K. Vision Through the Atmosphere. Toronto: University of Toronto Press, 1952.

4. Bailey, H. H., and L. G. Mundie. The Effects of Atmospheric Scattering and Absorption on the Performance of Optical Sensors. The Rand Corporation, RM-5938-PR, March 1968.

5. McClatchey, R. A. et al. Optical Properties of the Atmosphere. Air Force Cambridge Research Laboratories, AFCRL-70-0527. Bedford, Mass., September 1970.

6. Malila, W. A., Crane, R. B., Omarzu, C. A., and R. E. Turner. Studies of Spectral Discrimination. Willow Run Laboratories, The University of Michigan, Ann Arbor, Mich., May 1971 (under contract to NASA).

7. Duntley, S. Q., Johnson, R. W., Gordon, J. I., and A. R. Boileau. Airborne Measurements of Optical Atmospheric Properties at Night. Scripps Institute of Oceanography, S10 Ref 70-7, University of California, (under contract for Air Force Cambridge Research Laboratories, AFCRL 70-0137). 1970.

8. Wells, M. B. Contrast Transmission Data for Clear and Hazy Model Atmospheres, Vols. I, II, and III. Radiation Research Associates, RRA-T92, Fort Worth, Texas, 1968 (under contract for Air Force Cambridge Research Laboratories, AFCRL-68-0660).

9. Private communication with Dr. Robert Fenn, Air Force Cambridge Research Laboratories, concerning Project Haven View. Work was conducted by the Visibility Laboratory, Scripps Institute of Oceanography under contract to AFCRL. Data will be published in the near future.

10. Valley, S. L., editor. Handbook of Geophysics and Space Environment. Bedford, Mass: Air Force Cambridge Research Laboratories, 1965.

11. Elterman, L. Vertical Attenuation Model With Eight Surface Meteorological Ranges. Air Force Cambridge Research Laboratories, AFCRL-70-0200, 1970.

12. Electro-Optics Handbook, RCA Defense Electronic Products, P. O. Box 538, Burlington, Mass., October 1968.

Bibliography

13. Elterman, L. An Atlas of Aerosol Attenuation and Extinction Profiles for the Troposphere. AFCRL-66-828, Bedford, Mass., 1966.

14. Regent, B. and F. K. Goodwin. A Program for the Evaluation of the Effects of Atmospheric Haze on Optical Contrast. Vidya Research and Development, Vidya Report No. 232, Palo Alto, Calif., September 1966.

15. Dakin, D. R., et al. Aerial Photographic Energy Model and User Manual for Aerial Photographic Energy Model. Philco-Ford Corporation, Newport Beach, Calif., June 1968 (under contract for Air Force Avionics Laboratory, AFAL-TR-68-136).

16. Breitling, Lt. Col. P. J. and Capt. S. Pilipowskyj. "Computer Simulation of Optical Contrast Reduction Caused by Atmospheric Aerosol." AIAA 8th Aerospace Sciences Meeting, AIAA Paper No. 70-194, New York, January 19-21, 1970

17. Collins, D. G. Atmospheric Path Radiance Calculations for a Model Atmosphere. Radiation Research Associates Report RRA-M82 (AFCRL-68-0124) March 1968.

18. Collins, D. G. and M. B. Wells. Flash, A Monte Carlo Procedure for Use in Calculating Light Scattering in a Spherical Shell Atmosphere. Radiation Research Associates, RRA-T704, Fort Worth, Texas, January 1970 (under contract to Air Force Cambridge Research Laboratories, AFCRL-70-0206).

19. Blattner, W. G., Collins, D. G. and M. B. Wells, Monte Carlo Calculations in Spherical Shell Atmospheres. Radiation Research Associates, RRA-T7104, Fort Worth, Texas, June 1971 (under contract to Air Force Cambridge Research Laboratories, AFCRL-71-0382).

20. Deirmendjian, D. Electronic Scattering on Spherical Polydispersions. New York: American Elsevier Publishing Company, 1969.

21. Neznanski, L. S., Morgan, F. E. and H. P. Koesters. Final Report of Flight Test Program for Optical Filters Study. Air Force Special Weapons Center, AFSWC-TR-70-25, Kirtland AFB, New Mexico, 1970.

22. Gordon, J. I. and P. V. Church. "Sky Luminances and the Directional Luminous Reflectances of Objects and Backgrounds for a Moderately High Sun," Applied Optics, 5:795-801 (May 1966).

23. Bolieau, A. R. and J. I. Gordon. "Atmospheric Properties and Reflectances of Ocean Water and Other Surfaces for Low Sun," Applied Optics, 5:803-813 (May 1966).

Bibliography

24. Gordon, J. I. and P. V. Church. "Overcast Sky Luminances and Directional Luminous Reflectances of Objects and Backgrounds under Overcast Skies," Applied Optics, 5:919-923 (June 1966).

25. Leeman, V, Earing D., Vincent, R. K., and S. Ladd. The NASA Earth Resources Spectral Information System: A Data Compilation, WRL 31650-24-T, Willow Run Laboratories, University of Michigan, Ann Arbor, Mich., 1971.

26. Duntley, S. Q., et al. "Visibility," Applied Optics, 3:549-602 (May 1964).

27. Mees, C. E. K. The Theory of the Photographic Process (Revised Edition). New York: The Macmillan Company, 1954.

28. Brown, E. B. Modern Optics. New York: Reinhold Publishing Co., 1965.

Appendix A

Definitions of Contrast

Three definitions for spectral contrast are examined here along with related expressions for spectral contrast transmission. All are based on the equation relating the spectral radiance at an altitude Z, along a slant path with receiver zenith angle θ and azimuth from the sun ϕ to the spectral radiance leaving the source in that direction.

$$N_r(Z,\theta,\phi) = N_0(Z_t,\theta,\phi)T(Z,\theta) + N^*(Z,\theta,\phi) \tag{A.1}$$

Universal Contrast

The definition of universal contrast was given in Chapter II, Eqs (8) and (9), and for universal contrast transmission in Eqs(13) and (58).

Using Eq (10),

$$C_r(Z,\theta,\phi) = C_0(Z,\theta,\phi)\tau_c(Z,\theta,\phi) \tag{A.2}$$

using Eqs (8) and (13)

$$C_r(Z,\theta,\phi) = \frac{{}_tN_0(Z_t,\theta,\phi) - {}_bN_0(Z_t,\theta,\phi)}{{}_bN_0(Z_t,\theta,\phi)} \times \frac{{}_bN_0(Z_t,\theta,\phi)}{{}_bN_0(Z_t,\theta,\phi) + N^*(Z,\theta,\phi)/T(Z,\theta)} \tag{A-3}$$

$$C_r(Z,\theta,\phi) = \frac{{}_tN_0(Z_t,\theta,\phi) - {}_bN_0(Z_t,\theta,\phi)}{{}_bN_0(Z_t,\theta,\phi) + N^*(Z,\theta,\phi)/T(Z,\theta)} \tag{A-4}$$

dividing each term in the numerator and denominator by $H(Z_t,d)/\pi$, the spectral irradiance on an upward facing horizontal surface at the target altitude, and recognizing that from Eq (58) these quantities are ${}_bR_0(Z_t,\theta,\phi)$,

${}_{t}R_0(Z_t,\theta,\phi)$ and $R^*(Z,\theta,\phi)$, the directional spectral reflectances of background, target, and path respectively, then

$$C_r(Z,\theta,\phi) = \frac{{}_{t}R_0(Z,\theta,\phi) - {}_{b}R_0(Z,\theta,\phi)}{{}_{b}R_0(Z,\theta,\phi) + R^*(Z,\theta,\phi)} \tag{A.5}$$

Thus a useful relation between apparent spectral contrast and R^*, ${}_{b}R_0$ and ${}_{t}R_0$ is obtained.

Contrast Modulation

Inherent spectral contrast modulation is defined as

$$C_{0_m} = \frac{{}_{t}N_0(Z,\theta,\phi) - {}_{b}N_0(Z,\theta,\phi)}{{}_{t}N_0(Z,\theta,\phi) + {}_{b}N_0(Z,\theta,\phi)} \tag{A.6}$$

Developing an expression for spectral contrast modulation at altitude Z, receiver zenith angle θ and azimuth ϕ, we get

$$C_{r_m}(Z,\theta,\phi) = \frac{{}_{t}N_0(Z,\theta,\phi)T(Z,\theta) - {}_{b}N_0(Z,\theta,\phi)T(Z,\theta)}{{}_{t}N_0(Z_t,\theta\ \phi)T(Z,\theta,\phi) + {}_{b}N_0(Z_t,\theta,\phi) + 2N^*(Z,\theta,\phi)} \tag{A.7}$$

dividing by $T(Z,\theta)$

$$C_{r_m}(Z, \qquad \frac{{}_{t}N_0(Z_t,\theta,\phi) - {}_{b}N_0(Z_t,\theta,\phi)}{{}_{t}N_0(Z_t,\theta,\phi) + {}_{b}N_0(Z_t,\theta,\phi) + 2N^*(Z,\theta,\phi)/T(Z,\theta)} \tag{A.8}$$

then

$$\tau_{C_m}(Z,\theta,\phi) = \frac{1}{\dfrac{{}_{t}N_0(Z_t,\theta,\phi) + {}_{b}N_0(Z_t,\theta,\phi) + 2N^*(Z,\theta,\phi)/T(Z,\theta)}{{}_{t}N_0(Z_t,\theta,\phi) + {}_{b}N_0(Z_t,\theta,\phi)}} \tag{A.9}$$

dividing each term in the denominator by $H(Z,d)/\pi$ we get

$$\tau_{c_m}(Z,\theta,\phi) = \frac{1}{1 + \dfrac{R^*(Z,\theta,\phi)}{[{}_tR_0(Z_t,\theta,\phi) + {}_bR_0(Z_t,\theta,\phi)]/2}} \tag{A.10}$$

then

$$\boxed{\tau_{c_m}(Z,\theta,\phi) = \frac{1}{1 + R^*(Z,\theta,\phi)/\bar{R}_0(Z_t,\theta,\phi)}} \tag{A.11}$$

where $\bar{R}_0(Z_t,\theta,\phi)$ is the average spectral directional reflectance of the target and background.

Then

$$C_{r_m}(Z,\theta,\phi) = \tau_{c_m}(Z,\theta,\phi)C_{0_m}(Z_t,\theta,\phi) \tag{A.12}$$

$$\boxed{C_{r_m} = \frac{{}_tR_0(Z_t,\theta,\phi) - {}_bR_0(Z_t,\theta,\phi)}{1 + R^*(Z,\theta,\phi)/\bar{R}_0(Z_t,\theta,\phi)}} \tag{A.13}$$

Contrast Ratio

Spectral contrast ratio is defined as the ratio of target spectral radiance to background spectral radiance.

Then

$$C_{0_{c_R}}(Z_t,\theta,\phi) = \frac{{}_tN_0(Z_t,\theta,\phi)}{{}_bN_0(Z_t,\theta,\phi)} \tag{A.14}$$

and

$$C_{r_{c_R}}(Z,\theta,\phi) = \frac{{}_tN_0(Z_t,\theta,\phi)T(Z,\theta) + N^*(Z,\theta,\phi)}{{}_bN_0(Z_t,\theta,\phi)T(Z,\theta) + N^*(Z,\theta,\phi)} \tag{A.15}$$

dividing by $T(Z,\theta)$ and then by $H(Z,d)/\pi$,

$$C_{r_{c_R}}(Z_t,\theta,\phi) = \frac{{}_tR_0(Z_t,\theta,\phi) + R^*(Z,\theta,\phi)}{{}_bR_0(Z_t,\theta,\phi) + R^*(Z,\theta,\phi)} \tag{A.16}$$

and

$$\tau_{c_{c_R}}(Z,\theta,\phi) = \frac{1 + R^*(Z,\theta,\phi)/{}_tR_0(Z,\theta,\phi)}{1 + R^*(Z,\theta,\phi)/{}_bR_0(Z,\theta,\phi)} \tag{A.17}$$

We note that useful relations have been developed between three definitions of contrast and the directional path reflectance $R^*(Z,\theta,\phi)$, and the inherent spectral directional reflectances of target and background. From the flight measurement point of view, the universal contrast definition is the most useful, since we see that only in this definition is the spectral contrast transmission independent of the target.

Appendix B

Computation of Scattering Angle

To compute angle $\underline{\beta}$ between two lines in space,

$$\cos \underline{\beta} = \cos \alpha_1 \cos \alpha_2 + \cos \beta_1 \cos \beta_2 + \cos \gamma_1 \cos \gamma_2 \qquad (B.1)$$

where

$$\cos \alpha_1 = \frac{x_1}{d} = \frac{d \sin \theta_0 \cos \phi_0}{d}$$

$$\cos \alpha_1 = \sin \theta_0 \cos \phi_0$$

$$\cos \beta_1 = \frac{y_2}{d} = \frac{d \sin \theta_0 \sin \phi_0}{d}$$

$$\cos \beta_1 = \sin \theta_0 \sin \phi_0$$

$$\cos \gamma_1 = \frac{z_1}{d} = \frac{d \cos \theta_0}{d} = \cos \theta_0$$

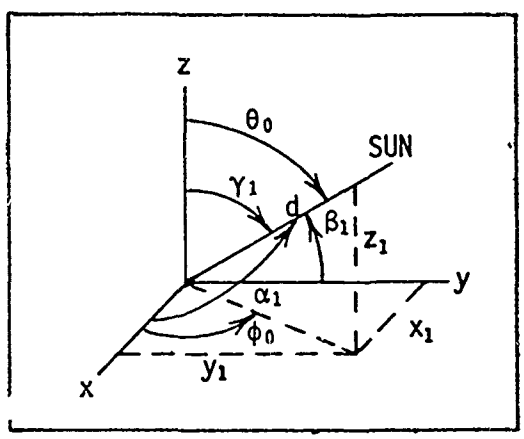

then

$$\cos \alpha_1 = \sin \theta_0 \cos \phi_0 \qquad (B.2)$$

$$\cos \beta_1 = \sin \theta_0 \sin \phi_0 \qquad (B.3)$$

$$\cos \gamma_1 = \cos \theta_0 \qquad (B.4)$$

For an observer at receiver zenith angle θ and azimuth $\underline{\phi}$,

$$\gamma_2 = 180 - \theta$$

$$\cos \alpha_2 = \frac{x_2}{d_2} = \frac{d_2 \sin(180 - \theta) \cos \underline{\phi}}{d_2}$$

$$\cos \alpha_2 = \sin(180 - \theta) \cos \underline{\phi}$$

$$\cos \beta_2 = \frac{y_2}{d_2} = \frac{d_2 \sin(180 - \theta) \sin \underline{\phi}}{d_2}$$

$$\cos \beta_2 = \sin(180 - \theta) \sin \underline{\phi}$$

$$\cos \gamma_2 = \frac{z_2}{d} = \frac{d_2 \cos(180 - \theta)}{d}$$

$$\cos \gamma_2 = \cos(180 - \theta)$$

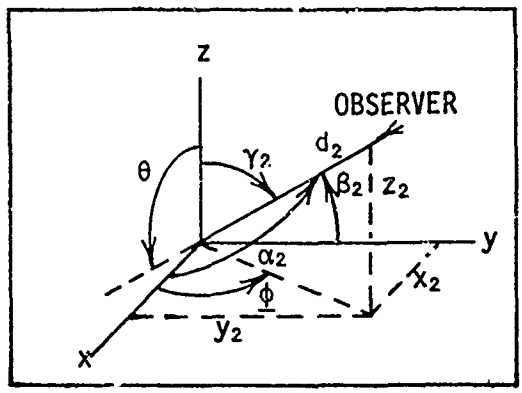

then

$$\cos \alpha_2 = \sin(180 - \theta) \cos \underline{\phi} \tag{B.5}$$

$$\cos \beta_2 = \sin(180 - \theta) \sin \underline{\phi} \tag{B.6}$$

$$\cos \gamma_2 = \cos(180 - \theta) \tag{B.7}$$

then

$$\cos \underline{\beta} = \sin \theta_0 \cos \phi_0 \sin(180 - \theta) \cos \underline{\phi} + \sin \theta_0 \sin \phi_0 \sin(180 - \theta) \sin \underline{\phi} + \cos \theta_0 \cos(180 - \theta) \tag{B.8}$$

but

$$\sin(180 - \alpha) = \sin \alpha$$

$$\cos(180 - \alpha) = - \cos \alpha$$

so

$$\cos \underline{\beta} = \sin \theta_0 \cos \phi_0 \sin \theta \cos \phi + \sin \theta_0 \sin \phi_0 \sin \theta \sin \phi - \cos \theta_0 \cos \theta \tag{B.9}$$

If the sun is in the yz plane, $\alpha_1 = 90°$; $\beta_1 = 90 - \gamma_1 = 90 - \theta_0$; $\phi_0 = 90°$, so

$$\cos \underline{\beta} = \sin \theta_0 \sin \theta \sin \underline{\phi} - \cos \theta_0 \cos \theta \tag{B.10}$$

in terms of angles from the sun in the yz plane

$$\underline{\phi} = \phi - 90^\circ = -(90 - \phi)$$

then

$$\boxed{\cos \beta = -\sin \theta_0 \sin \theta \cos \phi - \cos \theta_0 \cos \theta} \qquad \text{(B.11)}$$

The scattering angle β is $180^\circ - \underline{\beta}$, so

$$\cos \beta = -\cos \underline{\beta} = +\sin \theta_0 \sin \theta \cos \phi + \cos \theta_0 \cos \theta$$

$$\boxed{\cos \beta = \cos \theta_0 \cos \theta + \sin \theta_0 \sin \theta \cos \phi} \qquad \text{(B.12)}$$

Appendix C

Calculated Sky-Ground Ratios From RRA Monte Carlo Data

This appendix presents sky-ground ratios calculated from the RRA Monte Carlo data. The sky-ground ratio is calculated from Eq (43) by solving for K in terms of τ_c and the air-transmittance $T = \exp(-\sigma_0 \bar{R})$. Both the contrast transmission and the air-transmittance are known from Ref 8. Due to the variations of K with altitude, all values for a particular receiver zenith angle have been averaged over the altitudes for which data was computed (.5 KM to 10 KM). For a solar zenith angle of 0°, only the azimuth averaged values of K are presented, since for this solar zenith, any variation with azimuth is meaningless and due to the statistical variation of the Monte Carlo method.

Values of sky-ground ratio for slant paths in excess of 12 KM for the 3 KM surface visibility case and 50 KM for the 25 KM surface visibility case have been excluded from the altitude averaging. This is done because an increase in error in the calculation of air-transmittance for long slant paths causes a sharp increase in the computed K value. The exclusion is justified by the rather academic usefulness of values at slant ranges greater than 12 or 50 KM for the particular visibilities quoted.

TABLE C-I

Computed Sky-Ground Ratios from RRA Monte Carlo Data for 3 KM Visibility

All entries have been averaged over altitude. Values for slant ranges greater than 12 KM have been ignored.

	Receiver Zenith Angle θ	Albedo			
		.1	.3	.6	.9
Wavelength λ = .55 μm Overcast	171	3.4	1.9	1.5	1.4
	164	3.6	2.0	1.6	1.4
	157	3.5	2.0	1.6	1.4
	148	3.9	2.1	1.6	1.5
	138	4.5	2.3	1.7	1.5
	130	5.1	2.5	1.8	1.6
	123	6.6	2.9	2.0	1.7
	116	6.3	3.0	2.1	1.7
	110	11.	4.0	2.5	2.0
	104	11.	4.4	2.7	2.1
	98	3.4	1.5	.96	.79
	93	3.2	1.3	.77	.61
Wavelength λ = .65 μm Overcast	171	3.9	2.3	1.9	1.8
	164	4.75	2.6	2.1	1.9
	157	4.5	2.5	2.0	1.8
	148	5.1	2.7	2.1	1.9
	138	4.8	3.1	2.3	2.1
	130	7.0	3.5	2.5	2.2
	123	9.0	4.1	3.0	2.5
	116	11.	5.0	3.0	2.9
	110	13.0	6.3	4.1	3.3
	104	20.	8.0	5.0	3.7
	98	5.7	2.4	1.6	1.3
	93	11.4	4.4	2.7	2.1

TABLE C-II

Computed Sky-Ground Ratios from RRA Monte Carlo
Data for 25 KM Visibility

All entries have been averaged over altitude. Values for slant ranges greater than 50 KM have been ignored.

	Receiver Zenith Angle θ	Albedo			
		.1	.3	.6	.9
Wavelength λ = .55 μm Overcast	171	2.6	1.4	1.1	1.0
	164	2.5	1.3	1.0	.90
	157	2.7	1.4	1.0	.92
	148	1.8	1.3	1.0	.90
	138	2.9	1.4	1.0	.85
	130	3.5	1.6	1.2	1.0
	123	3.8	1.7	1.2	1.0
	116	3.9	1.7	1.1	.96
	110	4.3	1.8	1.2	.94
	104	4.9	1.9	1.2	.96
	98	5.1	1.9	1.1	.77
	93	5.1	2.0	1.3	1.0
Wavelength λ = .65 μm Overcast	171	2.3	1.2	.93	.83
	164	2.4	1.3	1.0	.93
	157	2.0	1.0	.76	.70
	148	2.7	1.4	1.0	.91
	138	3.0	1.4	1.0	.92
	130	3.3	1.6	1.2	1.1
	123	3.6	1.7	1.2	1.0
	116	4.0	1.7	1.1	.95
	110	4.3	1.8	1.1	.92
	104	5.7	2.3	1.4	1.1
	98	6.1	2.4	1.3	.97
	93	7.4	2.9	1.8	1.4

TABLE C-III

Computed Sky-Ground Ratios from RRA Monte Carlo Data for 3 KM Visibility

All entries have been averaged over altitude. Values for slant ranges greater than 12 KM have been ignored.

Wavelength λ = .55 μm; Solar Zenith Angle θ_0 = 0°

	Receiver Zenith Angle θ	Azimuth Averaged
Albedo = .1	171	2.6
	164	2.7
	157	3.0
	148	2.7
	138	2.8
	130	2.5
	123	2.3
	116	2.9
	110	3.9
	104	3.9
	98	1.9
	93	1.6
Albedo = .9	171	1.3
	164	1.4
	157	1.4
	148	1.3
	138	1.4
	130	1.4
	123	1.5
	116	1.3
	110	1.5
	104	1.4
	98	.6
	93	.4

TABLE C-IV

Computed Sky-Ground Ratios from RRA Monte Carlo Data for 25 KM Visibility

All entries have been averaged over altitude. Values for slant ranges greater than 50 KM have been ignored.

Wavelength λ = .55 μm; Solar Zenith Angle θ_0 = 0°

	Receiver Zenith Angle θ	Azimuth Averaged
Albedo = .1	171	2.6
	164	2.3
	157	1.6
	148	2.2
	138	2.1
	130	1.8
	123	1.6
	116	1.5
	110	1.7
	104	1.3
	98	1.4
	93	1.8
Albedo = .9	171	.94
	164	.86
	157	.56
	148	.88
	138	.75
	130	.98
	123	.70
	116	.67
	110	.76
	104	.50
	98	.62
	93	.81

TABLE C-V

Computed Sky-Ground Ratios from RRA Monte Carlo Data for 3 KM Visibility

All entries have been averaged over altitude. Values for slant ranges greater than 12 KM have been ignored.

Wavelength λ = .55 μm; Solar Zenith Angle θ_0 = 30°

	Receiver Zenith Angle θ	Azimuth				
		22.5°	67.5°	112.5°	157.5°	Average
Albedo = .1	171	2.5	2.2	3.7	2.5	2.7
	164	2.5	2.8	2.6	2.8	2.7
	157	2.8	3.0	2.7	3.2	3.0
	148	3.0	2.6	2.6	3.1	2.8
	138	2.6	2.5	3.0	2.9	2.8
	130	3.7	2.8	3.5	3.8	3.4
	123	4.1	3.4	3.6	3.7	3.8
	116	4.5	3.9	3.1	3.3	3.7
	110	4.9	4.1	4.0	4.1	4.3
	104	4.8	4.7	3.6	4.5	4.4
	98	2.9	1.6	1.1	1.6	1.8
	93	2.4	2.1	1.1	1.1	1.7
Albedo = .9	171	1.4	1.3	1.5	1.2	1.4
	164	1.3	1.4	1.2	1.3	1.3
	157	1.3	1.4	1.3	1.4	1.4
	148	1.4	1.4	1.3	1.3	1.4
	138	1.3	1.2	1.4	1.4	1.3
	130	1.5	1.4	1.5	1.4	1.5
	123	1.6	1.4	1.5	1.6	1.6
	116	1.5	1.6	1.3	1.4	1.4
	110	1.4	1.5	1.6	1.4	1.5
	104	1.1	1.7	1.5	1.5	1.5
	98	.70	.64	.55	.74	.66
	93	.48	.31	.28	.27	.33

TABLE C-VI

Computed Sky-Ground Ratios from RRA Monte Carlo Data for 25 KM Visibility

All entries have been averaged over altitude. Values for slant ranges greater than 50 KM have been ignored.

Wavelength λ = .55 μm; Solar Zenith Angle θ_0 = 30°

	Receiver Zenith Angle θ	Azimuth				
		22.5°	67.5°	112.5°	157.5°	Average
Albedo = .1	171	2.6	2.1	3.5	1.6	2.4
	164	1.8	2.4	1.8	1.1	1.7
	157	1.8	1.2	1.4	1.8	1.6
	148	1.7	1.4	1.9	2.0	1.8
	138	1.5	1.9	1.7	1.7	1.7
	130	2.0	1.7	1.7	1.8	1.8
	123	2.2	1.6	2.1	2.4	2.0
	116	1.6	1.7	1.6	1.9	1.7
	110	1.9	1.8	2.2	1.9	2.0
	104	1.4	1.6	1.5	1.9	1.6
	98	1.7	2.1	2.3	1.3	1.9
	93	3.4	1.9	1.6	1.4	1.7
Albedo = .9	171	1.0	.6	1.56	.97	1.0
	164	1.7	1.6	.63	.41	1.0
	157	.98	.93	.69	.65	.81
	148	.78	.66	.80	.79	.75
	138	.80	.92	.61	.65	.75
	130	1.0	.78	.68	.54	.75
	123	1.26	.85	.88	.88	.97
	116	.77	.88	.58	.72	.73
	110	.82	.59	.77	.76	.74
	104	.71	.60	.61	.53	.61
	98	.55	.63	.54	.51	.56
	93	.88	.77	.63	.84	.78

TABLE C-VII

Computed Sky-Ground Ratios from RRA Monte Carlo Data for 3 KM Visibility

All entries have been averaged over altitude. Values for slant ranges greater than 12 KM have been ignored.

Wavelength λ = .55 μm; Solar Zenith Angle θ_0 = 75°

	Receiver Zenith Angle θ	Azimuth				
		22.5°	67.5°	112.5°	157.5°	Average
Albedo = .1	171	5.2	4.9	4.9	5.9	5.2
	164	6.4	4.8	5.7	4.8	5.4
	157	4.3	5.4	5.3	4.6	4.9
	148	6.7	5.8	4.7	5.9	5.8
	138	9.1	6.9	5.9	7.6	7.4
	130	12.7	8.4	5.4	6.5	19.0
	123	10.7	7.8	8.9	12.0	25.0
	116	10.0	9.8	9.9	13.0	44.0
	110	16.0	10.6	13.5	21.0	51.0
	104	16.4	12.9	17.0	23.0	10.0
	98	4.63	2.4	4.14	5.8	13.0
	93	13.0	4.2	2.9	3.3	5.9
Albedo = .9	171	1.4	1.3	1.4	1.9	1.5
	164	1.5	1.6	1.6	1.4	1.5
	157	1.5	1.6	1.5	1.3	1.5
	148	1.7	1.5	1.4	1.5	1.5
	138	2.1	1.7	1.5	1.8	1.8
	130	2.2	1.8	1.6	1.7	1.8
	123	3.1	2.2	1.9	1.9	2.2
	116	3.2	2.0	2.1	2.2	2.2
	110	4.9	2.3	2.0	2.2	2.9
	104	5.3	2.7	2.2	2.2	2.2
	98	1.3	1.0	.75	.89	1.0
	93	1.5	.88	.5	1.2	1.0

TABLE C-VIII

Computed Sky-Ground Ratios from RRA Monte Carlo Data for 25 KM Visibility

All entries have been averaged over altitude. Values for slant ranges greater than 50 KM have been ignored.

Wavelength λ = .55 μm; Solar Zenith Angle θ_0 = 70°

	Receiver Zenith Angle θ	Azimuth				
		22.5°	67.5°	112.5°	157.5°	Average
Albedo = .1	171	2.3	4.8	3.7	1.8	3.1
	164	2.5	2.2	4.4	2.8	2.8
	157	2.9	4.0	3.3	4.3	3.6
	148	3.2	2.9	3.9	3.6	3.4
	138	3.3	3.8	2.8	3.8	3.4
	130	5.8	3.6	3.9	4.1	4.4
	123	6.0	3.9	4.1	3.8	4.5
	116	8.8	5.3	3.8	5.4	5.8
	110	9.8	4.2	4.4	5.6	6.0
	104	11.5	5.5	3.4	5.4	6.5
	98	17.0	4.6	3.3	4.8	7.4
	93	15.0	5.3	7.4	3.6	7.9
Albedo = .9	171	.37	1.51	1.52	.74	1.0
	164	.16	1.2	1.1	.98	.70
	157	.50	1.4	1.2	1.2	
	148	.90	.73	1.4	.93	
	138	.89	1.1	.77	.86	.90
	130	1.5	.89	1.1	.99	1.1
	123	1.2	.78	1.1	.83	.98
	116	1.25	1.04	.88	1.1	1.1
	110	1.4	.92	1.2	1.0	1.1
	104	1.7	.92	.82	1.0	1.1
	98	2.0	.86	.74	.81	1.1
	93	2.0	.89	1.2	.81	1.2

Vita

Edward Aloysius Duff was born 29 July 1942 in Philadelphia, Pennsylvania. He attended high school at Saint Joseph's College High School, where he graduated in 1960. He was appointed to the United States Air Force Academy where he graduated and was commissioned in 1965. He received a Bachelor of Science in Engineering Science. He was assigned to the Deputy for Flight Test, Wright-Patterson Air Force Base, Ohio, as an Electronics Engineer. Here he planned, directed and reported on the flight tests of advanced avionics and infrared systems for aircraft. He entered the Air Force Institute of Technology in June 1970, where he was elected to Tau Beta Pi.

Permanent address: 5729 Kingsessing Ave.
Phila., Penna., 19143

This thesis was typed by Mrs. Virginia Blakelock